Faculty of Mathematics and Natural Sciences
University of Oslo

A

THESIS

for the degree of

MASTER OF SCIENCE

in

THEORETICAL PHYSICS

ON THE PROSPECTS FOR MICROLENSING WIMPY HALOS

by

AUGUST GEELMUYDEN

MAY, 2018

Abstract

The kinetic decoupling of thermal dark matter candidates sets a model dependent mass scale below which structure formation is heavily suppressed. Probing the population of dark sub-halos therefore provides invaluable information about the particle nature of dark matter. Due to their elusive nature, however, the abundance of small-scale dark halos remains unknown to this day. We investigate the prospects for their detection using gravitational microlensing, a technique utilizing the temporary, apparent increase in the brightness of a distant star arising from the passage of a massive intermediate object. It is found that while one can put strong bounds on highly concentrated NFW-profiled halos, there is a minimal concentration needed for NFW-halos to produce observable microlensing effects. This minimal concentration is related to an exponential shrinkage of the Einstein ring in lensing geometries only sensitive to the inner $1/\mathtt{r}$ profile of the halo. We conclude that WIMPy halos nearby are likely never to be constrained by microlensing. At cosmological scales, microlensing of WIMPy halos could produce observable effects. Strong constraints from cosmological microlensing of WIMPy halos is doubted, but remains a possibility and should be investigated further.

Acknowledgements

First of all, I would like to extend my sincere gratitude for the guidance, encouragement and support provided by both my supervisors, Torsten Bringmann and Andrzej Hryczuk – your insight in the field is truly inspirational! I have learned a lot from our long discussions and your constructive feedback during the last year. A special thanks goes to Torsten for suggesting this topic, which has been an excellent match for me.

I also want to express my thankfulness to you Eline, for your constant support, for believing in me, and for enduring my absent-mindedness.

I would like to thank all the people who have played a part in making the last five years at Blindern fantastic. A special mention goes to all the students at "Lillefy" for our long conversations in the lunch room.

Thanks also to the theory group for providing a social and professional environment and for sticking together in trying to save a spot for theoretical physics after the reconstruction.

Last, but not least, I want to express my gratitude to Lånekassen, and therefore, every single Norwegian tax payer, who have financed me the last five years. This would not have been possible without you.

Motivation

The present abundance of small-scale dark matter halos is dependent on the particle properties. Detecting such halos can shed light on the expected cut-off in the halo mass function, and therefore, constrain particle dark matter candidates in a way that is complementary to other searches. The population of small-scale dark matter halos, being both transparent and diffuse, remains one of the open questions in the dark matter campaign.

Gravitational microlensing, which utilizes the temporarily increased brightness of a star due to the passage of an intervening massive object, has, during the last 30 years, provided stringent bounds on the multitude of compact astrophysical objects. Recently, there have been claims that also Axion miniclusters, modeled as highly concentrated NFW-profiled objects, can be constrained by gravitational microlensing [1]. This raises the question: can the less concentrated, small-scale dark matter halos predicted by cold, thermal relics also be constrained by existing microlensing data? If not, then what would it take to construct such a survey? We will attempt to answer these questions in a general way. That is, we will determine the requirements on NFW profile parameters needed to produce observable microlensing effects.

A Readers Manual

Before embarking on the actual thesis, let us prepare ourselves for what is to come. The text consist of four main parts. In the first, we introduce the dark matter problem from a historical point of view and provide a minimal introduction to Cosmology and structure formation. In the latter, we will briefly explain the crucial role dark matter has in explaining the formation of structures in the Universe, use some simple models to motivate the WIMP-candidate, and see how the particle properties of thermal relics are expected to affect the abundance of halos. The first part aims to provide the minimal background needed to see why knowing the population of small-scale dark matter halos could provide unique insight into the nature of dark matter. The reader is asked to condone the shortcomings resulting from the attempt at completeness and brevity.

In the second part, we first introduce the physics of gravitational lensing from first principles. We will then look at the history of gravitational lensing, and discuss the unlikeliness of microlensing events. Towards the end of the second part, we will introduce the formalism for constraining the amount of point-like objects with microlensing. We then discuss aspects of a numerical computation, while benchmarking with existing limits on the population of Primordial Black Holes. After the second part, we will have seen how the absence of microlensing events can be turned into constraints on the abundance of objects, and how these constraints depend on the lens-properties of the object.

In the third part, we study the microlensing of extended, NFW-profiled halo objects. Here, we will find analytic expressions for the lens properties and discuss complications with the numerical implementation when considering microlensing by extended objects. At the end, we present the number of expected microlensing events for an idealized survey of the Andromeda galaxy for a large portion of the NFW parameter space. This is followed by a discussion of the main features of these results, paying special attention to why WIMPy halos are expected to produce no microlensing events.

In the fourth, and last part, we discuss additional complications that may arise, and ask ourselves what the requirements are for the microlensing of WIMPy halos to produce observable effects. Finally, we recite some alternative techniques for constraining the abundance of halos.

As for conventions, we choose the signature of the metric to be so that the spacetime interval is positive for space-like events. We will mostly work in natural units, where $\mathtt{c} = \hbar = \mathtt{k}_\mathrm{B} = 1$. Sometimes, however, these fundamental constants will be written explicitly to simplify conversion into historical units.

Contents

Page

1 What is the Matter? 2
- 1.1 Historical Prelude . . . 2
- 1.2 The Formation of Structures . . . 4
  - 1.2.1 General Relativity and The Beginning of Time . . . 4
  - 1.2.2 The Need for a Decoupled Species . . . 8
  - 1.2.3 The Collapse of Overdensities . . . 11
  - 1.2.4 The Smallest Clumps . . . 13
  - 1.2.5 The Miraculous WIMP and its Contenders . . . 15
  - 1.2.6 The Structure and Abundance of Halos . . . 17

2 Gravity as Deflector of Light 20
- 2.1 Gravitational Lensing . . . 20
  - 2.1.1 Light Propagating in a Gravitational Potential . . . 20
  - 2.1.2 The Lens Equation . . . 21
  - 2.1.3 Apparent Magnification of the Source . . . 23
- 2.2 Gravitational Microlensing . . . 26
  - 2.2.1 Types of Gravitational Lensing . . . 26
  - 2.2.2 The History and Status of Gravitational Lensing . . . 27
  - 2.2.3 The Unlikeliness of a Microlensing Event . . . 29
  - 2.2.4 The Number of Expected Microlensing Events . . . 32
- 2.3 Constraints on Point-like Objects . . . 34
  - 2.3.1 Bound Objects between us and M31 . . . 34

3 Microlensing of Halo Objects 43
- 3.1 Lensing by NFW-profiled Objects . . . 43
  - 3.1.1 The Profile and its Projected Mass . . . 43
  - 3.1.2 Estimating the Tube Radius . . . 46
- 3.2 Can WIMPy Halos be Microlensed? . . . 49
  - 3.2.1 Which Halos are Observable? . . . 49
  - 3.2.2 The Reasonable Behavior of the Prospect Plane . . . 50
  - 3.2.3 Disappearance of the Einstein Ring . . . 52

4 Remedies and the Future **57**
4.1 Unspoken Complications 57
4.2 Increased Distance and the Sparsity of Photons 59
4.3 The Future of Halo Constraints from Lensing 62

5 Conclusion **64**

Appendix A The Deflection Angle **66**

Chapter 1

What is the Matter?

During the last century, astrophysical measurements of the total mass of astronomical bodies have consistently been larger than the combined mass of the objects believed to constitute the bodies. This problem can be handled in two ways, one can either attempt to construct a modified theory of gravity or one can postulate the presence of new forms of matter – referred to as *Dark Matter*. This chapter aims to briefly argue for the presence of dark matter, recite the main constraints and mention some compelling candidates.

1.1 Historical Prelude

Already in 1904, Lord Kelvin attempted to estimate the amount of non-luminous matter in our Galaxy [2]. His conclusion that perhaps a great majority of the stars may be dark bodies was, however, opposed already two years later by Henri Poincaré who is considered the first to use the term *Dark Matter* (or *Matière Obscure*) [3]. In 1915 Ernst Öpik concluded that dark matter is not needed to explain the dynamics of the nearby stars. A statement that would be confirmed by Jacobus C. Kapteyn seven years later [4]. In 1932 Jan Oort estimated the total dynamical mass near the sun to be $0.092\mathrm{M}_\odot/\mathrm{pc}^3$ and compared it to the density due to stars, which he took to be about $0.038\mathrm{M}_\odot/\mathrm{pc}^3$ [5]. When taking faint stars into consideration he concluded that the density of non-luminous matter must be less, and probably much less, than $0.05\mathrm{M}_\odot/\mathrm{pc}^3$. He was right, according to present knowledge the density of dark matter is indeed much less. A recent (2012) estimate of the local dark matter density states $0.008\mathrm{M}_\odot/\mathrm{pc}^3 \pm 37\%$ [6] which is about $5.37 \times 10^{-25}\mathrm{g/cm}^3$. For comparison, this would correspond roughly to a density of only one Hydrogen atom every third cubic centimeter. Whatever this matter is, it surely does not seem like a big problem. In fact, Oort explicitly refers to it as nebulous and meteoric matter. As we shall see shortly, this is no longer a likely option.

Dark matter as a serious problem would first appear from estimates of the gravitating mass of whole galaxies and systems of galaxies. In 1933, Fritz Zwicky used measurements of redshifts in the Coma cluster, published by Edvin Hubble and

Milton Humason two years earlier [7], to conclude that the amount of dark matter in the Coma system vastly outnumbers the luminous matter [8, 9]. His idea was simple: Using that the Coma cluster has radius $R \simeq 10^6 \mathrm{ly}$ and contains 800 galaxies, each having a mass of about $M = 10^9 M_\odot$, he estimated the average gravitational potential using

$$\langle V \rangle = -\frac{3}{5} G \frac{M^2}{R} \tag{1.1}$$

and found $\langle V \rangle / M \simeq -64 \times 10^{12} \mathrm{cm}^2 \mathrm{s}^{-2}$. Assuming the cluster to be virialized he could then relate kinetic K and potential energy V through $2\langle K \rangle = -\langle V \rangle$. When writing the average kinetic energy in terms of the velocity dispersion $\langle v^2 \rangle^{\frac{1}{2}}$ he then found

$$\langle v^2 \rangle^{\frac{1}{2}} \simeq \sqrt{2\frac{\langle K \rangle}{M}} \simeq \sqrt{\frac{3}{5}\frac{GM}{R}} \simeq 80 \mathrm{km/s}. \tag{1.2}$$

This being one order of magnitude less than the measured value of about $1000 \mathrm{km/s}$, Zwicky concluded that " *...the average density in the Coma system would have to be at least 400 times larger than that derived on the grounds of observations of luminous matter".*

Today we know that Zwicky's estimate exaggerates the amount of dark matter by about one order of magnitude due to the usage of a Hubble constant about 8.3 times larger than the present value $(67.74 \pm 0.46) \mathrm{km/s/Mpc}$ [10]. Nevertheless, the evidence still points towards the existence of a non-luminous, dominating matter component in the Coma cluster.

At the time, Zwicky's findings were considered peripheral and uninteresting [4], which might be the reason that it was first in 1959 that the next breakthrough was made, now by F. D. Kahn and L. Woltjer [11]. They argued that since the Andromeda galaxy (M31), contrary to most other galaxies, appears blue-shifted, it must be moving towards us. Being the closest galaxy, this makes sense if the Milky Way (MW) and M31 form a gravitationally bound system. When calculating the total mass of this system, Kahn and Woltjer found a total mass about six times larger than the reduced mass of the two galaxies combined. This points to an enormous amount of non-luminous matter which the authors suggested to be hot, intergalactic gas with a temperature of about $5 \times 10^5 \mathrm{K}$.

The evidence that came to tilt the community, however, appeared through the study of galactic rotation curves. Rotation curves had been studied earlier, but advances in technology during the 60s allowed measurements of the rotational velocity at increasingly large radii [12]. The problem was that according to Newtonian gravity the rotational velocity v, assuming for simplicity a spherically symmetric mass distribution and purely radial velocities, must be related to the contained mass $M(r)$ within a radius r by

$$v = \sqrt{\frac{GM(r)}{r}}\,. \tag{1.3}$$

This means that one would expect the rotational velocity to experience a so-called *Keplerian velocity decrease* $v \propto 1/\sqrt{r}$ in the outer regions. During the 70s, however,

it started to become clear that most galactic rotation curves do not exhibit such a fall-off [13–21]. The rotational velocity seemed to remain constant in the outer regions which, according to Einasto [4], could only be explained by assuming additional, non-luminous mass content in the outer regions. The mass content of these outer regions was estimated to outnumber luminous matter at least tenfold. Around the same time, measurements of the mass of hot X-ray emitting gas seemed not to be sufficient to hold clusters together[4] (see e.g. Gursky et al, 1972 [22]).

Towards the end of the seventies, the astrophysical community started to take the dark matter problem seriously, but it came with some troubling issues [3, 4]. If most of the matter in galaxies is neither gaseous nor stellar, then what is it? Perhaps more intriguing was the problem of Big Bang nucleosynthesis (BBN) – the production of atomic nuclei in the Early Universe. BBN suggests an underdense Universe with an energy density of about $\Omega = 0.04$ in units of the critical energy density $\rho_{\mathtt{crit}}$. If the amount of dark matter outnumbers the baryonic matter by a factor of about ten to one then, at least locally, one would expect densities closer to $\Omega = 0.2 - 0.3$. This, as we shall see in the next section, would mean that the Universe was less curved. If not curvature, then what makes the Hubble flow so smooth? More generally, how does the presence of dark matter affect the evolution of the Universe?

1.2 The Formation of Structures

In this section we briefly introduce the basics of cosmology and how structures in the Universe are thought to have formed, paying special attention to the role, and evolution, of Dark Matter. For completeness, let us start by reminding ourselves about some of the basic relations and terminology of general relativity and the evolution of a homogeneous Universe.

1.2.1 General Relativity and The Beginning of Time

The theory of general relativity is a generalization of the special theory of relativity taking gravitation into account – here as a purely geometric phenomenon arising from the intrinsic curvature of spacetime. The central assumption is the *Equivalence principle* stating that it is impossible to distinguish gravity from acceleration locally. This means that only freely falling reference frames are inertial. Therefore, inertial reference frames are linearly related only locally and the trajectory of inertial objects are no longer straight lines, but geodesics. Geodesics are curves that parallel transport their own tangent vector, which means that their parametrized coordinates $x^\mu(\lambda)$ are given by

$$\frac{dx^\nu}{d\lambda}\nabla_\nu\frac{dx^\mu}{d\lambda} = \frac{d^2x^\mu}{d\lambda^2} + \Gamma^\mu_{\rho\sigma}x^\rho x^\sigma = 0, \tag{1.4}$$

where $\Gamma^\mu_{\rho\sigma}$ are the Christoffel symbols. In fact, if λ is an affine parameter of the eigentime, then this is the extremal of the spacetime interval, or equivalently the

generalization of zero acceleration to curved spacetime.

The theory treats spacetime as a Riemannian manifold whose tangent spaces can be brought to a Minkowskian form, and whose metric $g_{\mu\nu}$ extremizes the *Hilbert action*

$$S = \int \left(\frac{R - 2\Lambda}{16\pi G} + \hat{\mathcal{L}}_M \right) \sqrt{-g} d^4x. \tag{1.5}$$

Here $-g$ is the absolute value of the determinant of the metric, $\mathcal{L}_M = \sqrt{-g}\hat{\mathcal{L}}_M$ is the Lagrangian density for the matter content and R is the Ricci scalar. For the metric $g_{\mu\nu}$ to extremize the Hilbert action S, it must satisfy the *Einstein Equations*

$$R_{\mu\nu} - \frac{1}{2} g_{\mu\nu} R + \Lambda g_{\mu\nu} = 8\pi G T_{\mu\nu} \tag{1.6}$$

where G is the gravitational constant, $R_{\mu\nu}$ is the *Ricci tensor*, Λ is the cosmological constant and $T_{\mu\nu}$ is the stress-energy tensor containing all the necessary information about the energy content of the Universe.

Solving Einstein's equations analytically is notoriously difficult. Actually, there are only a few known solutions, all corresponding to different symmetry situations. One of these solutions is the *Friedmann-Lemaitre-Robertson-Walker* (FRW) metrics describing universes that are path-connected and isotropic in every point. That the Universe as a whole can be approximated as isotropic in every point, called the *Cosmological principle*, can be argued for by combining the observational fact that the Universe on large scales is very isotropic with the so-called *Copernican principle*, stating that we are not privileged observers of the Universe. This translates into demanding a space-time that foliates into 3-dimensional, maximally symmetric, space-like sheets. Using spherical coordinates for the space-part, the metric can be written

$$g_{\mu\nu} dx^\mu dx^\nu = -dt^2 + a^2(t) \left[\frac{dr^2}{1 - \kappa r^2} + r^2 d\Omega \right] \tag{1.7}$$

where $a(t)$ is the *scale factor*, $d\Omega = d\theta^2 + \sin^2\theta d\phi^2$ is the standard metric on the 2-sphere and κ the spatial curvature when $a = 1$, which, unless otherwise stated, we take to be today. Note that we will refer to the vectors $(t, \mathbf{x})$ as *comoving* coordinates and $(t, a(t)\mathbf{x})$ as *physical* coordinates. If one further assumes the matter and radiation content to behave as a perfect fluid then, in the rest frame of the fluid, the Einstein equation can be summarized by the two *Friedmann equations*[*]

$$\Omega = 1 + \frac{\kappa}{\dot{a}^2} \tag{1.8}$$

$$\frac{\ddot{a}}{a} = -\frac{4\pi G}{3} (\rho + 3p) \tag{1.9}$$

where we have introduced the density parameter $\Omega \equiv \rho/\rho_c$ which is written in terms of the *critical energy density* $\rho_c \equiv 3H^2/(8\pi G)$ where $H \equiv \dot{a}/a$ is the *Hubble*

[*]Since the cosmological constant behaves as a perfect fluid with density $\rho_\Lambda = \Lambda/(8\pi G)$ and equation of state $\rho_\Lambda = -p_\Lambda$, it has been absorbed into ρ and p

parameter. The Hubble parameter has the nice interpretation that two objects at rest separated by a small distance r will have a relative velocity $v = Hr$. This velocity is referred to as the *Hubble velocity* or *Hubble flow*. For sufficiently distant objects, the Hubble velocity will equal the speed of light. This distance, $r = H^{-1}$, which is referred to as the *Hubble horizon*, is an estimate of how distant objects one can possibly affect with events here and now. Bear in mind, however, that since H changes with time, $r = H^{-1}$ is not an actual horizon, but rather an estimate of the radius $r = \int da/\dot{a}$ of the light cone.

Since physical wavelengths change with the scale factor a, light from distant objects will generally reach an observer with a different color than what was emitted. Due to this effect, it is customary to speak of the *redshift* $z \equiv a_{now}/a_{then} - 1$, sometimes referring to the time the Universe had the scale factor a_{then}, and sometimes to the comoving radial distance traversed by light during the growth from a_{then} to a_{now}.

From conservation of the stress-energy tensor ($\nabla_\mu T^\mu{}_0 = 0$) for each energy component, one can find that

$$\frac{\dot{\rho}_i}{\rho_i} = -3\,(1+\omega_i)\,\frac{\dot{a}}{a}. \tag{1.10}$$

where ρ_i is the energy density of component i and $\omega_i \equiv p_i/\rho_i$ its equation of state where p_i is the pressure. Assuming a constant equation of state, this is solved by $\rho_i \propto a^{-3(1+\omega_i)}$. Inserting this into equation (1.8) then, for a Universe with negligible curvature, one finds a differential equation for a whose solution is

$$a(t) \propto t^{\frac{2}{3(1+\omega)}}, \quad \text{for } \omega \neq -1\,. \tag{1.11}$$

This means that for matter, which has negligible pressure $p_M \simeq 0$, the energy density dilutes as the inverse volume $\rho_M \propto a^{-3}$. Moreover, the size of a purely matter-dominated Universe would evolve according to $a \propto t^{2/3}$. Since $p_R = 1/3\rho_R$ for radiation one finds $\rho_R \propto a^{-4}$ which corresponds to the energy density both redshifting and diluting [*]. Moreover, a radiation-dominated Universe would expand according to $a \propto t^{\frac{1}{2}}$, i.e. slower than a matter-dominated Universe. The energy density ρ_Λ corresponding to the cosmological constant, which by definition satisfies $\rho_\Lambda = -p_\Lambda$, is independent of the scale parameter $a(t)$. This means that the energy enclosed in a volume remains proportional to the volume as it expands. For this reason, one often refers to ρ_Λ as the energy density of space itself, or the *vacuum energy*. In a vacuum-dominated Universe, ρ is constant, so that for a flat Universe, equation (1.8) requires $H = \dot{a}/a$ to be constant. Therefore, the scale factor in a vacuum-dominated Universe evolves exponentially in time $a \propto \exp(Ht)$.

Looking backward in time, this means that at sufficiently early times the Universe was *radiation-dominated* (RD). After radiation-domination, the Universe entered an

[*] That the radiation-pressure is just the energy density distributed equally along the spatial directions can be seen by realizing that $p = \langle \mathbf{p}^2/(3E)\rangle\, n = \frac{1}{3}\langle E\rangle\, n = \frac{1}{3}\rho$ where $\mathbf{p}$ is the momentum, E is the energy and n is the number density.

epoch of *matter-domination* (MD), which is followed by the seemingly unstoppable epoch an exponential growth known as *vacuum-domination* (VD)*.

For much of its early history, the constituents of the Universe were in thermal equilibrium making it well approximated by equilibrium thermodynamics. Since the total energy density ρ at early times is dominated by the contribution from relativistic species, it is well approximated by

$$\rho = \frac{\pi^2}{30} g_{\mathrm{eff}}(T) T^4 \,, \tag{1.12}$$

where $g_{\mathrm{eff}}(T)$ counts the relativistic ($m_i \ll T$) number of degrees of freedom

$$g_{\mathrm{eff}} \equiv \sum_{i \in \mathrm{bosons}} g_i \left(\frac{T_i}{T}\right)^4 + \frac{7}{8} \sum_{j \in \mathrm{fermions}} g_j \left(\frac{T_j}{T}\right)^4 \,. \tag{1.13}$$

Here we have taken into account that a particle species i can have a thermal distribution with temperature T_i different from the photon temperature T. Combining the first Friedmann equation (1.8) for a flat, radiation-dominated Universe with the equilibrium relation (1.12), and using that in this case $H = 1/(2t)$, one can relate the age t of the Universe to its temperture T by

$$t = \sqrt{\frac{45}{16\pi^3 G}} g_{\mathrm{eff}}^{-1/2}(T) T^{-2} \simeq \frac{0.301 m_{\mathrm{pl}}}{\sqrt{g_{\mathrm{eff}}(T)}} T^{-2} \,, \tag{1.14}$$

where $m_{\mathrm{pl}} \equiv 1/\sqrt{G}$ is the Planck mass. More generally, since radiation dominates the entropy density, one has

$$s \simeq \frac{2\pi^2}{45} g_{\mathrm{eff},s}(T) T^3 \tag{1.15}$$

where $g_{\mathrm{eff},s}$ is defined as (1.13), but with the temperature ratios to the third power. From conservation of entropy ($a^3 s$) it follows that during periods of constant $g_{\mathrm{eff},s}$, the temperature T of the Universe in any epoch evolves according to

$$T \propto g_{\mathrm{eff},s}^{-1/3} a^{-1} \,. \tag{1.16}$$

For this reason, we think of the early, dense Universe as being extremely hot. In fact, at sufficiently early times the Universe would be so hot that one expects charged particles to be too energetic to combine into neutral particles. This means that the early Universe was an opaque plasma, referred to as the *primordial plasma*. As the Universe expands, the temperature cools, and at some point, the temperature is sufficiently low for electrons and protons to stick together and combine into electrically neutral atoms. The result is that photons thermally decouple from the other

*Strictly speaking, it is possible for exotic cosmologies to change the order of these epochs. For instance, if the Universe started out in MD, and at some point, the massive particles annihilated into radiative species, then MD could be followed by a period of RD. Note also that in a contracting Universe, the order would be reversed.

species, making the Universe transparent. Although this is the first time electrons and protons combine into neutral atoms, this event commonly goes under the rather unfortunate name of *recombination*. The photons freed from the primordial plasma during recombination can be detected today, although redshifted into the microwave band due to the expansion of the Universe. The spectrum, which is called the *Cosmic Microwave Background (CMB)* radiation, provides a unique window to the early Universe. It is a perfect black-body with temperature $(2.72548 \pm 0.00057)\mathrm{K}$ [23] and anisotropic temperature fluctuations of about $\delta T/T \simeq 8 \times 10^{-5}$ [24]. Measurements of the CMB anisotropies have played a crucial role in arriving at the standard model for cosmology – the ΛCDM-model. The ΛCDM model claims a flat, 13.8 billion year old Universe, with Hubble constant $H_0 = (67.74 \pm 0.46)\mathrm{km/s/Mpc}$, matter content (today) of 30.9%, 4.9% baryons and 26.0% Cold Dark Matter, and 69.1% vacuum energy [10] *. We will soon see what exactly is meant by *Cold Dark Matter*, but first, we should briefly explain why Dark Matter is a crucial ingredient in the cosmological energy budget.

1.2.2 The Need for a Decoupled Species

In this section we aim to state some of the key aspects of linear cosmological structure formation, and why it serves as a strong argument for the presence of dark matter. For more detailed reviews, the reader is invited to consult dedicated texts like [26–28].

Since the anisotropic temperature fluctuations in the CMB is of the order $\delta T/T \sim \mathcal{O}(10^{-5})$ then, according to the Stefan-Boltzmann law, we therefore expect the energy density ρ of the species in equilibrium with the black-body to have anisotropies $\delta\rho$ of roughly the same order†. Let us now look at how these early, small density variations will evolve on small scales. On scales much smaller than the Hubble horizon H^{-1}, the cosmological fluid has non-relativistic velocities, which means it should be well described by Newtonian fluid equations. In fact, the first order effect for perturbations in velocity $\mathbf{v}$, density ρ, pressure p, and gravitational potential Φ using the Euler equation, Poisson equation and continuity equation, expressed in comoving coordinates ($\mathbf{x} \equiv \mathbf{r}/a$), can be combined into one equation

$$\ddot{\delta}_k + 2H\dot{\delta}_k + \frac{c_s^2 k_J^2}{a^2}\left[\frac{k^2}{k_J^2} - 1\right]\delta_k = 0. \tag{1.17}$$

Here $\delta_{\mathbf{k}}$ is the Fourier mode of the *density contrast* $\delta(\mathbf{x}) \equiv \delta\rho(\mathbf{x})/\rho$ with wavenumber $\mathbf{k}$, $c_s = \sqrt{\delta p/\delta\rho}$ is the speed of sound and $k_J \equiv \sqrt{4\pi G\rho a^2}/c_s$ is the *Jeans*

*The value for the Hubble constant is purely from measurements of the CMB. There is a tension between this estimate and the local Hubble constant $H_0 = (73.24 \pm 1.74)\mathrm{km/s/Mpc}$ from distance ladder measurements [25].

†More precisely, one would have $\delta\rho/\rho = 4\delta T/T \sim 10^{-5}$. Note, however, that the light received from CMB has traveled for a long time. The temperature fluctuations will therefore also depend on the velocity redshift and frequency variations due to the light escaping peaks and valleys in the gravitational potential.

wavenumber. Note that for wavenumbers $k \gtrsim k_J$, the equation takes the form of an harmonic oscillator with frequency

$$\omega \simeq \frac{c_s}{a}\sqrt{k^2 - k_J^2} \tag{1.18}$$

that is damped by the expansion term $2H\dot{\delta}_k$. In other words, there will be no growth in density variations smaller than the *Jeans scale*

$$\lambda_J \equiv 2\pi/k_J \text{ for } k_J \equiv \frac{\sqrt{4\pi G\rho a^2}}{c_s}\,. \tag{1.19}$$

Physically, the Jeans scale can be understood as the scale where the fluid pressure starts to counteract gravitational collapse.

On scales larger than the Jeans scale ($k \ll k_J$), where the pressure is negligible, one has

$$\ddot{\delta}_k + 2H\dot{\delta}_k = 4\pi G\rho\delta_k\,. \tag{1.20}$$

In a matter-dominated, flat Universe $a(t) \propto t^{2/3}$, $H = \frac{2}{3t}$ and $\rho = \rho_c \equiv 3H^2/(8\pi G)$, so that in the case of negligible pressure the density contrast evolves according to

$$\ddot{\delta}_k + \frac{4}{3t}\dot{\delta}_k = \frac{2}{3t^2}\delta_k\,. \tag{1.21}$$

This equation is solved by a decaying mode $\delta_k \propto t^{-1}$ and a growing mode $\delta_k \propto t^{2/3} \propto a(t)$. Since our Universe, after recombination, is well described as matter-dominated and flat, we can now calculate what the density contrast would be today if it was of the order $\delta \sim 10^{-5}$ at the time of CMB. Since the Universe was about 1100 times smaller at recombination [10], the density contrast would have evolved to

$$\delta(\text{today}) \simeq 1100 \cdot 10^{-5} \simeq 10^{-2}. \tag{1.22}$$

This is still in the linear perturbation level ($\delta \ll 1$), which means that the Universe would not have had time to form astrophysical objects by today. That is, if most of the matter was coupled to the primordial plasma at recombination, the Universe would still be homogeneous with density variations of the order of one to one hundred. In other words, to explain the formation of structures one needs a stable and abundant species that was unaffected by the photon pressure of the primordial plasma. Density perturbations in such a species would be able to grow inside the primordial plasma, and thus provide potential wells for the baryonic particles to fall into once they are released from the plasma. Note that in order for this to work, the perturbations of the Dark Matter component must have been at least $\delta_{dm} \sim 1/1100 \sim 10^{-3}$ at recombination to explain the formation of structures within today. This conclusion, which remains roughly the same in more devoted calculations, should be taken as a strong argument for the presence of Dark Matter and its exotic nature.

In fact, the growth is even slower in a radiation dominated Universe. Equation (1.17) can be naturally extended to the case of multiple fluid components with densities $\{\rho_i\}$ and density contrasts $\{\delta_i\}$ as follows:

$$\ddot{\delta}_i + 2H\dot{\delta}_i + \left[\frac{c_{s,i}^2 k^2}{a^2}\delta_i - \sum_j 4\pi G\rho_j\delta_j\right] = 0\,. \tag{1.23}$$

Consider now the evolution of density variations δ in a matter-fluid during radiation domination ($H = \frac{1}{2t}$). If the radiation component is smooth ($\delta_\gamma = 0$), then the Jeans unstable perturbations ($k \ll k_J$) will follow the equation $\ddot{\delta} + \dot{\delta}/t = 0$, which is solved by $\delta(t) = \delta(t_0)[1 + C\ln(t/t_0)]$ where t_0 is some reference time. That is, if the density mode is large enough not to be a damped oscillator ($k \ll k_J$) then it will grow logarithmically with time. Actually, if the initial growth is negligible ($\dot{\delta} \simeq 0$) then $C \simeq 0$, meaning that the density contrast will stagnate. The scenario seems to be as follows: While density perturbations in the baryonic fluid are damped by the photon pressure of the primordial plasma, variations in the dark matter component grows logarithmically until the time of matter-radiation equality, where growth becomes more efficient. After recombination, when protons and electrons combine into neutral particles, the baryonic component "falls" into the potential wells formed by overdensities in the Dark Matter component.

For modes larger than the Hubble horizon H^{-1}, the picture is more complicated due to the density contrast $\delta \equiv \delta\rho/\rho$ being gauge dependent in the full relativistic treatment. It turns out, however, that the evolution of scalar, adiabatic super-horizon sized modes can be summarized by the gauge-invariant quantity $\delta\rho/(\rho + p)$ being constant [26].

As the Hubble horizon $H^{-1} \propto t$ grows, it will catch up with physical perturbation wavelengths λ that were once outside the horizon. For this reason, it is customary to refer to the time where the perturbation size equals the horizon as *horizon crossing*.

Before moving on, there is something that cannot remain uncommented – the density perturbations specified at any given time will generally depend on the initial spectrum! There is a wide range of reasons for postulating an epoch, referred to as *inflation*, of exponential growth prior to radiation-domination. Most simple models of inflation predict the initial scalar perturbation modes $\delta_{\mathbf{k}}$ to be a Gaussian random field that is uncorrelated (see e.g. [29])

$$\langle \delta_{\mathbf{k}}\delta_{\mathbf{k}'}\rangle = \frac{2\pi^2}{k^3}\delta^{(3)}(\mathbf{k} - \mathbf{k}')\mathcal{P}(k)\,, \tag{1.24}$$

where $\mathcal{P}(k)$ is referred to as the *power spectrum*. Moreover, it is both a prediction of simple inflation models and consistent with data that the power spectrum, when specified at the time t_{HOR} of horizon crossing, to be given by a feature-less power law [30]

$$\mathcal{P}(k)\big|_{t_{HOR}} \propto k^{1-n_s} \tag{1.25}$$

where n_s is referred to as the *spectral index*. Using the Planck data, the estimated value for the spectral index has been found to be $n_s = 0.9667 \pm 0.0040$ [24], which

is well approximated by the so-called *Harrison-Zel'dovich* spectrum with $n_s = 1$ [31–33]. Note that since perturbations are assumed to be Gaussian, some (rare) modes are expected to enter horizon crossing with very large overdensities δ_k. If the overdensity is roughly of order unity, $\delta_k \sim 1$, then it will collapse into a black hole [34, 35]. Such black holes are referred to as *Primordial Black Holes* (PBHs) and may, unlike black holes of stellar origin, have masses well below the Chandrasekhar limit of $1.4 M_\odot$.

1.2.3 The Collapse of Overdensities

At some point, growing overdensities $\delta\rho$ will become sufficiently large for the gravitational force to counteract the dilution due to the expansion of the Universe. This results in collapse into objects that are, in a sense, decoupled from the expansion of the Universe. In this section, we present a simple analytical model, referred to as the *Spherical Collapse model*, for estimating the density contrast needed for collapse, and the asymptotic size of the resulting object.

From the first Friedmann equation (1.8), we expect a spherical, homogeneous overdensity $\delta\rho$ in an otherwise flat, homogeneous, matter-dominated Universe to behave locally as a closed Universe*. The evolution of the scale factor $a(t)$ in a closed Universe can be stated in parametric form as

$$a(\theta) = \frac{\Omega_{m0}}{2(\Omega_{m0} - 1)}(1 - \cos\theta) \tag{1.26}$$

$$t(\theta) = \frac{\Omega_{m0}}{2H_0(\Omega_{m0} - 1)^{3/2}}(\theta - \sin\theta) \tag{1.27}$$

where $\Omega_{m0} > 1$ is the density parameter of the overdense region at some early time ($\Omega_{m0} - 1 \ll 1$), H_0 is its Hubble parameter and $\theta \in (0, 2\pi)$. Note that at sufficiently early times ($\theta \ll 1$) then, to leading order, $a(t) \propto t^{2/3}$. That is, to first order, the overdensity evolves with the flat, outside Universe. The size of the overdense region will, however, reach a maximal value at $\theta = \pi$, which is followed by a collapse into $a = 0$ at $\theta = 2\pi$. At the maximum, one therefore has

$$a_{max} = \frac{\Omega_{m0}}{\Omega_{m0} - 1} \text{ and } t_{max} = \frac{\pi\Omega_{m0}}{2H_0(\Omega_{m0} - 1)^{3/2}}. \tag{1.28}$$

Assuming matter domination both in the spherical overdensity and in the background Universe, we find $\rho/\rho_b = \Omega_{m0}(a/a_b)^{-3}$ where ρ_b is the density of the background and $a_b(t) = (3H_0 t/2)^{2/3}$ its scale factor. This means that the overdensity will acchieve its maximal size when its density is a factor

$$\frac{\rho_{max}}{\rho_b} = \frac{\Omega_{m0} a_{max}^{-3}}{a_b^{-3}(t_{max})} = \frac{9\pi^2}{16} \simeq 5.55 \tag{1.29}$$

*This argument can be formally motivated in a rigorous manner by considering a manifold consisting of tho different FRW manifolds stitched together [26, 36].

larger than the background. If the matter fluid is perfectly collisionless, then the overdensity will collapse into zero size ($a_{coll} = 0$) at $\theta_{coll} = 2\pi$. Physically, this scenario would correspond to collapse into a black hole. Most overdensities, however, are not perfectly spherical and homogeneous, which makes the collapse much more complicated than it appears in the spherical collapse model. The result of this process, known as *violent relaxation*, is a collapsed, virialized object whose time averaged kinetic energy $\langle T \rangle$ equals $-\frac{1}{2}\langle V \rangle$, where V is the gravitational potential energy. Using that $\langle T \rangle = 0$ at t_{max} then energy conservation implies $R_{max} = 2R_{vir}$. In other words, the virialized object will be a factor $2^3 = 8$ denser than at t_{max}. If we take $t_{coll} \equiv t(2\pi)$ to be the virialization time, then the background density has grown by a factor

$$\frac{\rho_{b,vir}}{\rho_{b,max}} = \left(\frac{t_{vir}}{t_{max}}\right)^2 = 4. \tag{1.30}$$

This means that in an otherwise flat, matter dominated Universe ($\rho_b = \rho_{crit}$), the density of the virialized object is given by

$$\rho_{vir} = 5.55 \cdot 8 \cdot 4 \cdot \rho_{crit} \simeq 178\rho_{crit} \tag{1.31}$$

where ρ_{crit} is the critical density of the Universe at the time of virialization. This means that perturbations form gravitationally bound structures when its density is roughly 178 times larger than the mean density of the Universe. Recall that in this highly simplified model for the collapse of overdensities, we assume a flat, matter-dominated Universe, with a single, perfectly spherical, homegeneous overdensity. We should, therefore, not take the value $178\rho_{crit}$ as anything more than a rough estimate. In fact, to avoid the misconception that $178\rho_{crit}$ is accurate to three leading digits, we will use

$$\rho_{vir} \simeq 200\rho_{crit}\,, \tag{1.32}$$

as is customary, throughout this thesis. This being said, we know from cosmological N-body simulations that the spherical collapse model captures the general picture of the collapse up to a factor of order unity, see e.g. [37].

Since $a(\theta)$ and $t(\theta)$ expanded to leading order yield the evolution of the background spacetime, the next-to-leading expansion should correspond to the evolution of overdensities in the linear regime. Using that

$$\frac{a(\theta)}{a_{max}} \simeq \frac{1}{4}\theta^2\left(1 - \frac{\theta^2}{12}\right) \tag{1.33}$$

$$\frac{t(\theta)}{t_{max}} \simeq \frac{\theta^3}{6\pi}\left(1 - \frac{\theta^2}{20}\right) \tag{1.34}$$

one can, after some algebra, reach the expression

$$\frac{a(t)}{a_{max}} \simeq \frac{1}{4}\left(6\pi\frac{t}{t_{max}}\right)^{2/3}\left[1 - \frac{1}{20}\left(6\pi\frac{t}{t_{max}}\right)^{2/3}\right] \tag{1.35}$$

for the linear evolution of $a(t)$, where the first factor is the evolution of the background with density ρ_{crit}. Now, using that $\rho \propto a^{-3}$ during matter-domination and $\rho = \rho_{crit}(1+\delta)$, we can identify

$$(1+\delta)^{-1/3} = 1 - \frac{1}{20}\left(6\pi \frac{t}{t_{max}}\right)^{2/3} \tag{1.36}$$

and since $(1+\delta)^{-1/3} \simeq 1 - \delta/3$ in the linear regime ($\delta \ll 1$), we see that the linear theory would have predicted a density contrast of

$$\delta_{lin} \simeq \frac{3}{20}(12\pi)^{2/3} \simeq 1.686 \tag{1.37}$$

at the time of collapse $t = t_{coll}$.

1.2.4 The Smallest Clumps

We have now seen that overdensities of wavelength smaller than the Hubble horizon H^{-1} and, in the case of baryons, larger than the Jeans scale λ_J (1.19) will grow. Furthermore, the density contrast $\delta \equiv \delta\rho/\rho$ of a matter component inside the Hubble horizon grows proportional to the scale factor $a(t)$ during matter domination and logarithmically in time during radiation domination.

Small perturbations in the Dark Matter component will also be subject to a damping effect. Since the Dark Matter fluid is collision-less, the perfect fluid assumption will at some sufficiently small scale break down. This scale, which we will refer to as the *free streaming scale* λ_{fs}, corresponds roughly to the distance freely traveled by the particles in the medium prior to the matter-domination epoch of efficient growth. For all initial power spectra that decrease with increasing length scales (see (1.24) and (1.25)), it turns out that the free streaming scale sets the scale on which the first structures form (see e.g. [26]).

Now, let us try to obtain a rough estimate of the free streaming scale λ_{fs}. In doing so, we will assume the Dark Matter to have previously been in thermal equilibrium with the primordial plasma. We therefore restrict ourselves to the class of dark matter candidates referred to as *thermal Dark Matter*.

The free streaming scale can be thought of as the comoving distance traveled by individual dark matter particles from the time of kinetic decoupling t_{kd} to the time they start to feel the presence of gravitational potentials. Since efficient growth starts at matter-radiation equality t_{EQ}, let us assume that this is the time where gravitational potentials become significant. If the time t_{NR} the particle becomes non-relativistic is well before t_{EQ}, then the velocity of the particle will typically be so redshifted that the free streaming after t_{EQ} will anyway be negligible. If we further take kinetic decoupling to be early, i.e. $t_{kd} \approx 0$, the free streaming scale can

be approximated by *

$$\lambda_{fs} \simeq \int_0^{t_{EQ}} \frac{v(t)dt}{a(t)} \simeq \int_0^{t_{NR}} \frac{cdt}{a(t)} + \int_{t_{NR}}^{t_{EQ}} \frac{v(t)dt}{a(t)} \simeq \frac{t_{NR}}{a_{NR}} \left[2 + \ln\left(\frac{t_{EQ}}{t_{NR}}\right)\right] . \quad (1.38)$$

Note that in the limiting case of the particle becoming non-relativistic at equality, i.e. $t_{NR} = t_{EQ}$, the free streaming scale will be very large. In this case the first objects to form will have mass much larger than galaxies [26] and structure formation will proceed in a "top-down" manner where large objects form first, and later break up into smaller objects. In this scenario, which is referred to as *Hot Dark Matter*, there would be no objects with Milky-Way size [26]. This, amongst multiple other reasons, is why we think the Dark Matter is not hot. Neutrinos are the only particles in the Standard Model that are are stable and feebly interacting enough to, at least in principle, serve as viable Dark Matter candidates. Since a thermal species χ becomes non-relativistic when $T_\chi \lesssim m_\chi/3$ †, however, the small neutrino mass means they become non-relativistic at late times and thus act as hot dark matter. For this reason, the Standard Model neutrinos can be excluded as a Dark Matter candidate (see e.g. [38] for the Lyman-α constraints). Additionally, being fermions, the number N_ν of neutrinos in an object of size R is limited by the available phase space, i.e. $N_\nu \lesssim p^3R^3$. If neutrinos were the dominating matter component in galaxies, then Pauli blocking would prevent them from being sufficiently slow moving in the halo.

The case where Dark Matter becomes non-relativistic long before it kinetically decouples from the plasma ($t_{kd} \gg t_{NR}$) is referred to as *Cold Dark Matter* (CDM) – this is the CDM in the ΛCDM model. For CDM, the damping will, in addition to free streaming, also be set by a remaining viscous coupling to the primordial plasma. Crucially, this damping scale is determined by the decoupling temperature T_{kd}, the thermally averaged scattering cross section, and the mass m_χ of the Dark Matter particle. To determine the decoupling temperature properly T_{kd}, however, one needs to trace the evolution of the phase space distribution function f of the Dark Matter particle. This is exactly what the Boltzmann equation $\mathbb{L}[f] = \mathbb{C}[f]$, $\mathbb{L}$ being the Liouville operator and $\mathbb{C}$ the collision operator, is made for. For brevity, we will not solve the Boltzmann equation here and instead recite the result of one such calculation‡: For Dark Matter particles χ interacting with the weak force, the characteristic mass M_{fs} that is damped by free streaming can be estimated as

$$M_{fs} \simeq 2.9 \times 10^{-6} M_\odot \left[\frac{1 + \ln\left(g_{eff}^{1/4} \frac{T_{kd}}{50MeV}\right)/19.1}{\left(\frac{m_\chi}{100GeV}\right)^{1/2} g_{eff}^{1/4} \left(\frac{T_{kd}}{50MeV}\right)^{1/2}}\right]^3 \quad (1.39)$$

*Using that $a(t) \propto \sqrt{t}$ during radiation domination the first term can be written as $2t_{NR}/a_{NR}$ and since non-relativistic velocities simply redshift $v(t) \propto a^{-1}(t)$ with time, the final expression follows.

†This relation follows naturally from identifying the thermal energy $\frac{3}{2}k_B T$ with the kinetic energy $\frac{1}{2}mv^2$ of the particles involved.

‡For a proper discussion, the reader is invited to consult texts such as [39].

where m_χ is the mass of the Dark Matter particle [40]. Since $g_{eff} \simeq 10.75$ at $T_{kd} \simeq 30MeV$, a dark matter particle with mass $m_\chi \simeq 100GeV$ that decouples at $T_{kd} \simeq 30MeV$ has a characteristic free-streaming mass of roughly $M_{fs} \simeq 5 \times 10^{-7} M_\odot$ *. In other words, in a Universe with a weakly interacting Dark Matter particle with mass $m_\chi \simeq 100GeV$ that thermally decouples at $T_{kd} \simeq 30MeV$, the first objects to form are expected to have mass roughly like that of the Earth ($\sim 10^{-6} M_\odot$). Note, however, that the cut-off scale may vary by many orders of magnitude depending on the particle mass and the scattering cross section, see e.g. [40, 41].

1.2.5 The Miraculous WIMP and its Contenders

Assuming a thermal species that started off in chemical equilibrium with the Standard Model particles, its departure from equilibrium will determine the present abundance of that species. When integrating out the momentum dependence of the Boltzmann equation for a flat NFW spacetime, one can recognize the number density n to bring the equation into the following form

$$\partial_t n + 3Hn = \langle \sigma v \rangle \left(n_{eq}^2 - n^2 \right) , \tag{1.40}$$

where n_{eq} is the equilibrium number density and $\langle \sigma v \rangle$ is the thermally averaged total annihilation cross section σ times the *Møller velocity* v. To be precise, in arriving at this result one must assume the Dark Matter particles χ to be stable, that there is no asymmetry in the number density of χ and its anti-particle $\overline{\chi}$, and that the dominating annihilation process is of the form $\chi\overline{\chi} \to Y\overline{Y}$, where Y generically denotes the species χ can annihilate into. Note also that the species Y are assumed to have thermal equilibrium distributions with zero chemical potential and that all particles are assumed to obey Maxwell-Boltzmann statistics.

Note that before departure from chemical equilibrium, when the annihilation and production rate $\Gamma = n_{eq} \langle \sigma v \rangle$ is larger than the Hubble rate H, the number density will converge to its equilibrium value $n = n_{eq}$. If, on the other hand, $\Gamma > H$, the number density dilutes with the expansion, i.e. $n \propto a^{-3}$.

If we assume thermal equilibrium during decoupling, we may invoke entropy conservation $\partial_t a^3 s = 0$ so that the left hand side of equation (1.40) can be written in the form

$$\partial_t n + 3Hn = a^{-3} \partial_t (a^3 n) = a^{-3} \left[a^3 s \partial_t \frac{n}{s} \right] . \tag{1.41}$$

Therefore, by introducing the variable $Y \equiv n/s$, the integrated Boltzmann equation takes the form

$$\dot{Y} = -s \langle \sigma v \rangle \left(Y^2 - Y_{eq}^2 \right) . \tag{1.42}$$

Taking advantage of the relation between time and temperature (1.14), we can

*At temperatures around $30MeV$, the only particles coupled to the primordial plasma are photons ($g_\gamma = 2$), electrons ($g_{e^-} = 2$ and $g_{e^+} = 2$) and the three generations of neutrinos ($3 \times g_\nu = 3 \times 2 = 6$). From the definition (1.13) is then follows that $g_{eff} \simeq 10.75$.

introduce the variable $x \equiv m_\chi/T$ by

$$t \simeq \frac{0.301 m_{pl}}{g_{eff}^{1/2}} \frac{x^2}{m_\chi^2} \tag{1.43}$$

so that the equation takes the form [42]

$$\frac{dY}{dx} = -\frac{s \langle \sigma v \rangle}{x \tilde{H}} \left(Y^2 - Y_{eq}^2 \right) . \tag{1.44}$$

Here $\tilde{H} = H/(1 + \tilde{g})$, where H is the Hubble parameter and

$$\tilde{g} \equiv \frac{1}{3} \frac{T}{g_{eff,s}} \frac{dg_{eff,s}}{dT} . \tag{1.45}$$

The asymptotic value for Y is easily found for hot Dark Matter, for which chemical decoupling happens at $x_f \lesssim 3$. In that case the equilibrium value Y_{EQ} will stay roughly constant leading to a present abundance of roughly $n = s_0 Y_{EQ}(x_f) \simeq 800 g_{eff,\chi}/g_{eff}(x_f) cm^{-3}$ quite insensitive to the details of decoupling. Here $g_{eff,\chi} = g_\chi$ if χ is a boson, and $g_{eff,\chi} = (3/4) g_\chi$ if it is a fermion, g_χ being the internal degrees of freedom for χ (see e.g. [26]). For cold Dark Matter, on the other hand, the asymptotic abundance depends strongly on the details of chemical decoupling. If one parametrizes $\langle \sigma v \rangle \equiv \sigma_0 x^{-n}$ and pretends that $\tilde{g} = 0$, the asymptotic value for the density parameter can be stated as (see [26])

$$\Omega_\chi \simeq 7.43 \times 10^{-20} \frac{(n+1) x_f^{n+1} g_{eff}^{1/2}}{g_{eff,s}} \left(\frac{pb}{\sigma_0} \right) \tag{1.46}$$

Now, at energies much lower than the mass of the W boson ($m_W \simeq 80.4 GeV$), a typical annihilation cross section with weak interactions behaves as [28]

$$\sigma_0 \sim m_\chi^2 \alpha^2 / m_W^4 \sim 10^{-20} pb \left(\frac{m_\chi}{GeV} \right)^2 . \tag{1.47}$$

This means that a massive $m_\chi \sim GeV$ Dark Matter particle that is weakly interacting and chemically decouples with $x_f \sim \mathcal{O}(10)$ naturally produces relic densities of order unity. In other words, a stable and massive particle that is weakly interacting and decouples around $T_f \sim \mathcal{O}(GeV)$ can naturally produce the correct relic density of Dark Matter ($\Omega_{dm} \simeq 0.26$).

This should, however, be considered as a rough estimate. For example, including the effects of a varying number of degrees of freedom actually changes the result quite a lot. See e.g. Figure 3 of [43] for the thermally averaged cross section needed to produce the correct relic density.

The viability of these *Weakly Interacting Massive Particles*, or *WIMPs*, as Dark Matter candidates is sometimes referred to as the *WIMP miracle*. The miracle belongs to the fact that particle physicists, in trying to address the shortcomings of the

Standard Model, has independently predicted stable WIMPs. Examples of WIMP candidates include the Lightest Supersymmetric Particle (LSP) and the Lightest-Kaluza-Klein particle (LKP). There are multiple large, international search programmes looking for the elusive WIMP, and consequences of the theories that predict them. These include probing the production mechanism through collider searches (see e.g. [44]), the scattering with standard model particles (direct detection) [45], and the annihilation channels (indirect detection) [46].

There are, of course, a wide range of viable and well-motivated non-WIMPy candidates. One of the most popular is the *Axion*, which are the pseudo-Nambu–Goldstone bosons spawned from the spontaneous breaking of a $U(1)$ symmetry (Peccei-Quinn), invented to solve the so-called *strong CP problem*. The Axions were never in thermal equilibrium as they attain their mass at the QCD phase transition, and thus have a very different production mechanism than the WIMPs.

Later, we will mention the Massive Astrophysical Compact Halo Objects, or *MACHOs*, as a Dark Matter candidate. These are compact objects consisting of baryonic matter, and therefore strongly disfavored by structure formation which needs a species that were initially decoupled from the primordial plasma. As we shall see, the MACHO Dark Matter model is essentially ruled out, but bear in mind that this does not mean that the existence of MACHOs is ruled out. One certainly expect some MACHOs to be around, although not with the abundance required to solve the Dark Matter problem.

One non-particle candidate that has received a lot of attention lately is the *Primordial Black Hole Dark Matter* (PBH DM). Although, as we will see later, the model with a monochromatic mass spectrum of Primordial Black Holes are essentially ruled out by gravitational lensing, a wide mass distribution has been argued to both evade the current constraints, solve many of the problems of Dark Matter, and fit well in with the LIGO observations of gravitational waves from black hole mergers [47].

1.2.6 The Structure and Abundance of Halos

We have finally reached the section where we can discuss the present day abundance and structure of the collapsed and virialized Dark Matter overdensities, referred to as *halos*. Let us start by briefly reciting what is known about their structure.

From N-body simulations of structure formation with cold Dark Matter, halos have been found to be well fitted by the mass density [48]

$$\rho_{NFW}(R) = \frac{\rho_s}{\frac{R}{R_s}\left(1+\frac{R}{R_s}\right)^2} \tag{1.48}$$

referred to as the *Navarro-Frenk-White (NFW) profile*. Here the *scale radius* R_s is the radius that separates the inner $\rho(R) \sim 1/R$ profile from the outer $\rho \sim 1/R^3$ profile. Note that there are no free shape parameters of the halo profiles. That is, according to Navarro, Frenk and White [48], all cold Dark Matter halos are well

approximated by an inner, cuspy, profile of $1/R$ and an outer profile of $1/R^3$. Of course, the NFW profile cannot be exactly true seeing that the density diverges at the center and that the contained mass logarithmically diverges with R. Actually, this profile only makes sense so long as the average density

$$\bar{\rho}(R) = \frac{M_{enc}(R)}{\frac{4}{3}\pi R^3}\,, \tag{1.49}$$

is less than the virial density $\rho_{vir} \simeq 200\rho_{crit}$, where

$$M_{enc}(R) = \int 4\pi R^2 \rho(R) dR = 4\pi\rho_s R_s^3 \left[\ln\left(\frac{R_s + R}{R_s}\right) - \frac{R}{R_s + R}\right] \tag{1.50}$$

is the mass enclosed in a sphere of radius R. By defining the virial radius R_{vir} to be the radius at which $\bar{\rho}(R_{vir}) = \rho_{vir}$ we can therefore write

$$\rho_s = \frac{\rho_{vir} C^3}{3f(C)} \text{ for } f(C) = \ln(1 + C) - \frac{C}{1 + C} \tag{1.51}$$

where $C \equiv R_{vir}/R_s$ is the *concentration* parameter. If we also introduce the *virial mass* $M_{vir} \equiv M_{enc}(R_{vir})$ we may express the scale radius as

$$R_s = \frac{1}{C}\left(\frac{3M_{vir}}{4\pi\rho_{vir}}\right)^{\frac{1}{3}}\,. \tag{1.52}$$

As pointed out in the original paper [48], the virial mass M_{vir} and the concentration C are highly correlated for WIMPs (see e.g. [49]). This means that the density profile of WIMP halos are effectively determined by their virial mass M_{vir}.

The NFW profile was, however, determined from N-body simulations containing Dark Matter only. Measurements of the rotation curves of low-surface-brightness (LSB) galaxies suggest the inner density to be more like a core $\rho \simeq$ const (see e.g. [50]). This mismatch between the inner, cuspy $1/R$ profile predicted by pure Dark Matter simulations and the cored $\rho \simeq$ const profiles suggested by rotation curves is called the *cusp-core problem*. It has been shown that feedback from star formation in the baryonic component can transform a cuspy profile into a cored one [51, 52]. Alternatively, it has been shown that cored profiles may also form if one allows Dark Matter to be slightly self-interacting [53]. Moreover, explaining the core-cusp problem with baryonic feedback has proven difficult for Dwarf galaxies ($\sim 10^8 M_\odot$), for which simulations predict very diverse rotation curves [54]. In fact, it has also been argued that cusps may appear more like cores for halos that are not spherically symmetric [55]. In any case, the inner density of Dark Matter halos that are too small to house star formation remains unclear.

Another problem that refers to the mismatch of simulations and observation is the so-called *Missing satellites problem*. This refers to the problem that Cold Dark Matter simulations tend to predict many more satellite galaxies than observed. As argued by [56], the missing satellites problem can, by extrapolating the number

of observed Ultra-Faint Dwarf Galaxies (UFDGs) to the whole galaxy, be resolved by correcting for detection efficiency. In other words, there is no missing satellites problem, but rather a *faintness problem* [47]. That is, what prevents star formation in satellite galaxies from being effective? Also, the faintness problem has a possible solution, namely: maybe the satellite dark matter halos get stripped of their baryonic content via interactions with the host galaxy? This, however, introduces yet another problem – the *too big to fail* problem. Some of the satellite galaxies predicted by simulations are simply too big to lose their baryonic content in this way (see e.g. [57]).

Numerous formalisms for predicting the abundance of halos analytically has been developed. One of the more popular is the *Press-Schechter* formalism (see [58]) which assumes the fraction of Dark Matter $F(>M,t)$ contained in halos larger than M at time t to equal twice the probability $P(\delta_M(t) > \delta_{crit})$ that an overdensity δ_M with contained mass M is larger than the critical value for collapse, i.e. equation (1.37) *.

The point of these formalisms is to reach an expression for the so-called *Halo mass function* $\frac{dn}{d\log M}$, which is the number density of Dark Matter halos per logarithmic interval of M. In the case of cold dark matter, one expects that for small masses, the number density scales roughly as $\frac{dn}{d\log M} \propto M^{\alpha-1}$, for some small α, which is determined by the mass variance at the scale of interest. This would, however, mean that the total mass

$$M_{tot} = \int_{M_{min}}^{M_{max}} M \frac{dn}{d\log M} d\log M = \left[\frac{M^\alpha}{\alpha}\right]_{M_{min}}^{M_{max}} \tag{1.53}$$

contained in halos would diverge as $M_{min} \to 0$ and $\alpha \to 0$. This is fixed by recalling that the damping scale of the early Dark Matter perturbations leads to an exponential cut-off in the power spectrum, and thus also in the halo mass function [59]. In other words, locating the cut-off in the halo mass function could determine the damping scale and thus provide valuable insight into the nature of Dark Matter. For example, the cut-off predicted by the Super Symmetry (SUSY) neutralino Dark Matter is roughly between $10^{-4}M_\odot$ and 10^{-11} depending on the neutralino mass [40].

What makes measurements of the small-scale halo mass function hard is the lack of luminous mass trapped in these halos. This means that there are essentially two ways of detecting these clumps: either by detection of particles that result from Dark Matter interactions or by observing their gravitational effects. This thesis is devoted to the latter, taking advantage of the deflection of light in a gravitational field.

*The need for the factor of two in the assumption $F(>M,t) = 2P(\delta_M(t) > \delta_{crit})$ belongs to the fact that half the overdensities are expected to be underdense, i.e. $\delta_M(t) < 0$.

Chapter 2

Gravity as Deflector of Light

2.1 Gravitational Lensing

Assuming the validity of General relativity, the trajectory of light can be described as following null geodesics $g_{\mu\nu}dx^\mu dx^\nu = 0$ of the spacetime metric $g_{\mu\nu}$. For most astrophysically relevant scenarios, however, the effects predicted by General relativity can be translated into classical optics in a formalism referred to as the *Gravitational Lensing Formalism*. This section seeks to introduce the basics of this formalism, for a more complete introduction, see e.g. [60].

2.1.1 Light Propagating in a Gravitational Potential

The curving of space-time due to the presence of massive objects reduces the coordinate speed of light. This gives rise to so-called *Shapiro delay* where, to first order, light that passes through a gravitational potential Φ will exhibit a time-delay $dt = 2\Phi/c^3 d\ell$ for every differential length $d\ell$ it traverses. More importantly, this means that a gravitational potential configures a varying index of refraction which, due to its geometric origin, produces lens effects absent of chromatic aberrations[†]. In most astrophysically relevant scenarios, the space-time curvature is sufficiently weak to be considered as a perturbation of the Minkowskian space-time. Assuming static sources and matter to behave as a perfect fluid, the perturbed Minkowski spacetime (expressed in transverse gauge) takes the form

$$g_{\mu\nu}dx^\mu dx^\nu = -\left(1+\frac{2\Phi}{c^2}\right)c^2dt^2 + \left(1-\frac{2\Phi}{c^2}\right)d\mathbf{x}^2 \tag{2.1}$$

where $d\mathbf{x}^2$ should be understood as the Euclidean line element $dx^2+dy^2+dz^2$ and Φ is the Newtonian gravitational potential. Using that light travels along null-

[†]The absence of chromatic aberrations in gravitational lenses can be understood as a consequence of the null-geodesics really being deformations in space time and not "proper" deflections.

geodesics, it follows that the index of refraction is given by

$$n = \sqrt{\frac{1 - 2\Phi/c^2}{1 + 2\Phi/c^2}} = 1 - \frac{2\Phi}{c^2} + \mathcal{O}\left[\left(\frac{\Phi}{c^2}\right)^2\right]. \tag{2.2}$$

By invoking Fermat's principle (see appendix A) one finds the deflection angle $|\boldsymbol{\alpha}|$ of light passing outside a spherically symmetric mass M to be

$$|\boldsymbol{\alpha}| = \frac{4GM}{c^2 \xi} = 1''.75 \left(\frac{M}{M_\odot}\right)\left(\frac{\xi}{R_\odot}\right)^{-1} \tag{2.3}$$

where ξ is the impact parameter of the ray with respect to the mass (see figure 2.1), and G and c are the gravitational constant and the speed of light respectively. Note that this approximates the deflection to happen in one point, which is only reasonable provided that the deflection angle is small and the massive object is much smaller than the length of the trajectory. Objects that satisfy these criteria are referred to as *geometrically thin lenses*, and the approximation as the *thin lens approximation*.

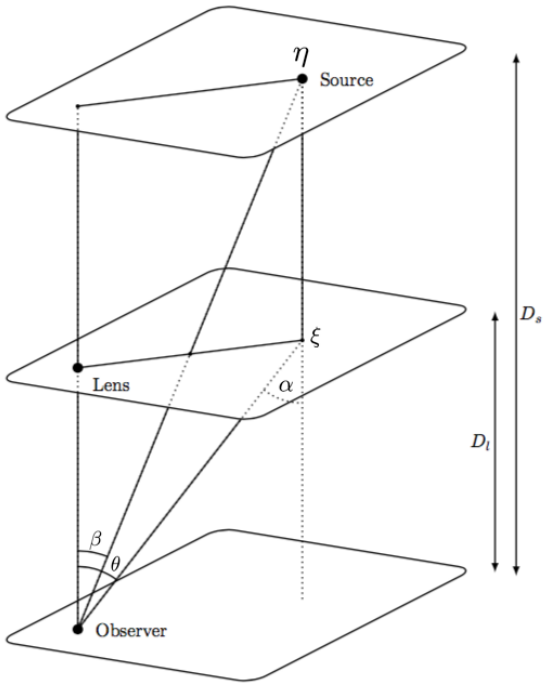

Figure 2.1: Setup for deflection of light by intervening massive objects assuming small deflection angles.

As demonstrated at the end of appendix A, equation (2.3) actually holds for masses that are axially symmetric with respect to the direction of propagation. For light passing through the object, one then has to substitute the mass M by the enclosed projected mass

$$M_p(\xi) \equiv \int_0^\xi 2\pi x dx \int_{-\infty}^{\infty} dz \rho(x, z) \tag{2.4}$$

where $\rho(x, z)$ is the mass density of the object and z is the direction of propagation. That the projected mass enters the expression should be understood as a consequence of the thin lens approximation which effectively treats the deflecting object as a flat sheet of matter.

2.1.2 The Lens Equation

Imagine a ray of light being gravitationally deflected by a geometrically thin massive object on its way from a point-like source to an observer. Denote the distance to

the lens and the source from the observer by D_l and D_s respectively. We refer to the planes orthogonal to the line of sight towards the lens with distances D_l and D_s as the *lens plane* and *source plane* respectively. From elementary geometry, it follows that

$$\boldsymbol{\eta} + D_{ls} \tan \boldsymbol{\alpha} = \frac{D_s}{D_l} \boldsymbol{\xi} \tag{2.5}$$

where D_{ls} is the distance between the lens and the source, $\boldsymbol{\eta}$ is the position of the source in the source plane, $\boldsymbol{\xi}$ is the distance of the deflection point in the lens plane and $\boldsymbol{\alpha}$ is the deflection angle of the ray. Here, $\tan \boldsymbol{\alpha}$ refers to the vector with components $\tan \alpha_i$, α_i being the components of $\boldsymbol{\alpha}$. Introducing the actual and apparent angular position of the source, $\boldsymbol{\beta}$ and $\boldsymbol{\theta}$, with respect to the observer, we may observe that for small deflection angles $\boldsymbol{\eta} = D_s \tan \boldsymbol{\beta} \simeq \boldsymbol{\beta}$ and $\boldsymbol{\xi} = D_l \tan \boldsymbol{\theta} \simeq D_l \boldsymbol{\theta}$. The result is the so-called *Lens equation*

$$\boldsymbol{\beta} = \boldsymbol{\theta} - \frac{D_{ls}}{D_s} \boldsymbol{\alpha} \,. \tag{2.6}$$

Although not generally true in curved space-times, we will in the following assume that $D_{ls} = D_s - D_l$.

For axially symmetric lenses, the deflection angle is given by

$$|\boldsymbol{\alpha}| = \frac{4GM_p(\xi)}{\xi} \tag{2.7}$$

where $\xi \equiv |\boldsymbol{\xi}|$. Note that in this case, by symmetry of the lens, the deflection angle must be directed radially in the lens plane. To see this more clearly, imagine a ray received at some non-zero $\boldsymbol{\theta}$. Although the axial symmetry of the geometry is broken, flips around the the line defined by $\boldsymbol{\theta}$ and the origin remains a symmetry. Therefore, if we trace the ray backwards, it cannot have been deflected in a direction other than that defined by $\boldsymbol{\theta}$, i.e. $\boldsymbol{\alpha} \propto \boldsymbol{\theta}$. If it did, it would violate the "flip-symmetry" of the scenario. It then follows from the lens equation (2.6) that $\boldsymbol{\alpha}$, $\boldsymbol{\theta}$ and $\boldsymbol{\beta}$ lies on the same radial line, meaning that it suffices to treat the lens equation as one-dimensional. Inserting for α then yields

$$\beta = \theta \left(1 - \frac{\theta_E^2(\theta)}{\theta^2}\right) \text{ for } \theta_E^2(\theta) \equiv \alpha\theta \frac{D_{ls}}{D_s} = \frac{4GM_p(\theta)}{c^2} \frac{D_{ls}}{D_l D_s}, \tag{2.8}$$

where $M_p(\theta)$ denotes the projected mass contained within a radius $D_l\theta$ in the lens plane, see equation (2.4). If the function $\theta_E(\theta)$ is independent of θ, then according to equation 2.8, θ_E is the apparent angular position of the source when its actual position is precisely behind the lens ($\beta = 0$). By the rotational symmetry of this scenario, the source will then appear to the observer as a ring of angular radius θ_E. We refer to the ring as the *Einstein ring* and its radius θ_E as the *Einstein radius*. More generally, at perfect alignment one must have $\theta = \theta_E(\theta)$, meaning that the Einstein radius is exactly a fixed point of θ_E. We will, however, refer the function

$\theta_E(\theta)$ as the Einstein radius. Note that we will sometimes use the same name for the *physical Einstein radius*

$$R_E(R) \equiv D_l \theta_E = \sqrt{\frac{4GM_p(R)}{c^2}\frac{D_l D_{ls}}{D_s}}, \tag{2.9}$$

which is the length in the lens plane needed to subtend an angle θ_E as a function of the distance R from the center of the lens to the deflection point of the considered ray. Curiously, the functional form of $\theta_E(\theta)$ opens the mathematical possibility for an exotic mass distribution to give rise to multiple Einstein rings.

For point-like lenses, the projected mass, and thus also the Einstein radius, is independent of θ. This makes the lens equation a quadratic equation, whose solution is

$$\frac{\theta}{\theta_E} = \frac{1}{2}\left(\frac{\beta}{\theta_E} \pm \sqrt{\left(\frac{\beta}{\theta_E}\right)^2 + 4}\right). \tag{2.10}$$

Hence, in the point-like case, the source will be visible to the observer in two different directions, whose angular separation is

$$\Delta\theta = \theta_E \sqrt{\left(\frac{\beta}{\theta_E}\right)^2 + 4}\,, \tag{2.11}$$

which is never smaller than twice the Einstein radius. In fact, the two images will always appear on each side of the Einstein ring – one inside and one outside*.

2.1.3 Apparent Magnification of the Source

Assuming absence of emission and absorption of photons along the way, it follows from Liouville's theorem that gravitational lensing conserves surface brightness. Therefore, any apparent light magnification of the source must be caused by a magnification of the angular size of the source. We can thus express the magnification μ as the ratio of deflected angular size per unit of un-deflected angular size. Although this can be easily computed in the case of an axially symmetric lens, let us use this as an opportunity to introduce some new terminology.

A gravitational lensing scenario can be thought of as a mapping $\boldsymbol{\theta} \mapsto \boldsymbol{\beta}$ from the apparent position $\boldsymbol{\theta}$ to the actual position $\boldsymbol{\beta}$ of the source. Since a ray of light received from a direction $\boldsymbol{\theta}$ must have taken a unique path from the source, the mapping $\boldsymbol{\theta} \mapsto \boldsymbol{\beta}$ must always be well defined †. The lens equation 2.6 then enables an easy way of studying the mapping $\boldsymbol{\theta} \to \boldsymbol{\beta}$, hereby referred to as the *lens mapping*,

*This is of course with the exception of $\beta = 0$, where the Einstein ring appears.

†Note that the inverse mapping $\boldsymbol{\beta} \mapsto \boldsymbol{\theta}$ is not generally well defined. The reason resides in the possibility that light emitted from the same source position $\boldsymbol{\beta}$, but in different directions, may hit the observer from different directions $\boldsymbol{\theta}$.

through calculation of its local linearization

$$\mathcal{A} \equiv \frac{\partial \boldsymbol{\beta}}{\partial \boldsymbol{\theta}} = \begin{pmatrix} 1-\kappa-\gamma_1 & -\gamma_2 \\ -\gamma_2 & 1-\kappa+\gamma_1 \end{pmatrix}. \tag{2.12}$$

Here we have introduced the *convergence* κ and the *shear* $\gamma = \gamma_1 + i\gamma_2$ which quantifies the isotropic and anisotropic deformation of the source respectively. This can be understood by confirming that its orthogonal eigenvectors have eigenvalues $1-\kappa\pm|\gamma|$. A sufficiently small spherical source will therefore appear to the observer as an ellipse of eccentricity $2|\gamma|/(1-\kappa+|\gamma|)$.

Note that if the determinant of the Jacobian (2.12) is nowhere vanishing, then the lensing scenario can form one image only. Since $\mathcal{A}$ must asymptotically equal the identity mapping then, by continuity, there will only be produced one image if, and only if, $\det\mathcal{A} > 0$ at all points. Conversely, $\det\mathcal{A} < 0$ in at least one point is a necessary and sufficient condition for multiple images to form. This, of course, only holds true for point-like sources being lensed by isolated and transparent lenses. In fact, under these assumptions any smooth mass distribution for which $M_p(\xi)/\xi$ remains bounded as $\xi \to \infty$ produces an odd number of images [61]. Note, however, that this is not valid for source positions that correspond to critical lines, where $\det\mathcal{A} = 0$.

In points where the inverse Jacobian matrix exists, its determinant quantifies the local change in apparent angular size compared to the actual angular size of the source. This, as we have seen, is exactly the magnification of an individual image. For this reason, the inverse linearized lens mapping is often referred to as the *magnification matrix* $\mathcal{M} \equiv \mathcal{A}^{-1}$. The magnification of an image of a point-like source produced by a geometrically thin, isolated and transparent lens is therefore given by

$$\mu = \frac{1}{\det\mathcal{A}} = \frac{1}{(1-\kappa)^2 - |\gamma|^2}. \tag{2.13}$$

Since, for an axially symmetric lens, the three vectors $\boldsymbol{\alpha}$, $\boldsymbol{\theta}$ and $\boldsymbol{\beta}$ lie on the same radial line, the magnification is more easily obtained by realizing that in this case the ratio of angular sizes equals the ratio of differential changes in the angular radii squared*. One then obtains

$$\mu = \left[\frac{\beta}{\theta}\frac{d\beta}{d\theta}\right]^{-1} = \left[\left(1-\frac{\theta_E^2}{\theta^2}\right)\left(1+\frac{\theta_E^2}{\theta^2}-2\frac{\theta_E}{\theta}\frac{d\theta_E}{d\theta}\right)\right]^{-1},$$

which agrees with the expression we would have found when determining (2.13) while assuming the validity of (2.8). Since

$$\frac{d\theta_E}{d\theta} = \frac{1}{2}\frac{\theta_E}{M_p}\frac{dM_p}{d\theta}$$

*Alternatively you can realize that infinitesimal angular sizes are given by $|\boldsymbol{\theta}\,d\phi \times d\boldsymbol{\theta}|$ and $|\boldsymbol{\beta}\,d\phi \times d\boldsymbol{\beta}|$

we can further write the magnification as

$$\mu = \left[\left(1 - \frac{\theta_E^2}{\theta^2}\right)\left(1 + \frac{\theta_E^2}{\theta^2} - \frac{\theta_E^2}{\theta}\frac{1}{M_p}\frac{dM_p}{d\theta}\right)\right]^{-1}. \tag{2.14}$$

For future convenience, let's also state this in terms of the physical Einstein radius $R_E \equiv D_l\theta_E$ and the *projected mass density*

$$\Sigma(\xi) \equiv \int \rho_{lens}\left(\sqrt{\xi^2 + z^2}\right) dz. \tag{2.15}$$

In terms of these variables, the magnification for an axially symmetric lens is given by

$$\mu = \left[\left(1 - \frac{R_E^2}{R^2}\right)\left(1 + \frac{R_E^2}{R^2} - 2\pi R_E^2\frac{\Sigma(R)}{M_p}\right)\right]^{-1}. \tag{2.16}$$

where $R = D_l\theta$. Sometimes, it can be convenient to define the *critical surface density* $\Sigma_{cr} \equiv M_p/(\pi R_E^2)$, to remind ourselves that this is independent of the image position R. From the above discussion, we see that if there are points such that $\Sigma(R) > \Sigma_{cr}$, then there are points for which $\mu(R)$ attains negative values. Therefore, if the projected mass density is larger than the critical mass density at some image positions, then some lens positions will constitute multiple images.

Note that for a point-like lens, for which $\Sigma(R) = 0$, the magnification takes the particularly simple form

$$\mu = \left[1 - \left(\frac{\theta_E}{\theta}\right)^4\right]^{-1}. \tag{2.17}$$

By virtue of equation 2.10, the magnification can be found more easily by direct calculation:

$$\mu_\pm = \frac{\theta}{\beta}\frac{d\theta}{d\beta} = \frac{1}{4}\left(1 \pm \frac{y}{\sqrt{y^2+4}}\right)\left(1 \pm \frac{1}{y}\sqrt{y^2+4}\right) = \frac{1}{2} \pm \frac{y^2+2}{2y\sqrt{y^2+4}} \tag{2.18}$$

where $y \equiv \beta/\theta_E$. This means that if $\beta = \theta_E$ then $\mu = 1/2 \pm 3\sqrt{5}/10$ which evaluates to $\mu_+ \approx 1.17$ for the larger image and $\mu_- \approx -0.17$ for the smaller image, where the negative sign signals that the smaller image will appear inverted. It follows that the total magnification for the two images combined is

$$\mu = |\mu_+| + |\mu_-| = \frac{y^2+2}{y\sqrt{y^2+4}} \tag{2.19}$$

which for $\beta = \theta_E$ gives $\mu \approx 1.34$.

Before moving on, there is one thing that should not remain uncommented: Our expression for the magnification diverges at the Einstein ring! This nonsensical result is caused by our non-physical assumption that the sources are point-like. Real sources will always subtend some, although typically vanishingly small, space angle in the sky. One should, therefore, average the magnification over all points $\boldsymbol{\beta}$ on the

source, which results in a finite expression for the magnification. A point-like source at position $\boldsymbol{\beta}$, whose images are at positions $\{\boldsymbol{\theta}_i\}$, will have a total magnification given by

$$\mu_{tot,0}(\boldsymbol{\beta}) = \sum_i |\mu(\boldsymbol{\theta}_i)|. \tag{2.20}$$

Treating an extended source as a collection of point-like sources, we can express its total magnification as

$$\mu_{tot} = \frac{\langle I(\boldsymbol{\beta})\mu_{tot,0}(\boldsymbol{\beta})\rangle}{\langle I(\boldsymbol{\beta})\rangle}, \tag{2.21}$$

where $I(\boldsymbol{\beta})$ is the surface brightness of the point $\boldsymbol{\beta}$ on the source, and the average is taken over the collection of points constituting the source.

2.2 Gravitational Microlensing

2.2.1 Types of Gravitational Lensing

It is customary to divide the realm of gravitational lensing into three main branches: *Strong Lensing*, *Weak Lensing* and *Microlensing*. A strong lensing scenario is one that forms multiple images, which typically have an observable separation. This means that quantities such as the flux ratio and angular separation of individual images are accessible. For image separations to be resolvable, the lenses need to be both distant and heavy. Therefore, strong lensing is the study of galaxy- and cluster-sized lenses at cosmological distances.

In weak gravitational lensing, scenarios that are too weak to form multiple images are studied. This often amounts to estimating the mass density through determination of the deformation field (see equation (2.12)). In absence of knowledge about the true shape of the sources, weak lensing is typically combined with a statistical machinery to determine the local correlation of source ellipticity as due to an intermediate, deflecting density field. For further information on weak lensing see e.g. [60], or the famous weak lensing result from the Bullet Cluster (1E 0657-558) [62].

Lastly, gravitational microlensing is, like strong lensing, the study of lensing scenarios constituting multiple images*. The difference between the two is that microlensing is concerned with lenses that are too small for the images to be resolved. This, however, leaves only one measurable quantity, namely the apparent source brightness. Unfortunately, without knowledge of the unlensed flux, this value seems to be of little use. The key insight is that the observer, lens, and source will generally have a relative velocity that makes the lensing geometry time dependent. For small and nearby sources, these timescales will be accessible.

Consider, for example, a point-like lens passing the line of sight towards a solar source with an angular impact parameter β_0 and velocity $v_\perp$ perpendicular to the

* Conceptually, gravitational microlensing could also probe weak lensing scenarios, but this would require magnification sensitivities far beyond those of today.

line of sight. The total magnification would then be given by equation (2.19) where

$$y(t) = \sqrt{\left(\frac{\beta_0}{\theta_E}\right)^2 + \left(\frac{v_\perp (t - t_0)}{D_l \theta_E}\right)^2}. \tag{2.22}$$

This means that,

$$\Delta t_E \equiv \frac{D_l \theta_E}{v_\perp} \tag{2.23}$$

defines a timescale for the microlensing event. If one considers a source in the Large Magellanic Cloud (LMC) with roughly $D_s \simeq 50\mathrm{kpc}$, then the time-scale for a solar mass lens passing at a distance of $2\mathrm{kpc}$ with perpendicular velocity $v_\perp = 220\mathrm{km/s}$, which is roughly the rotational velocity of the solar system around the center of the galaxy, then $\Delta t_E \simeq 9$ weeks. If instead, the lens had Earth-mass $M \simeq 10^{-6} M_\odot$, then the time scale would be roughly one and a half day.

Gravitational lensing is, however, not the only cause of change in apparent source brightness. In addition to absorption and eclipsing effects, many stars exhibit intrinsic brightness variations. Therefore, filtering out all the impostors is a complicated process. Leaving this aside, there are also some theoretical problems related to the information contained in a microlensing event. At best, one could obtain a fit of the expected magnification (2.22) which would determine the time t_0 of the event, the impact parameter $y_0 = \beta_0/\theta_E$ and its duration Δt_E. Since the time t_0 is only a convention, and the impact parameter y_0 depends on the random position of the lens, the only quantity that contains physical information is the time scale Δt_E. Sadly, the information contained in Δt_E is a degenerate combination of the lens mass M, the perpendicular velocity $v_\perp$, and the distance both to the source D_s and the lens D_l as seen from the observer. It is often possible to determine D_s by other means, which leaves D_l, $v_\perp$ and M as free variables. Although it is, in principle, possible to lift the degeneracy further by utilizing perturbing effects such as finite source size or the wobbling of the line of sight as the earth rotates around the sun – known as the *parallax effect* – one would still be left with a severe degeneracy between the lens mass M and the perpendicular lens velocity $v_\perp$.

Regardless of the degeneracy issue, one can obtain stringent bounds on the abundance of microlenses based solely on the number of events detected.

2.2.2 The History and Status of Gravitational Lensing

The idea of gravity as deflector of light can be traced back to Newton himself where he in *Query I* of Opticks 1704 [63] asks "*Do not Bodies act upon Light at a distance, and by their action bend its rays, and is not this action strongest at the least distance?*". After the completion of the theory of General relativity in 1915, Einstein proposed a deflection angle twice that of the Newtonian prediction [64] (see equation (2.3)). The total eclipse of May 29, 1919, allowed measurement of the astrometric deviation of a star close to the sun [65]. The result, which favored

Einstein's theory [66], also marked the first observation of a gravitational lensing phenomenon.

In the coming years, the theoretical possibility for multiple images to form due to gravitational lensing was discussed (see Chwolson 1924 [67] and Einstein 1936 [68]) [60]. Observing this phenomenon, however, was regarded as extremely unlikely. That view was not shared by Fritz Zwicky, who in 1937 claimed that extragalactic nebulae, now called galaxies, offered a much greater chance of observing lens effects [69]. The only problem was that there were no known objects that could act as sources at these distances. Then, in 1963, the first quasi-stellar object (quasar) was discovered [70], which was both luminous and distant enough to be lensed by other galaxies. The first observation would, however, have to wait until 1979 when Walsh et al. published the discovery of two quasars (QSO 0957+561), separated by only six seconds of arc, which were measured to lie at the same distance and have identical spectra [71, 72]. Already the next year, a triple-imaged quasar (PG1115+080) was discovered [73]. A few years later giant luminous arcs were discovered and identified as heavily distorted images of distant galaxies [74, 75]. Then, finally, in 1988 the first observation of an Einstein ring was reported found in the radio source MG 1131+0456 [76]. Up to this point, only strong gravitational lensing phenomena had been observed. The idea that individual stars might cause flux variations in the images of QSO 0957+561 was, however, much discussed during the eighties [77–79]. The first claimed detection of such a microlensing effect was, however, found in the quadruple-imaged quasar QSO 2237+0305 by Mike Irvin (1989)[80, 81].

During the early nineties, multiple dedicated telescopes were built with the intent of addressing a question posed by Bohdan Paczyński in his 1986 article [60, 82]. Paczyński had realized that if the dark matter in the galactic halo is made of compact objects more massive than the moon ($\sim 10^{-8}\mathrm{M}_{\odot}$), then the probability for any star to be microlensed at a given time must be about 10^{-6}. If one were to monitor the brightness of a few million stars in the Magellanic Clouds, one would therefore be able to determine the amount of dark matter that is in the form of massive astrophysical compact halo objects (MACHOs).

First, three different collaborations were formed: OGLE (Optical Gravitational Lensing Experiment), EROS (Expérience pour la Recherche d'Objets Sombres) and MACHO. In 1993 the first detection of galactic microlensing events was announced by Aubourg et al. (EROS) [83] and Alcock et al. (MACHO) [84], both maintaining the view that MACHOs remains a viable candidate. At the end of the MACHO survey around year 2000, having monitored 11.7 million stars in the Large Magellanic Cloud (LMC) for 5.7 years, they reported to have found a total of $13-17$ candidate microlensing events [85] – about one order of magnitude fewer than Paczyński's prediction. This was in agreement with the preliminary results of EROS for the Small Magellanic Cloud (SMC) at the time [86]. On the other hand, the OGLE survey, which monitored stars in the galactic bulge, had reported an optical depth of about $(3.3 \pm 1.2) \times 10^{-6}$ already in 1994 [87]. Since this was larger than expected, the matter was investigated further. In the end (2003) a survey by EROS-2 suggested $(0.94 \pm 0.29) \times 10^{-6}$[88] – a number that fits well with models assuming no MACHO

population. When the dust settled, the microlensing surveys had strongly disfavored the MACHO Dark Matter model for masses from $10^{-7}M_\odot$ to about $10M_\odot$. To probe even lower masses, however, the Magellanic clouds was of little use. The reason is that when one considers smaller masses, the angular size scale of microlensing – the Einstein radius – decreases. For masses lower than $10^{-7}M_\odot$, the Einstein radius starts to become smaller than the source size, which leads to the magnification peak being heavily suppressed. The solution to this problem had already been proposed in 1992 by Arlin Crotts [89]. Crotts suggested searching for microlensing of stars in the Andromeda Galaxy (M31) which, being about 15 times more distant than the Magellanic clouds, would make it possible to probe masses at least down to about $10^{-10}M_\odot$. In addition, the tilted disc of M31 would make it possible to statistically distinguish between lenses in M31 and the Milky Way. This did, however, come with some serious problems attached. One would, for instance, need to increase the time resolution even though the sources, being more distant, were much fainter than for LMC. A more severe problem was that of angular resolution. Since no telescope would be able to resolve individual stars in M31, each pixel could only monitor the combined flux of from multiple stars. This would lead to a much larger background flux which meant larger magnification were required in order to observe a microlensing event. This, of course, also means that it is possible to monitor many more sources at the same time. The method proposed by Crotts is frequently referred to by the somewhat unfortunate name of *pixel microlensing* or *pixel-lensing*. Although multiple pixel-lensing surveys such as AGAPE (Andromeda Galaxy Amplified Pixels Experiment), MEGA (Microlensing Exploration of the Galaxy and Andromeda) and WeCAPP (Wendelstein Calar Alto Pixellensing Project) were conducted early on, we will, for the sake of brevity, only discuss one the most recent ones here. The Subaru Hyper Suprime-Cam (HSC) monitored about 10^8 stars throughout the entire M31 galaxy for 7 hours with a 2 minute sampling rate [90]. This resulted in strong limits on the population of dark compact objects with masses between $10^{-14}M_\odot$ and $10^{-6}M_\odot$. The details of these bounds will be discussed extensively throughout the rest of this thesis.

2.2.3 The Unlikeliness of a Microlensing Event

This section aims to introduce some vocabulary for microlensing while discussing what exactly a *microlensing event* is and how we can estimate its unlikeliness. When discussing the latter, we will follow Paczyński [82], Nemiroff [91] and Griest [92] closely.

Consider a point-like lens drifting between an observer and a single point-like source. Let the lens be in the origin and denote the angular position of the source by $\boldsymbol{\beta}$. The smaller the value of $|\boldsymbol{\beta}|$, the larger the total magnification $\mu(\boldsymbol{\beta})$ becomes. At some point, the magnification will become large enough for the observer to distinguish it from the noise of the detector. This magnification, which we will refer to as the *threshold magnification* μ_T, defines an upper bound on $|\boldsymbol{\beta}|$ needed for the microlensing effect to be observable. We will denote the physical length of this upper

bound as it appears in the lens plane by ℓ_T. For a given lens, each distance D_l will fix ℓ_T and hence define a tube around the line of sight towards the source, called the *microlensing tube*. For this reason, we will refer to ℓ_T as the *tube radius*. The microlensing tube will play a vital role in what follows as its interior defines the lens positions that would constitute observable microlensing effects. Note that the tube radius will typically be given by some constant u_T times the Einstein radius R_E, where u_T depends on μ_T only.

Consider a lens that has tube radius ℓ_T and a constant velocity $\boldsymbol{v}$ with respect to the rest frame of the microlensing tube. Denote the magnitude of the component of $\boldsymbol{v}$ perpendicular to the line of sight by $v_\perp$ and its angle with respect to center-line of the tube by θ. The observable microlensing effect, referred to as the *microlensing event*, will then last for a time

$$t_e = \frac{2\ell_T}{v_\perp}\cos\theta. \tag{2.24}$$

We will call this time the *event duration*, not to be confused with the *time of diametrical crossing* $\hat{t} \equiv 2\ell_T/v_\perp$. In fact, when averaged over uniformly distributed impact parameters $b = \ell_T \sin\theta$ on the interval $[-\ell_T, \ell_T]$ we have

$$\langle t_e \rangle = \frac{\pi}{4}\langle \hat{t} \rangle . \tag{2.25}$$

If one would be able to resolve the images in a microlensing event, its geometry would look something like figure 2.2. The top figure, which is computed with a ray-tracing algorithm assuming the validity of the lens equation (2.6), shows snapshots of a spherical source being lensed by a pointlike object. The red circles display the contour of the actual positions of the source, while the black areas depict the images corresponding to each source position. Note how the Einstein radius (dotted black line) defines the scale of the event, and that no image ever crosses the line. The lower image depicts the magnification (black solid line) together with what the magnification would have been if the source was point-like (black dotted line). This former is found by computing the deformed black areas in units of the area of the undeflected source, while the latter is the magnification in equation (2.19). The red line marks the threshold magnification which we have set to $\mu_T = 1.34$. For point-like lenses, this corresponds to setting the tube radius (red dotted lines) equal to the Einstein radius.

It is customary to state the likelihood for microlensing via determination of the number of lenses inside a single microlensing tube – a quantity referred to as the *microlensing optical depth* τ. Assuming constant number density n of lenses and a factoring $\ell_T = u_T R_E$ of the tube radius, the optical depth is given by

$$\tau = \frac{4GM}{c^2} D_s^2 \frac{\pi u_T^2}{6} n. \tag{2.26}$$

If all dark matter were to be the form of point-like objects of solar mass, then, assuming a constant dark matter density of $\rho = Mn \simeq 0.008 M_\odot/pc^3$ all the way to

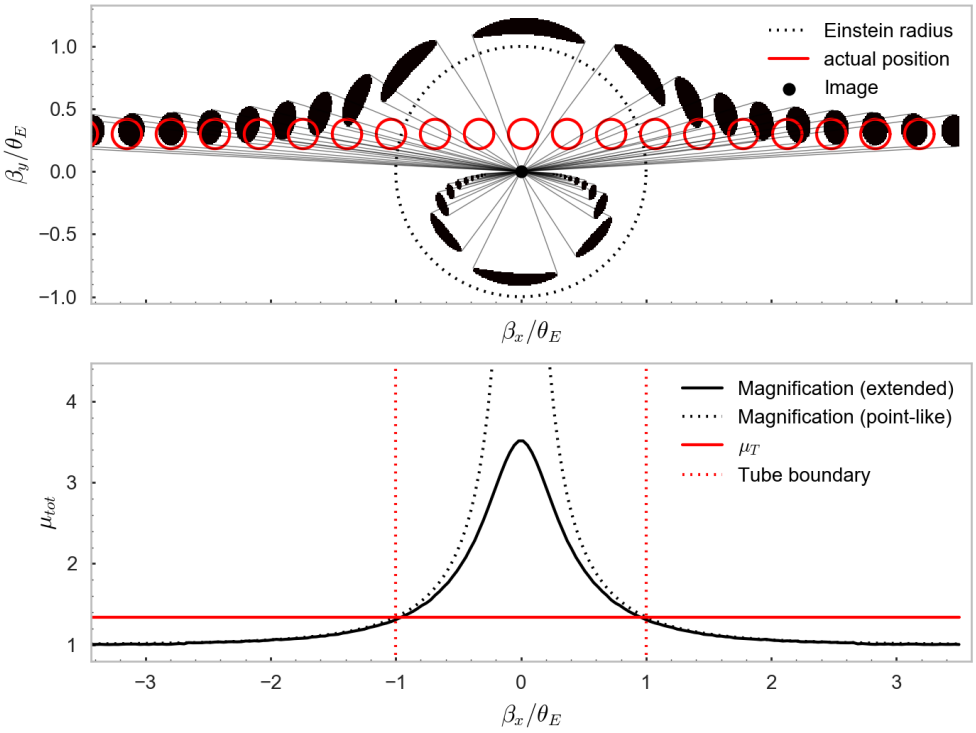

Figure 2.2: The geometry of a microlensing event by a point-like lens is shown in the top figure. The red circle displays the actual position and size of the source, while the black patches correspond to how they appear to the observer. Thin gray lines are drawn to illustrate show which images correspond to each other. Note that there are always two images, one inside the Einstein ring (dotted black line) and one outside. The bottom figure displays the magnification for the event both for a point-like source (dotted black) and for an extended source (black line). This is compared to the threshold magnification value $\mu_T = 1.34$ (red line) defining the boundary of the microlensing tube (dotted red).

the large Magellanic cloud ($D_s \simeq 50\text{kpc}$) one would obtain roughly $\tau = 2 \times 10^{-6}$. This means that one would have to look at about half a million stars in the LMC in order to expect to witness one that is microlensed.

Generally, the optical depth associated with a spherically symmetric thin lens is given by

$$\tau \equiv \int \pi \ell_T^2 n(D_l) dD_l. \tag{2.27}$$

Assuming $\ell_T = u_T R_E$, we can write this as

$$\tau = \frac{4G}{c^2} \pi f D_s^2 u_T^2 \int_0^1 \rho(x) x(1-x) dx \tag{2.28}$$

where $x \equiv D_l/D_s$, f is the fraction of dark matter in the form of point-like objects and $\rho(x)$ is the dark matter density along the line of sight.

2.2.4 The Number of Expected Microlensing Events

For a microlensing event to be detected, one needs to witness the whole, or at least a large portion, of its passage across the microlensing tube. More relevant than the optical depth is, therefore, the microlensing *event rate*, which quantifies the flux of lenses through the microlensing tube. In the following, we derive an expression for the expected differential event rate per event duration. We start by following the procedure of Griest [92] and consider the differential flux of lenses through the lensing tube of a single point-like source

$$d\Gamma = (\boldsymbol{v}_\perp \cdot d\boldsymbol{S}) n(\boldsymbol{r}) f(\boldsymbol{v}) \frac{dN}{dM} d^3v dM \tag{2.29}$$

where $\boldsymbol{v}_\perp$ is the velocity of the lens perpendicular to the line of sight, $d\boldsymbol{S}$ is a surface element of the microlensing tube pointing normally out of the tube, $n(\boldsymbol{r})$ is the number density of lenses in position $\boldsymbol{r}$, $f(\boldsymbol{v})$ is the velocity distribution of the lenses, $\frac{dN}{dM}$ is the mass distribution for the lenses and d^3v is an infinitesimal volume element in velocity space. For simplicity, we will assume a monochromatic mass distribution, meaning that $dN/dM = \delta(M - m)$. This allows us to write

$$d\Gamma = v_\perp \cos\theta n(\boldsymbol{r}) f(\boldsymbol{v}) d^3v dS \tag{2.30}$$

where θ is the angle between $\boldsymbol{v}_\perp$ and $d\boldsymbol{S}$. In the host halo regions, we may assume an isotropic Maxwellian velocity distribution[90]:

$$f(\boldsymbol{v}) = \frac{1}{\left(\sqrt{\pi} v_c\right)^3} \exp\left[-\frac{(\boldsymbol{v} - \boldsymbol{v}_t)^2}{v_c^2}\right] \tag{2.31}$$

where $\boldsymbol{v}_t = (1-x)\boldsymbol{v}_{\perp,O} + x\boldsymbol{v}_{\perp,S}$ is the transversal velocity of the lensing tube, $\boldsymbol{v}_{\perp,O}$ and $\boldsymbol{v}_{\perp,S}$ being the transversal velocity of the observer and the source respectively and $x \equiv D_l/D_s$. The width of the distribution is chosen to be the local circular

velocity of the sun $v_c \approx 220\text{km/s}$ [92, 93]*. When considering halos bound to other galaxies than the Milky Way (MW), v_c generally takes a different value. We will later need the velocity curve for the Andromeda galaxy (M31), which flattens at about 226km/s[94]. Since setting $v_c = 220\text{km/s}$ for both MW and M31 allows us to estimate the combined, differential event rate $d\Gamma$ for both galaxies in a single calculation, this will be done throughout the thesis.

Now, choose polar coordinates (ℓ,α) in the lensing plane such that $dS = \ell_T\, d\alpha d D_l$ and cylindrical coordinates $(v_\perp, \theta, v_\parallel)$ in velocity space so that $d^3v = v_\perp\, d\theta dv_\perp dv_\parallel$. Since $\mathbf{v}_\parallel$ is orthogonal to $\boldsymbol{v}_t$, the $v_\parallel$-dependence can be easily integrated out, leaving us with

$$d\Gamma = \frac{n(\mathbf{r})v_\perp^2 \cos\theta \ell_T}{\sqrt{\pi}v_c^2} \exp\left[-\frac{(\boldsymbol{v}_\perp - \boldsymbol{v}_t)^2}{v_c^2}\right] d\theta dv_\perp dv_\parallel d\alpha d D_l. \tag{2.32}$$

In the end, Griest reaches an expression for the event rate per event duration given by

$$\frac{d\Gamma}{dt_e} = n(\mathbf{r})\frac{16\ell_T^4}{t_e^4 v_c^2} y^{\frac{3}{2}}(1-y)^{-\frac{1}{2}} e^{-\frac{v_t^2}{v_c^2} - Ay} I_0(B\sqrt{y}) dy d D_l, \tag{2.33}$$

where

$$A = \left(\frac{2\ell_T}{v_c t_e}\right)^2 \text{ and } B = 2\sqrt{A}\frac{v_t}{v_c}. \tag{2.34}$$

Here $y = \cos^2\theta$ and I_0 is the modified Bessel function of the first kind.

Since this expression is rather inconvenient, we deviate from Griest and follow the method appearing in appendix A of Alcock et al [95]. The idea is to instead use the duration of diametrical crossing

$$\hat{t} \equiv \frac{2\ell_T}{v_\perp} \tag{2.35}$$

whose relation to the actual event duration t_e is given by $t_e = \hat{t}\cos\theta$. Substituting $dv_\perp = 2\ell_T/\hat{t}^2 d\hat{t}$ and integrating out the θ-dependence, leaves the expression

$$\frac{d\Gamma}{d\hat{t}} = n(\mathbf{r})\frac{32\ell_T^4}{\hat{t}^4 v_c^2} e^{-\frac{v_t^2}{v_c^2}} e^{-Q} I_0\left(2\sqrt{Q}\frac{v_t}{v_c}\right) d D_l \text{ for } Q \equiv \left(\frac{2\ell_T}{\hat{t}v_c}\right)^2 \tag{2.36}$$

which, in the case of negligible tube velocities ($v_t \simeq 0$) simplifies to

$$\frac{d\Gamma}{d\hat{t}} = n(\mathbf{r})\frac{32\ell_T^4}{\hat{t}^4 v_c^2} e^{-Q} d D_l, \tag{2.37}$$

knowing that $I_0(x) \simeq 1$ for $x \ll 1$. Finally, assuming the number density of lenses to be proportional to the mass density ρ_{host} of the host galaxy we find

$$n(\mathbf{r}) = f\frac{\rho_{host}(\mathbf{r})}{M} \tag{2.38}$$

*Using v_c as a constant assumes a flattened velocity curve throughout. An alternative would be to set $v_c^2 = GM_{host}(< r)/r$.

where f is the fraction of the total amount dark matter contained in such lens objects and M is the mass of the lens. Note that by allowing a mass dependence for f, we can, in principle, handle extended mass distributions. Note also that this rather crucial assumption that the number density is proportional to the mass density amounts to saying that the Dark Matter objects are not clustered. There have been recent claims that the microlensing limits on Primordial Black Hole Dark Matter (PBH DM) has been overestimated because of this [47].

Although the time scale accessible to the telescope is determined by t_e, and not $\hat{t}$, we will treat them on equal footing. This can be justified, at least up to a factor of order unity, by equation (2.25). Assuming the detection efficiency ε of the telescope depends on the event duration $\hat{t}$ only, the predicted number of events can be expressed by

$$N_{exp} = E \int d\hat{t} \frac{d\Gamma}{d\hat{t}} \varepsilon(\hat{t}), \tag{2.39}$$

where E is the number of stars monitored times the amount of monitoring time.

2.3 Constraints on Point-like Objects

2.3.1 Bound Objects between us and M31

This section seeks to reproduce the exclusion curves for the fraction of the galactic halo that can be in the form of point-like objects using the results from the microlensing survey by Hyper-Suprime-Cam (HSC) Subaru Telescope towards the Andromeda galaxy (M31). We will refer to the point-like objects as PBHs, knowing that other, sufficiently compact, objects would be subject to the same constraints. The method closely mimics the one used by Fairbairn et al. [1] and, as they do, we will compare the final results to those obtained by Niikura et al. [90].

To start, we approximate the density profiles of the host galaxies as NFW profiles (see eq (1.48)) with parameters $R_s = 21.5\text{kpc}$ and $\rho_s = 4.88 \times 10^6 M_\odot/\text{kpc}^3$ for the Milky Way (MW), and $R_s = 25.0\text{kpc}$ and $\rho_s = 4.96 \times 10^6 M_\odot/\text{kpc}^3$ for M31 [96]. We use, as Fairbairn et al. [1], galactic coordinates $(l, b) = (121.2°, -21.6°)$ for M31 setting $D_s = 770\text{kpc}$. In terms of these coordinates the distance to the MW center of mass from the line of sight can be written

$$r_{MW}(x) = \sqrt{R_\oplus - 2D_s x R_\oplus \cos(l)\cos(b) + x^2 D_s^2} \tag{2.40}$$

for $x \equiv D_l/D_s$. Since the HSC survey monitored stars in the galactic disc, bulge and halo regions [90], we approximate the distance to the center of M31 from the line of sight as

$$r_{M31}(x) = D_s(1 - x). \tag{2.41}$$

Considering lenses bound to both M31 and MW thus amounts to using the parametrized host mass density

$$\rho_{host}(x) \equiv \rho_{MW}(r_{MW}(x)) + \rho_{M31}(r_{M31}(x)). \tag{2.42}$$

The main goal of this section will therefore be to evaluate the following integral

$$N_{exp} = fE \int_0^\infty d\hat{t} \int_0^1 dx \frac{D_s \rho_{host}(x)}{M} \frac{32 u_T^4 R_E(x)^4}{\hat{t}^4 v_c^2} \exp\left[-\left(\frac{2u_T R_E(x)}{\hat{t} v_c}\right)^2\right] \varepsilon(\hat{t}) \quad (2.43)$$

where we have factored the tube radius $\ell_T(x) \equiv u_T R_E(x)$. We will set $u_T = 1$ which corresponds to a magnification threshold of $\mu_T \simeq 1.34$. Note that equation (2.43) only holds for point-like lenses assumed to have a monochromatic mass-spectrum and be bound to one of the host galaxies with Maxwellian velocity distribution normalized to flattened rotation curves at $220 km/s$ [92–94].

First, let us examine the telescope-independent part of the integrand

$$\frac{d\Gamma}{d\hat{t}dx} = \frac{D_s \rho_{host}(x)}{M} \frac{32 R_E(x)^4}{\hat{t}^4 v_c^2} \exp\left[-\left(\frac{2u_T R_E(x)}{\hat{t} v_c}\right)^2\right] \quad (2.44)$$

where, for simplicity, we have set $f = 1$. This can be interpreted as the number of microlensing events produced by a single star whose duration of diametrical crossing is in the interval $[\hat{t}, \hat{t} + d\hat{t}]$ and distance to lens is in the interval $[x, x + dx]$ measured in units of the source distance.

The functional form of equation (2.44) for the lens mass $M = 10^{-8} M_\odot$ is shown in figure 2.3. The white region at low $\hat{t}$ marks event rates smaller than $10^{-5}/yr^2$ which are artificially removed to make the contributing domain more visible. The plot suggests that we should take care while integrating due to the narrow peaks at the boundary of the x domain. Physically, this means that we expect most of the microlensing events to be due to lenses either very close to the solar system ($x \simeq 0$) or very close to the source ($x \simeq 1$). In fact, looking at how equation (2.44) scales, we find

$$\frac{d\Gamma}{d\hat{t}dx} \sim \frac{1}{M}\left[\frac{Mx(1-x)}{\hat{t}^2}\right]^2 \exp\left(-\text{const} \times \left[\frac{Mx(1-x)}{\hat{t}^2}\right]\right). \quad (2.45)$$

This means that for a fixed duration of diametrical crossing, lenses at the boundary will become increasingly important when one considers larger lens masses. Similarly, for a fixed lens distance x, the time of diametrical crossing $\hat{t}$ must increase roughly as the square root of the lens mass. Therefore, for some mass larger than the one depicted in figure 2.3, the contribution from all lenses that are not on the boundary of x will be exponentially suppressed due to a duration of diametrical crossing that is larger than the monitoring time. From figure 2.3 we can estimate at which mass this happens. The lower $\hat{t}$ suppression becomes important at about one order of magnitude less than the maximal value of $\hat{t}$, which means that for masses two orders of magnitude larger than the one depicted, namely $M \simeq 10^{-6} M_\odot$ the integral will be completely dominated by the narrowing boundary contribution. Note also that for sufficiently low masses the number of expected events should scale roughly as the lens mass.

To take the peaky domain dependence into account, an importance sampling, Monte-Carlo (MC) integration scheme is constructed. To pay special attention to

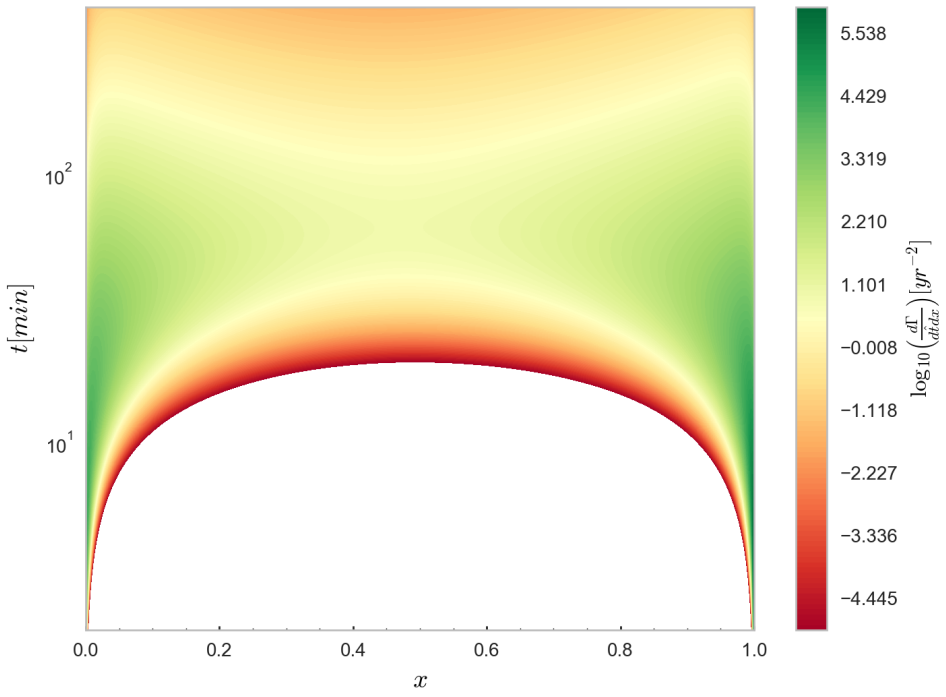

Figure 2.3: The logarithm of the differential event rate $\mathrm{d}\Gamma$ per time of diametrical crossing $\hat{\mathrm{t}}$ per distance $\mathrm{x} \equiv \mathrm{D_l}/\mathrm{D_s}$ (see equation (2.44)), is shown for a survey of M31 assuming all Dark Matter to be in the form of point-like objects with mass $\mathrm{M} = 10^{-8}\mathrm{M}_\odot$. The white region contains all event rates smaller than the chosen value $10^{-5}/\mathrm{yr}^2$.

the boundaries of x we sample from the probability distribution

$$P(x) = \frac{1}{\pi\sqrt{x(1-x)}} \tag{2.46}$$

which is chosen to mimic the x dependence of the inverse Einstein radius. A set of points distributed according to (2.46) are thus found by mapping uniformly distributed values on the interval $[0, 1]$ with the inverse cumulative density function

$$\text{icdf}(x) = \sin^2\left(\frac{\pi x}{2}\right). \tag{2.47}$$

Sampling from this distribution should, however, be done with caution as the probability mass is shifted so much to the boundaries that some samples may be rounded to $x = 1$, for which the integrand is undefined. This is solved naively by resampling until no round-off enters, thus possibly imposing a sampling bias.

As the domain does not exhibit as narrow peaks along $\hat{t}$, it should suffice to sample from a simple exponential distribution. To do this, a scale parameter t_{scale} needs to be chosen. Since $\hat{t} \equiv 2u_T R_E/v_\perp$ we choose

$$t_{scale} = 50\frac{\sqrt{\frac{GM}{c^2}D_s}}{220\text{km/s}}, \tag{2.48}$$

to avoid an x dependence, where the factor 50 is found by trial and error.

Let us now estimate the HSC telescope efficiency $\varepsilon(\hat{t})$, which defines to what degree the telescope is sensitive to different event durations. As pointed out by Niikura et al. [90], the functional form of the efficiency will generally depend on the magnitude of the source. To avoid a too involved analysis we pretend, as Fairbairn et al. [1], $\hat{t}$ is the event duration and estimate the efficiency of the HSC survey as a step function with value 0.5 whenever $2\text{min} \leqslant \hat{t} \leqslant 7\text{hr}$. For comparison we also perform the calculation with an efficiency found by taking the green curve in fig 19. of Niikura et al [90], which corresponds to a star with absolute magnitude of 24mag, and performing a least-squares fit with a double sigmoid function

$$\varepsilon_{fit}(t) = \frac{C}{1+e^{-A(t-t_1)}} - \frac{C}{1+e^{-B(t-t_2)}}. \tag{2.49}$$

The resulting fit, as seen in figure 2.4, agrees well for parameters $A = 106 \pm 11\%$, $t_1 = 0.0575 \pm 2\%$, $B = 1.83 \pm 11\%$, $t_2 = 4.11 \pm 2\%$ and $C = 0.598 \pm 1\%$ when t is measured in units of hours.

Now, all that remains is to estimate the efficiency E, which is the amount of monitoring time for all the sources combined. Since HSC monitored roughly 10^8 stars for a period of seven hours, we choose E to be $10^8 \times 7\text{hr} \simeq 79909\text{yr}$. Assuming all dark matter is in the form of PBHs ($f = 1$) the resulting prediction for the number of expected microlensing events is as shown in figure 2.5.

As can be anticipated from our discussion of figure 2.3, the number of expected microlensing events peaks at a lens mass around $10^{-10}M_\odot$, which corresponds

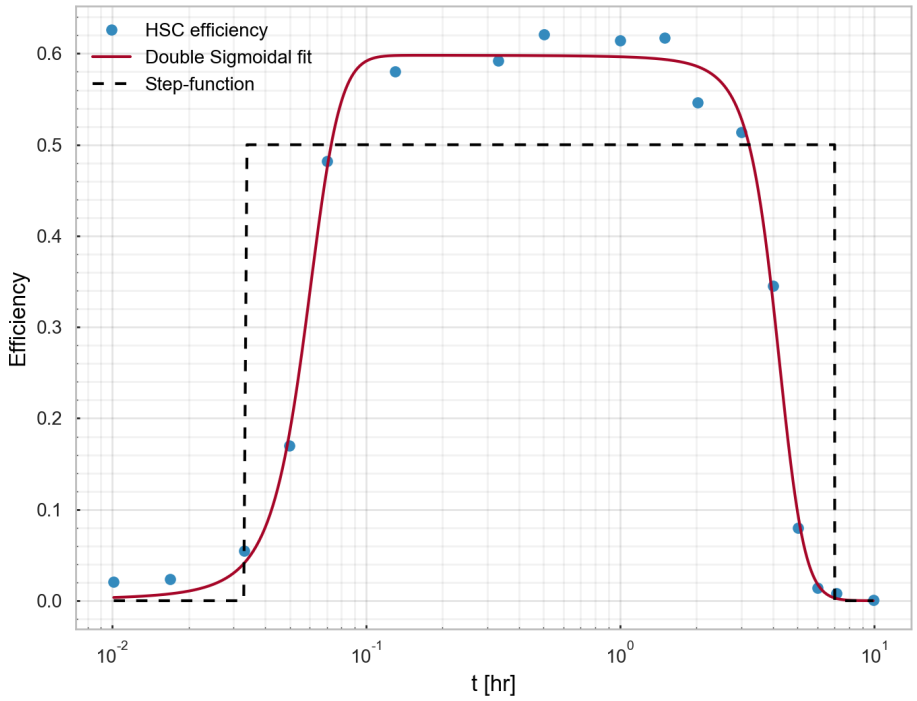

Figure 2.4: The event duration efficiency (green curve in fig 19. of Niikura et al [90] v1) compared to the step-function approximation (dashed), being constantly 0.5 for $2\mathtt{min} \leqslant \mathtt{t} \leqslant 7\mathtt{hr}$. The solid red line shows the best fit of a double sigmoidal function (2.49), having parameters $\mathtt{A} = 106 \pm 11\%$, $\mathtt{t}_1 = 0.0575 \pm 2\%$, $\mathtt{B} = 1.83 \pm 11\%$, $\mathtt{t}_2 = 4.11 \pm 2\%$ and $\mathtt{C} = 0.598 \pm 1\%$ for $\mathtt{t}$ measured in hours.

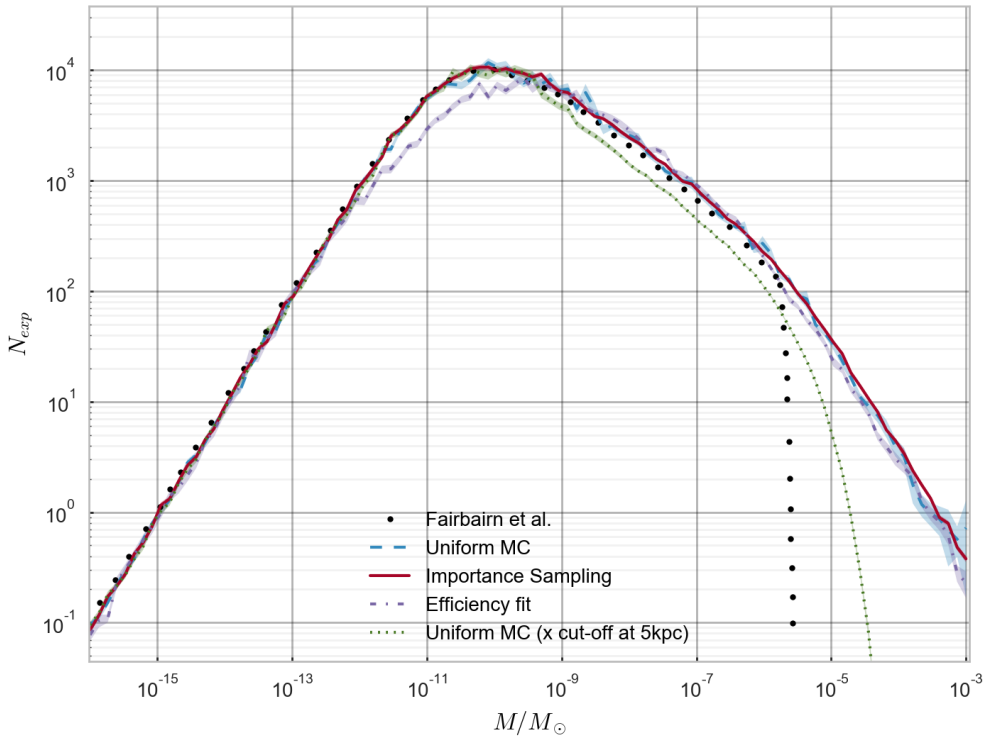

Figure 2.5: The number of expected microlensing events from PBHs bound to the galactic halo for a survey of M31 using equation 2.43. The results are compared to the those of Fairbairn et al. [1] (black dots). The computation is performed using four different techniques: A uniform MC integrator on a step-function efficiency (dashed blue), an importance sampling (IS) MC scheme on a step-function efficiency (solid red), an IS MC using the double sigmoidal efficiency fit in figure 2.4 (dot-dash purple) and a uniform MC integrator which disregards all lenses closer than 5kpc from either the source or the solar system. All integrators use 10^5 sampling points and have an estimated MC error of roughly $0.5 - 10\%$ depending on the method and lens mass.

roughly to reducing the duration of diametrical crossing by one order of magnitude. The three methods yield consistent results, with the exception of the method using a double sigmoidal efficiency (dot-dash purple) predicting slightly fewer events for the "ideal" lens mass. They are also in good agreement with the result of Fairbairn et al, except for the absence of the cut-off slightly above $10^{-6}M_{\odot}$.

In our treatment, the absence of a cut-off at high masses can be understood by realizing that even though microlensing at intermediate distances will become increasingly suppressed as the lens mass increases, there will always be lenses close enough to the boundary for the suppression to be ineffective. Since, in addition, the host density favors lenses at the boundary, this means no sharp cut-off should appear. Discarding all lenses that are too close to either the source or the solar system could reproduce such a cut-off, but for it to happen for masses around $10^{-6}M_{\odot}$ would mean that all lenses closer than about $5\mathrm{kpc}$ should be disregarded. This is way too large for it to make physical sense, and even if it were, its functional form would not fit that of Fairbairn et al. For comparison, this curve is included in figure 2.3 (dotted green). After communication with the authors, it has turned out that the cut-off in [1] is indeed a numerical error on their side, arising from the narrowing of peaks in the x dependence of equation (2.44) as the lens mass M increases.

Next, we treat the number of expected events N_{exp} as a function of the lens mass M and the fraction of dark matter $f \equiv \Omega_{PBH}/\Omega_{DM}$ that is in the form of PBHs. For each mass, we then compare our prediction $N_{exp}(M, f)$ with the number N_{obs} of microlensing events observed by the HSC survey. Assuming microlensing events are Poisson distributed, we have

$$P(N_{obs}|N_{exp}) = \frac{N_{exp}^{N_{obs}}}{N_{obs}!} e^{-N_{exp}} \tag{2.50}$$

whose 95% confidence limits (CL) are found by

$$\sum_{N=0}^{N_{obs}} P(N|N_{exp}) \leqslant 0.05\,. \tag{2.51}$$

The HSC survey found only one candidate event that passed all the tests [90]. Taking the optimist view that this is an actual microlensing event by a PBH, we are left with the 95% CL upper limit of $N_{exp} = 4.74$. Using that $N_{exp}(M, f) = fN_{exp}(M, 1)$ the 95% CL upper limit on the amount of dark matter in the form of PBHs is therefore given by

$$f(M) \leqslant \frac{4.74}{N_{exp}(M, 1)}. \tag{2.52}$$

The computed bounds are shown in comparison to those of Fairbairn et al and Niikura et al. in figure 2.6.

The results agree very well, with the exception of the Niikura et al bound being slightly stronger for small lens masses and slightly weaker for large masses. This effect is thought to arise from a collection of simplifications from our side. For example, Niikura et al integrates over a proper source-magnitude dependent efficiency

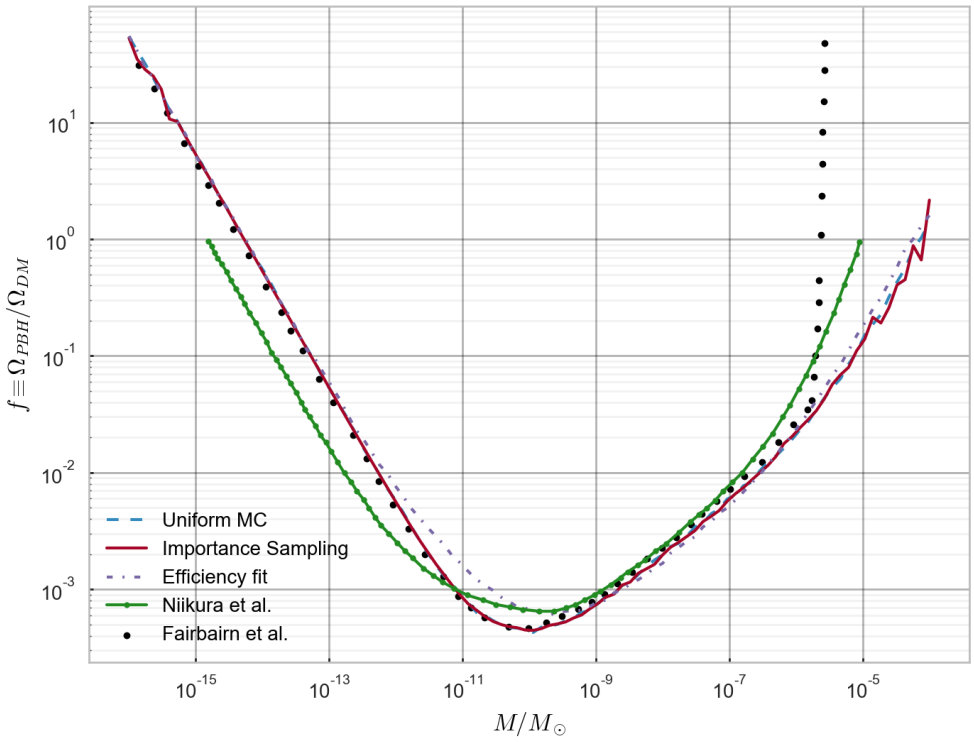

Figure 2.6: The 95% C.L upper bound on the fraction f of dark matter in the form of PBHs for the optimistic view that the microlensing candidate seen by HSC is a PBH. The three methods using a uniform MC integrator (blue dashed), more involved importance sampling integration method (red solid) and the importance sampling method with the fitted double sigmoidal function for efficiency (purple dash-dot) is compared with the results of Fairbairn et al. (black dots) and Niikura et al (green dotted line). All integrators use 10^6 MC points.

and uses the actual event duration t_e instead of the time of diametrical crossing $\hat{t}$. The effect may also be affected by our assumption that the rotational velocity v_c is flattened throughout the line of sight. Niikura et al computes N_{exp} for lenses in MW and M31 separately and instead estimates v_c by

$$v_c(r) = \sqrt{\frac{GM_{host}(< r)}{r}}, \tag{2.53}$$

where they use $M_{host}(< r)$ as the enclosed dark matter host mass inside r. This means that they predict lower velocities for intermediate lenses, leading to a larger number of expected events where short event durations start to suppress the integrand. Since too short event durations occur for low masses, we expect Niikura et al to claim better exclusion limits in this regime.

To avoid having to calculate N_{exp} for lenses in MW and M31 separately, we will stick with our method throughout the thesis, knowing that it only slightly alters the exclusion limits.

Chapter 3

Microlensing of Halo Objects

We now turn to what is the main focus of this thesis, namely the prospects for microlensing extended NFW-profiled lenses.

3.1 Lensing by NFW-profiled Objects

In their paper, Fairbairn et al (2017) [1] claim to constrain the number of axion miniclusters, modeled as NFW profiled halos, using results from microlensing surveys such as HSC. This suggests that NFW profiled lenses should, at least for some parameter choices, make observable microlensing effects. In this section, we will try to determine for which NFW parameters the microlensing effect is observable.

3.1.1 The Profile and its Projected Mass

To determine the lensing properties of a NFW-profiled object, we must first determine the functional form of the projected mass density $\Sigma(\xi)$ and the enclosed projected mass $M_p(\xi)$. Assuming the object to follow a NFW profile (see equation (1.48)) without an outer cut-off actually makes the integral

$$\Sigma(\xi) = \int_{-\infty}^{\infty} \rho_{NFW}\left(\sqrt{\xi^2 + z^2}\right) dz \tag{3.1}$$

exactly solvable. Factoring out the parameters by defining $\Sigma(R) \equiv 2\pi\rho_s R_s \tilde{\Sigma}(R/R_s)$, the result can be stated as

$$\tilde{\Sigma} = \begin{cases} \frac{2}{x^2-1}\left[1 - \frac{2}{\sqrt{1-x^2}}\operatorname{arctanh}\sqrt{\frac{1-x}{1+x}}\right] & \text{for } x < 1 \\ \frac{2}{3} & \text{for } x = 1 \\ \frac{2}{x^2-1}\left[1 - \frac{2}{\sqrt{x^2-1}}\arctan\sqrt{\frac{x-1}{x+1}}\right] & \text{for } x > 1 \end{cases} \tag{3.2}$$

in agreement with Wright and Brainerd [97]. Since the mass contained inside a sphere of radius R, which is given by

$$M_{enc}(R) = 4\pi\rho_s R_s^3 f\left(\frac{R}{R_s}\right) \text{ for } f(x) \equiv \ln(x+1) - \frac{x}{x+1}, \tag{3.3}$$

is logarithmically divergent, it is unphysical to consider NFW-profiled objects without an outer cut-off. We therefore introduce a cut-off radius R_{max} and define $x_M \equiv R_{max}/R_s$. Since dark matter halos are described well by an NFW profile only out to the virial radius, it is natural to choose $R_{max} = R_{vir}$. Assuming $\rho \propto 1/r^3$ at $x \gtrsim x_M$ then allows us to estimate by how much we have overestimated the outer projected mass density, namely

$$\delta\tilde{\Sigma} = 2\int_{x_M}^{\infty} \rho dz = \frac{2}{x^2}\left[1 - \sqrt{1 - \left(\frac{x}{x_M}\right)^2}\right]. \tag{3.4}$$

Taking this into account, we are left with the expression

$$\tilde{\Sigma}(x) = \begin{cases} \frac{2}{x^2-1}\left[1 - \frac{2}{\sqrt{1-x^2}}\operatorname{arctanh}\sqrt{\frac{1-x}{1+x}}\right] & \text{for } x < 1 \\ \frac{2}{3} & \text{for } x = 1 \\ \frac{2}{x^2-1}\left[1 - \frac{2}{\sqrt{x^2-1}}\arctan\sqrt{\frac{x-1}{x+1}}\right] - \delta\tilde{\Sigma}(x) & \text{for } x > 1 \\ 0 & \text{for } x > x_M \end{cases} \tag{3.5}$$

for the projected mass density. The enclosed projected mass can then be found in a similar fashion. First, we introduce the dimensionless enclosed projected mass by $M_p(R) \equiv \rho_s R_s^3 \tilde{M}_p(R/R_s)$ and integrate the projected mass density over a circular sheet of radius $R \equiv xR_s$ centered at the origin. The resulting expression is

$$\tilde{M}_p(x) = \begin{cases} 2\pi\left[2\ln\frac{x}{2} + \frac{4}{\sqrt{1-x^2}}\operatorname{arctanh}\sqrt{\frac{1-x}{1+x}}\right] & \text{for } x < 1 \\ 2\pi\left[2\ln\frac{x}{2} + \frac{4}{\sqrt{x^2-1}}\arctan\sqrt{\frac{x-1}{x+1}} - \frac{1}{2}\frac{x^2}{x_M^2} - \frac{1}{16}\frac{x^4}{x_M^4}\right] & \text{for } x_M \geqslant x \geqslant 1 \\ \frac{M_{tot}}{\rho_s R_s^3} & \text{for } x > x_M \end{cases} \tag{3.6}$$

Knowing the functional form of $M_p(R)$ means we have an analytic expression for the Einstein radius using equation (2.9). We therefore have all we need to perform the lens mapping.

Figure 3.1 displays the images corresponding to four different source-lens separations when deflected by an NFW object. To obtain these images, a ray-tracing algorithm has been implemented to compute the inverse lens mapping. The NFW lens is chosen to have a very high concentration $C = 2 \times 10^7$ and low virial mass $M_{vir} = 10^{-6} M_\odot$. While the high concentration is chosen to better visualize the deformation properties, the low lens mass is chosen to make the Einstein ring (red solid and gray dotted) comparable to the size of the source, which is taken to be sun-sized. The source is taken to be in M31 ($D_s = 770\text{kpc}$) and the lens position in MW with $D_l = 0.01 D_s$. Note that for sufficiently large source-lens separations (top left figure), there will only be one image. This is very different from point-like lenses, where there will always be two images.

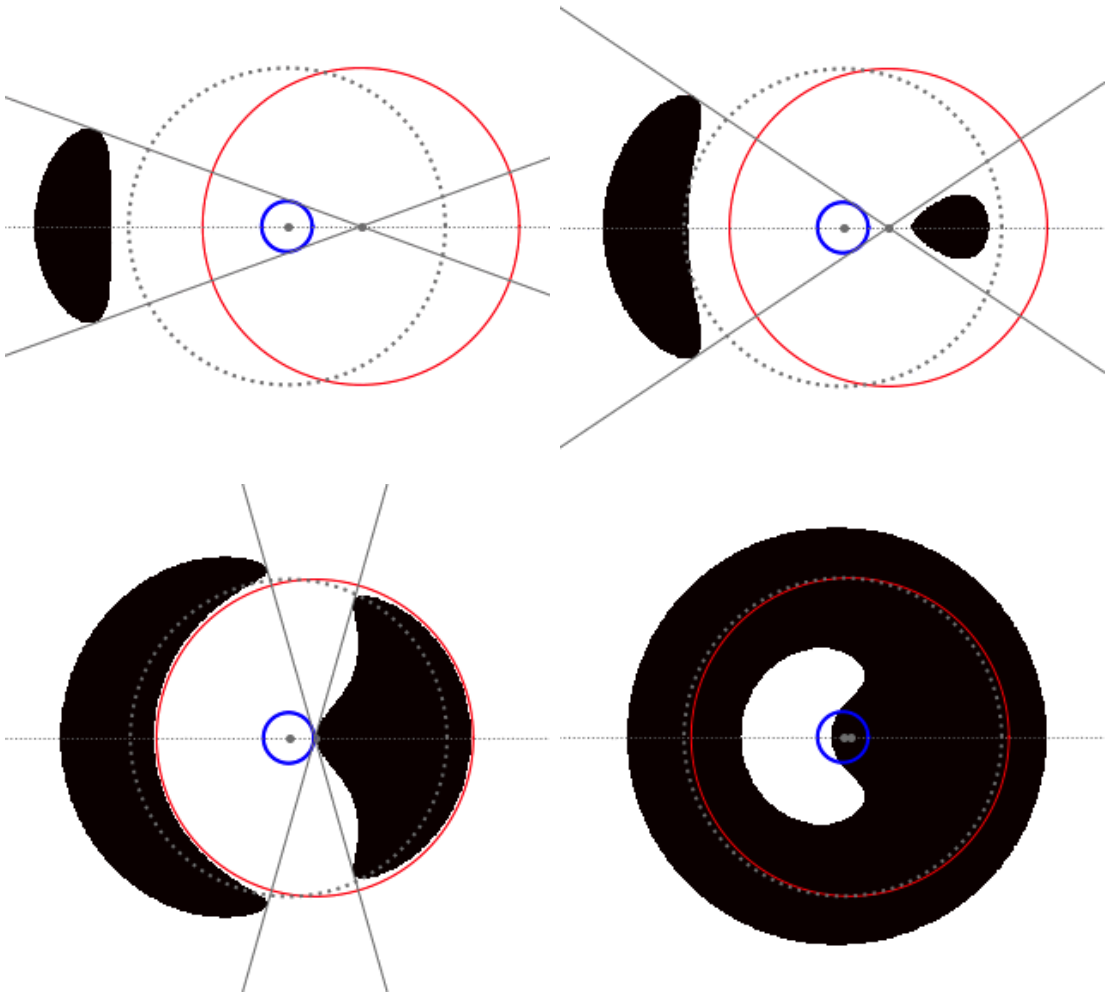

Figure 3.1: The geometry of the image constituted by an NFW-profiled object deflecting light from an extended source. The blue circle indicates the actual position and size of the source, while the black area shows how it would appear to the observer. The gray radial lines demonstrate the angular extent of the image as seen from the lens, located at the intersection of the lines. The red and gray dotted circles mark the Einstein ring (θ_E^*) centered at the lens and source respectively.

3.1.2 Estimating the Tube Radius

When predicting the number of expected microlensing events by NFW profiled objects, we may recycle most of the formalism introduced in the previous chapter. In fact, the only thing that prevents us from simply calculating N_{exp} as it appears in (2.43) is that we do not know the functional form of the tube radius ℓ_T. The central problem is therefore to determine the tube radius ℓ_T as a function of the lens distance $x \equiv D_l/D_s$, the virial mass M_{vir} and the concentration C.

For a given magnification threshold μ_T, the tube radius ℓ_T is exactly the distance $D_l\beta_T$ for which the total magnification $\mu_{tot}(\beta_T)$ is μ_T. It should, therefore, at least in principle, be easy to find ℓ_T: Find an expression for the total magnification $\mu_{tot}(\beta)$ and demand $\mu_{tot}(\beta_T) = \mu_T$. The problem is that the total magnification $\mu_{tot}(\beta)$ is given as a sum of the absolute value of the magnification of each image

$$\mu_{tot}(\beta) = \sum_{\theta \in \|\mathbf{F}^{-1}(\{\beta\})\|} |\mu(D_l\theta)|, \tag{3.7}$$

where $\mathbf{F} : \boldsymbol{\theta} \to \boldsymbol{\beta}$ is the lens mapping and $\mu(R)$ is defined in equation (2.16). Sadly, determining the fiber $\mathbf{F}^{-1}(\{\beta\})$ of a source position β is both analytically nontrivial and computationally expensive.

A brute force method for computing the total magnification would be to utilize a ray-tracing algorithm. By virtue of the lens mapping $\mathbf{F}$, a set grid of points $\{\boldsymbol{\theta}\}$ in the lens plane can be mapped to their corresponding source positions in the source plane by $\mathbf{F}(\{\boldsymbol{\theta}\}) = \{\boldsymbol{\beta}\}$. For a certain angular source position $\boldsymbol{\beta}_0$ with angular radius $\delta\beta_s$, the corresponding image positions can be found using

$$\text{Images}(\beta_0, \delta\beta_s) = \left\{\boldsymbol{\theta} \middle| \|\mathbf{F}(\boldsymbol{\theta}) - \boldsymbol{\beta}_0\| \leqslant \delta\beta_s\right\}. \tag{3.8}$$

This means that the total magnification is given by

$$\mu_{tot}(\beta_0) = \frac{\int_{\text{Images}(\beta_0, \delta\beta_s)} d^2\theta}{\pi(\delta\beta_s)^2}. \tag{3.9}$$

This will, however, become increasingly difficult to evaluate when the source size $\delta\beta_s$ becomes much smaller than the Einstein radius.

Another method, which we will refer to as *semianalytic*, would be to numerically find all solutions $\boldsymbol{\theta}$ of $\mathbf{F}(\boldsymbol{\theta}) = \boldsymbol{\beta}_0$ and then compute (3.9) analytically.

In figure 3.2 the total magnification for an NFW deflector with virial mass $M_{vir} = 10^{-6}M_\odot$, concentration $C = 2 \times 10^7$ and distance $x = 0.01$ with respect to M31 ($D_s = 770\text{kpc}$) is portrayed. The four ray-tracing estimates (gradient blue solid lines) are computed with 1400×1400 gridpoints assuming source sizes $R_\odot$, $R_\odot/2$, $R_\odot/4$ and $R_\odot/8$ respectively. We also compute the total magnification due to a point-like object with similar Einstein radius θ_E^* and the magnification one would have obtained if the image-positions were the same as for a point-like lens. The latter has, for obvious reasons, been dubbed *semiaccurate*. Note that the semianalytic method for estimating the total magnification agrees very well with the ray-tracing

results. Therefore the numerical estimate of the tube radius is computed using this method. It should not be taken as a surprise that the NFW magnification is larger than the magnification of a point-like lens whose Einstein radius equals the Einstein fixed point radius θ_E^* of the NFW halo. After all, slightly outside θ_E^* one expects $\theta_E(\theta) > \theta_E^*$ since $\theta_E(\theta)$ scales as the square root of the enclosed projected mass. A point-like lens of the same mass as the NFW halo, however, will generally have much larger magnifications except, of course, in cases where θ_E^* is larger than the angular extent of the halo ($\theta_E^* \gtrsim R_{vir}/D_l$). In that case, the halo would be indistinguishable from a PBH.

Such devoted estimates of the total magnification are needed to determine the tube radius accurately. Sadly, the estimation methods outlined above are not easily generalized to point-like sources and a wide range of halo parameters. Moreover, due to the sensitivity of the lensing integral, we will need a lot of integration points in the x-domain. Since the tube radius is dependent on x, we need a much faster estimate of the tube radius. For this reason, we follow Fairbairn et al and pretend an NFW deflector has two images and that their images have the same positions and magnification ratio as for point-like objects. This means that for a threshold magnification of $\mu_T = 1.34$, we need only to determine the maximal θ for which $\mu(D_l\theta) = 1.17$. Let us denote this value for $D_l\theta$ by R_T. Since, in this case, one has $\beta = \theta_E$ for a point-like lens, it follows from equation (2.10) that $\beta = \theta/1.618$. That is, we estimate the tube radius ℓ_T by

$$\ell_T \simeq \max\left\{ x D_s \frac{\theta}{1.618} \middle| \mu(D_l\theta) = 1.17 \right\} . \tag{3.10}$$

This estimate appears as a black dashed line in figure 3.2. Although it does not perfectly match the more precise semianalytic estimate, it suffices as a rough estimate. In fact, we will later see that the halo parameters $M_{vir} = 10^{-6} M_\odot$ and $C = 2 \times 10^7$ portrayed in figure 3.2 correspond to a limiting case and that the other halos for which estimating a tube radius makes sense, are even better approximated as point-like.

To reduce the x-dependence of ℓ_T we introduce the factorization $R_T \equiv \mathcal{R} R_E(M_{vir})$. Unfortunately, $R_E(M_{vir})$ does not absorb all the x-dependence of ℓ_T. Especially for low-concentration halos, $\mathcal{R}$ will exhibit some x-dependence at the boundaries. This x-dependence of $\mathcal{R}$ is shown in figure 3.3 for solar-mass lenses with 100 log-spaced concentrations between 10^4 and 10^{10}. As the rounded box-shape of the $\mathcal{R}$ will become clearer later, we postpone the discussion and simply note that as C decreases, the span of the non-zero values of $\mathcal{R}$ becomes more narrow in the x-domain.

Since the tube radius will only enter in the lens integral, and since $\mathcal{R}$ mainly exhibits variations close to the boundaries of x, we will solve for the tube radius on a set of lens positions x more densely packed close to the boundary. To achieve this, we use the inverse cumulative density function in equation (2.47) to map a linearly spaced set of x-values. The resulting distribution is shown as black dots in figure 3.3. By linear interpolation over this set, we obtain the estimated values for

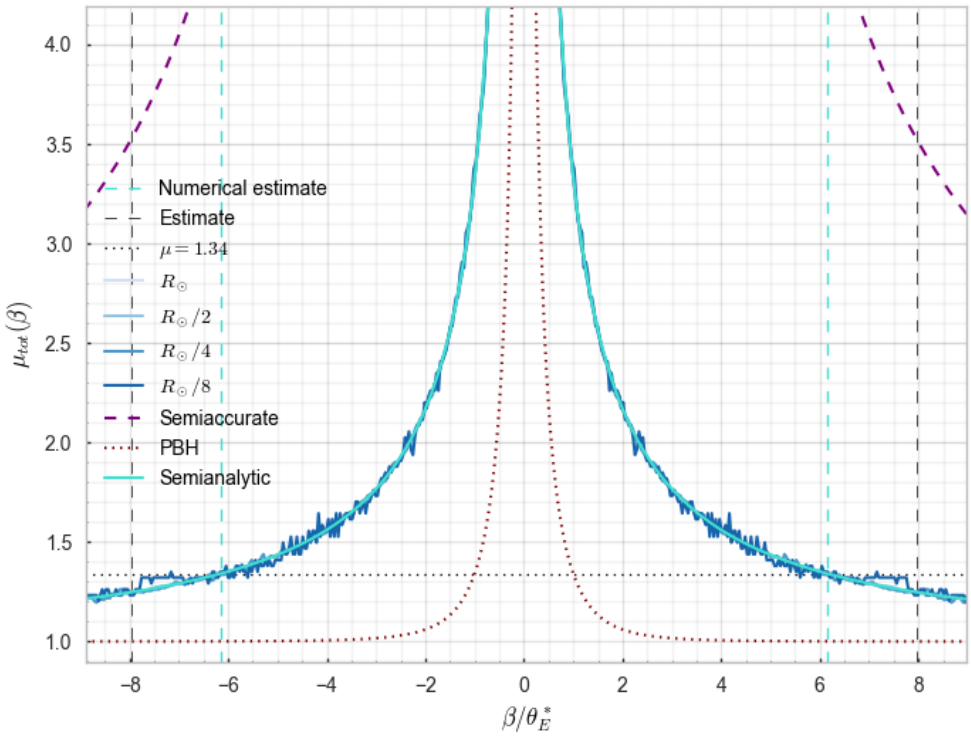

Figure 3.2: Various estimates of the total magnification due to an NFW-profiled deflector. The gradient blue solid lines are obtained by ray-tracing with a finite source-size of $R_\odot$, $R_\odot/2$, $R_\odot/4$ and $R_\odot/8$ respectively. The dashed purple line assumes a point-like lens to obtain the image positions and uses the analytic expression (2.16) for the magnification, while the cyan line computes the image positions numerically and is, therefore, the most exact estimate of the magnification due to a point-like source. These curves are compared to the magnification from a point-like lens whose Einstein radius agrees with the NFW Einstein radius fixed point θ_E^* (red dotted line). The black dotted line marks the magnification threshold $\mu_T = 1.34$, the cyan dashed line displays the numerically estimated solution for $\mu_{tot}(\beta) = 1.34$ while the black dashed lines are the estimate used throughout this thesis.

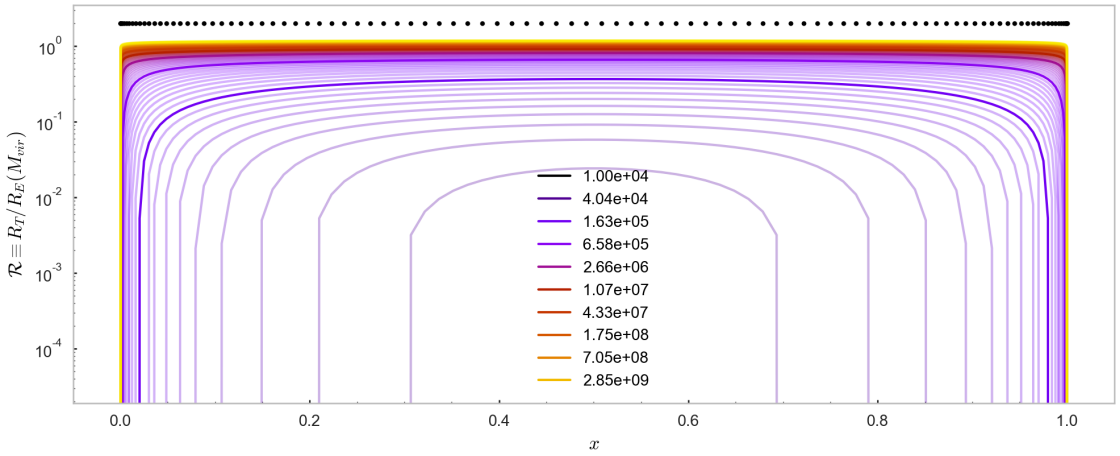

Figure 3.3: The estimated value for the distance R_T, from the center of mass of the lens, the outer image has when the image is magnified by a factor 1.17. This, which is taken to be an estimate of the tube radius, is displayed in units of $R_E(M_{vir})$ as a function of $x \equiv D_l/D_s$. The different lines correspond to 100 different NFW lenses with log-spaced concentrations between 10^4 and 10^{10} where every tenth is colored strongly. All the lenses have the same mass, $M_{vir} = M_\odot$, and the source is taken to be in M31.

the tube radius ℓ_T as a function of x which should replace $u_T R_E(x)$ in the lensing integral (2.43).

3.2 Can WIMPy Halos be Microlensed?

3.2.1 Which Halos are Observable?

To study which halos are in principle observable, we first imagine an idealized version of the HSC survey which monitors for infinitely long with an infinitely short sampling rate. In other words, we set $\varepsilon(\hat{t}) = 1$ for all $\hat{t}$. Although unphysical, this will serve as the maximal number of events one can expect from a survey of M31 whose threshold magnification is $\mu_T = 1.34$.

Since a general, NFW profiled lens is determined by its virial mass M_{vir} and concentration C, we consider a grid of points in the (C, M_{vir})-plane. We can then think of each point therein as the scenario that all dark matter is in the form of halos with NFW parameters C, M_{vir} that is gravitationally bound to one of the galaxies. Computing the tube radius ℓ_T and evaluating the lens integral

$$\frac{N_{exp}}{E} = \int_0^\infty d\hat{t} \int_0^1 dx \frac{D_s \rho_{host}(x)}{M} \frac{32\ell_T^4}{\hat{t}^4 v_c^2} \exp\left[-\left(\frac{2\ell_T}{\hat{t} v_c}\right)^2\right] \tag{3.11}$$

then yields the number of expected events per monitored star per year of monitoring time. The result of this computation on a log-spaced 200×200 grid $(C, M_{vir}) \in$

$[1, 10^{10}] \times [10^{-9}M_\odot, 10^{12}M_\odot]$ is shown in figure 3.4, which hereby will be referred to as the *prospect plane*. In the figure a gray band has been added, signaling the concentration-mass relation for WIMPy halos as stated by Sánchez-Conde et al [49]. The width of the band corresponds to one standard deviation.

Now, each point in the colored region corresponds to a certain number of expected microlensing events per monitored star per year of monitoring time. For example, the yellow region refers to the halos that would produce observable microlensing events for about one in a million stars during a year of monitoring time. In other words, one would have to monitor about one million stars over a year in order to expect one single microlensing event due to these halos. On the other hand, the dark green area corresponds to halos that, for each monitored star, are expected to produce one observable microlensing event per year. This is, of course, a way too optimistic number for realistic telescopes. Since the green area corresponds to very small halos, their event durations will typically be much smaller than the exposure time of the telescope, meaning that most events will not be seen. Likewise, the red area, which corresponds to one event per year per hundred billion stars, should also be treated as an unrealistic limiting case as these halos are of about the same mass as the host galaxies.

The points where there is no color (white area) corresponds to the case where no value for the tube radius ℓ_T was found. Therefore, the white area corresponds to the halos whose passage in front of any star would not be observable by a telescope of magnification threshold $\mu_T = 1.34$. That is, the prospect plane seems to suggest that even for an ideal efficiency, a microlensing survey of M31 with magnification threshold $\mu_T = 1.34$ would never be able to constrain the number of galactic WIMPy halos bound to the galaxy. WIMPy halos are simply not compact enough! The rest of this chapter will, therefore, be devoted to understanding this result, and discussing the hope of resolving this issue by, for example, considering different source-positions and magnification thresholds. Before embarking on that discussion, however, let us point out that the prospect plane does not suggest that all Dark Matter halos evade such microlensing constraints. For instance, the Axion miniclusters discussed by Fairbairn et al [1] are expected to have a much larger concentration than the WIMP halos, and therefore be subject to constraints.

3.2.2 The Reasonable Behavior of the Prospect Plane

The prospect plane as depicted in figure 3.4 exhibits two obvious features. For sufficiently large concentrations the number of expected events becomes approximately independent of concentration, and for any given virial mass M_{vir}, there seems to be a minimal concentration C needed for microlensing events to be detectable.

That concentration becomes irrelevant at sufficiently high values should not be taken as a surprise. After all, high concentration means more matter accumulates in the center of the halo, making it gradually better described as a point-like lens. Actually, since the microlensing effect is only sensitive to the projected mass density $\Sigma(R)$ and the enclosed projected mass $M_p(R)$, we can, by virtue of equations (3.5)

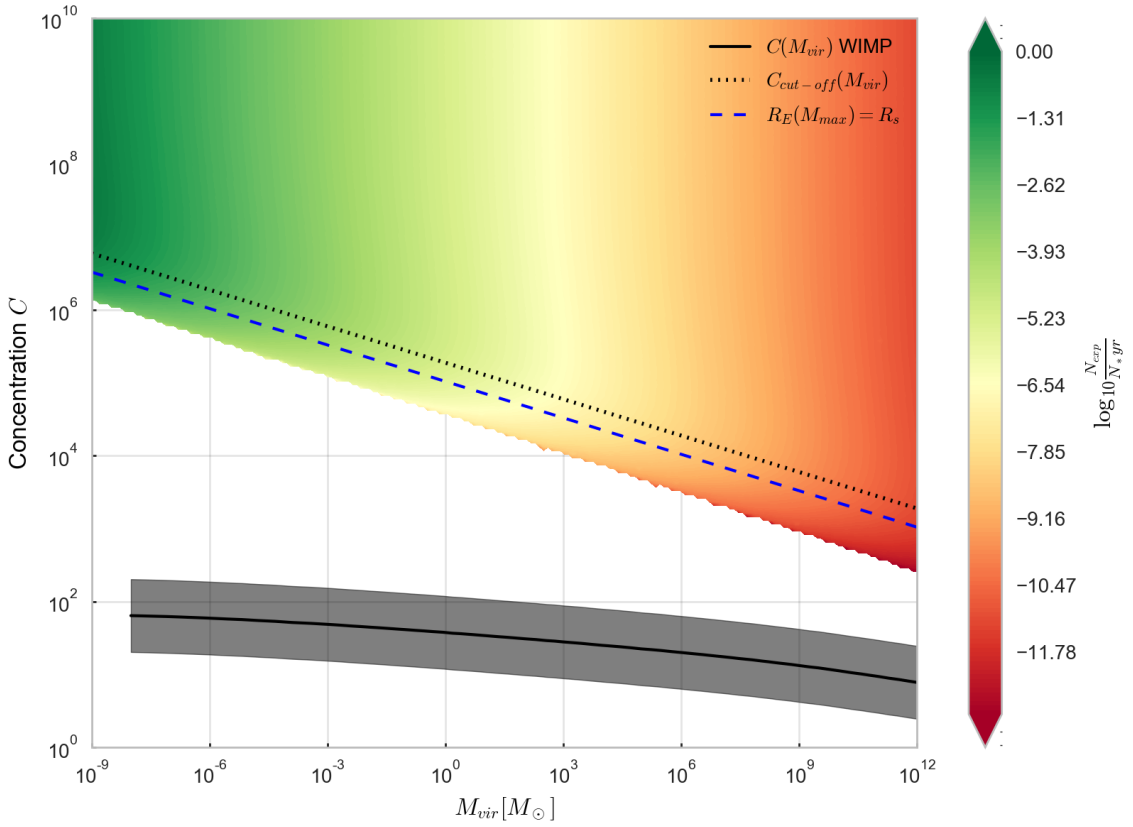

Figure 3.4: The number $\mathsf{N_{exp}}$ of expected microlensing events per star monitored per year of monitoring time estimated for a 200×200 grid of log-spaced NFW lens profile parameters $(\mathsf{C}, \mathsf{M_{vir}}) \in [1, 10^{10}] \times [10^{-9}\mathsf{M}_\odot, 10^{12}\mathsf{M}_\odot]$. The number of expected events $\mathsf{N_{exp}}$ is found by solving equation (3.11) with the approach discussed in previous sections. Added to the figure is also a black line, corresponding to the concentration-mass relation for WIMPy halos as stated by Sánchez-Conde et al [49], and its $\pm 1\sigma$ band. Two estimates, $\mathsf{R_E}(\mathsf{M_{vir}}) \simeq \mathsf{R_s}$ and $\mathsf{C_{cut-off}}$, of the cut-off scale, is shown as a blue dashed line and a black dotted line respectively.

and (3.6), compute this limit. Since the scale radius R_s is inversely proportional to the concentration C, large C means small R_s. First, let us consider the projected mass density $\Sigma(R) \equiv 2\pi\rho_s R_s \tilde{\Sigma}(R/R_s)$. Since the enclosed mass can be written

$$M_{enc}(R) = 4\pi\rho_s R_s^3 \frac{f(R/R_s)}{f(C)} \text{ for } f(x) \equiv \ln(1+x) - \frac{x}{x+1} \tag{3.12}$$

and, by definition, $M_{vir} = M_{enc}(R_{vir})$ we find that

$$\rho_s = \frac{\rho_{vir} C^3}{3f(C)} \sim \rho_{vir} \frac{C^3}{\ln(C)} \text{ for } C \gg 1. \tag{3.13}$$

This means that $\Sigma(R) \simeq C^2 \tilde{\Sigma}(R/R_s)/\ln(C)$ which, since $\tilde{\Sigma}(R/R_s) \simeq 1/C^2$ for $C \gg 1$ (and $R < R_{vir}$), gives $\Sigma(R) \simeq 1/\ln(C)$. Hence the projected mass density will vanish logarithmically with C, making it increasingly similar to a point-like lens. By the same reasoning the enclosed projected mass must, for large concentrations, tend towards M_{vir} according to $M_p(R) \simeq M_{vir} \ln(RC/R_{vir})/\ln(C)$.

We do, in other words, expect the NFW profiled lenses to behave as black holes with mass M_{vir} for sufficiently high concentrations. Note, however, that the convergence towards point-like behavior is very slow when increasing C.

Let us now consider the cut-off that appears for sufficiently low concentrations. Numerically, this cut-off arises when no solution for $\mu(R) = \mu_T$ is found. That is, when the maximal magnification is below the threshold magnification. When this happens, the numerical solver returns, as it should, $\ell_T = 0$ which automatically yields zero expected microlensing events. According to equation (2.16), the magnification is formally divergent at fixed points $R_E^* = R_E(R_E^*)$ of the Einstein radius R_E. Therefore, the absence of a solution to the equation $\mu(R) = \mu_T$ suggest the disappearance of all non-trivial fixed points R_E^*. That is, since $\mu(R) \to 1$ for $R \to \infty$ then if $\mu(R)$ diverges at R_E^* continuity of μ leads to the existence of a solution to $\mu(R) = \mu_T$ for some $R \geqslant R_E^*$. Note, however, that one would expect sufficiently large magnifications to occur even in the absence of an Einstein ring provided that there exist points for which $R_E(R)/R$ is sufficiently close to unity*. To determine how the low concentration cut-off arises, we should therefore first discuss the existence of an Einstein ring for NFW profiled lenses.

3.2.3 Disappearance of the Einstein Ring

To determine the radius of the Einstein ring for an NFW profiled lens with parameters C and M_{vir}, we need to locate the fixed point $R_E^* = R_E(R_E^*)$, where R_E depends on C, M_{vir} as well as the positions of the source and the lens. First, note that the

* Since there are other divergent points of $\mu(R)$, $R_E(R)/R$ being close to unity is a sufficient, but not necessary, condition

enclosed projected mass scales as

$$M_p(R) \simeq \begin{cases} 2\pi\rho_s R_s R^2 \ln\frac{2R_s}{R} & \text{for } R \ll R_s \\ 4\pi\rho_s R_s^3 \ln\frac{R}{R_s} & \text{for } R \gg R_s \text{ and } R < R_{vir} \\ M_{vir} & \text{for } R \geqslant R_{vir} \end{cases} \tag{3.14}$$

Since $R_E(R) \propto \sqrt{M_p(R)}$ it follows that $R_E(R)$ scales roughly according to

$$R_E(R) \sim \begin{cases} R\sqrt{\rho_s R_s \ln\frac{R_s}{R}} & \text{for } R \ll R_s \\ \sqrt{\rho_s R_s^3 \ln\frac{R}{R_s}} & \text{for } R \gg R_s \text{ and } R < R_{vir} \\ \text{const} & \text{for } R \geqslant R_{vir} \end{cases} \tag{3.15}$$

This means that if the Einstein ring R_E^* is inside the scale radius R_s, then it will be roughly be given by

$$R_E^* \simeq R_s \exp\left(\frac{-\text{const}}{\sqrt{\rho_s R_s}}\right) \tag{3.16}$$

and since $\rho_s R_s \simeq C^2/\ln(C)$, the fixed point R_E^* must be exponentially decreasing by $R_E^* \simeq R_s \exp(-\sqrt{\ln(C)}/C)$ for $C \gg 1$. The geometry of this effect is depicted in figure 3.5.

Since R_E^* does not become much smaller than $R_E(M_{vir})$ when $R_E^* > R_s$, we can approximate the scale where the rapid shrinking of R_E^* starts by $R_E(M_{vir}) \simeq R_s$. This corresponds to the scenario where the red and yellow line in figure 3.5 would be on top of each other. This scale is shown in the prospect plane (figure 3.4) as a blue dashed line. Note that since $R_s \propto M_{vir}^{1/3}/C$ and $R_E(M_{vir}) \propto \sqrt{M_{vir}}$, the slope of this line must be given by $C_{cut-off} \propto M_{vir}^{-\frac{1}{6}}$. In fact, we can do even better than this. For $C \gg 1$ solving for $R_E(R_s) = R_s$ gives

$$C_{cut-off}(M_{vir}) = \left[\frac{4G}{c^2}\left(\frac{4\pi\rho_{vir}}{3}\right)^{\frac{2}{3}} D_s x(1-x)\ln\frac{e}{2}\right]^{-\frac{1}{2}} M_{vir}^{-\frac{1}{6}}. \tag{3.17}$$

This estimate appears as a dotted black line in the prospect plane 3.4. Note that this scale agrees perfectly with where the lines of equal number of expected microlensing events N_{exp} bends strongly towards lower masses.

To visualize more clearly what is going on, the magnification $\mu(R)$ of individual images for a halo of solar mass and $x = 0.1$ is portrayed as a function of the image position R and the concentration C in figure 3.6. Here, the dark purple contour corresponds to solutions of $\mu(R) = 1.17$ and the weak gray contour lines to log-spaced curves of equal source position. The points of equal concentration C along a line of equal source position correspond to (the absolute value of) the image positions of that configuration. Note that, in accordance with Burke's odd-number theorem [61], there are always either one or three images. Moreover, the innermost image will typically have a negligible magnification compared to the others.

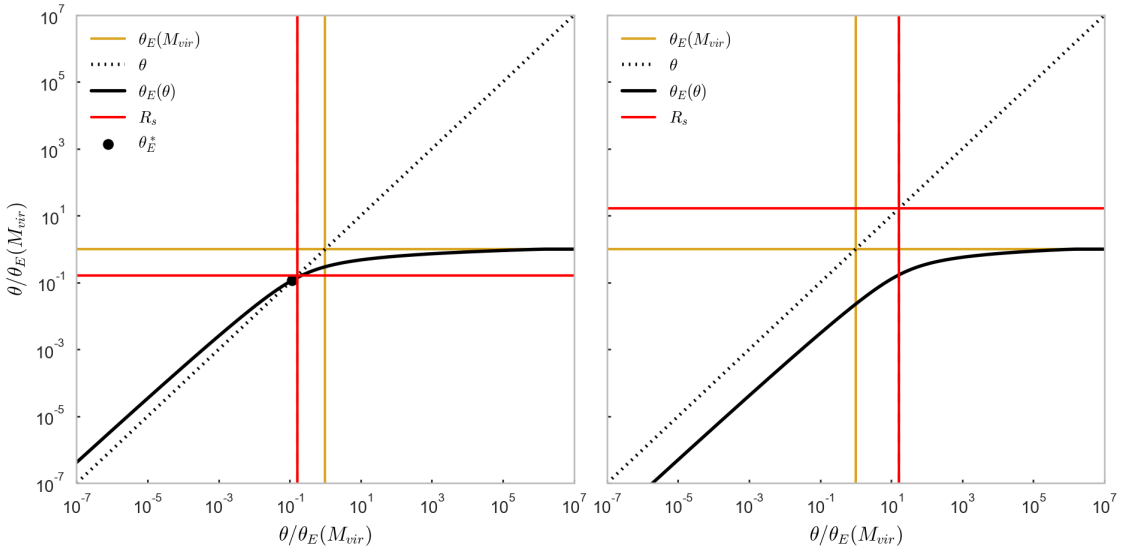

Figure 3.5: The Einstein radius function $\theta_E(\theta)$ (black filled) plotted together with the identity function (black dashed) for NFW profiled lenses with concentrations 10^7 (left) and 10^5 (right) and the same mass $M = 10^{-3}M_\odot$ and relative lens position $x = 0.01$ with respect to $D_s = 770\text{kpc}$. If an intersection point θ_E^* (black dot) exists it indicates the angular radius of an Einstein ring. The yellow line is the asymptotic value of $\theta_E(\theta)$ and the red line is the scale radius.

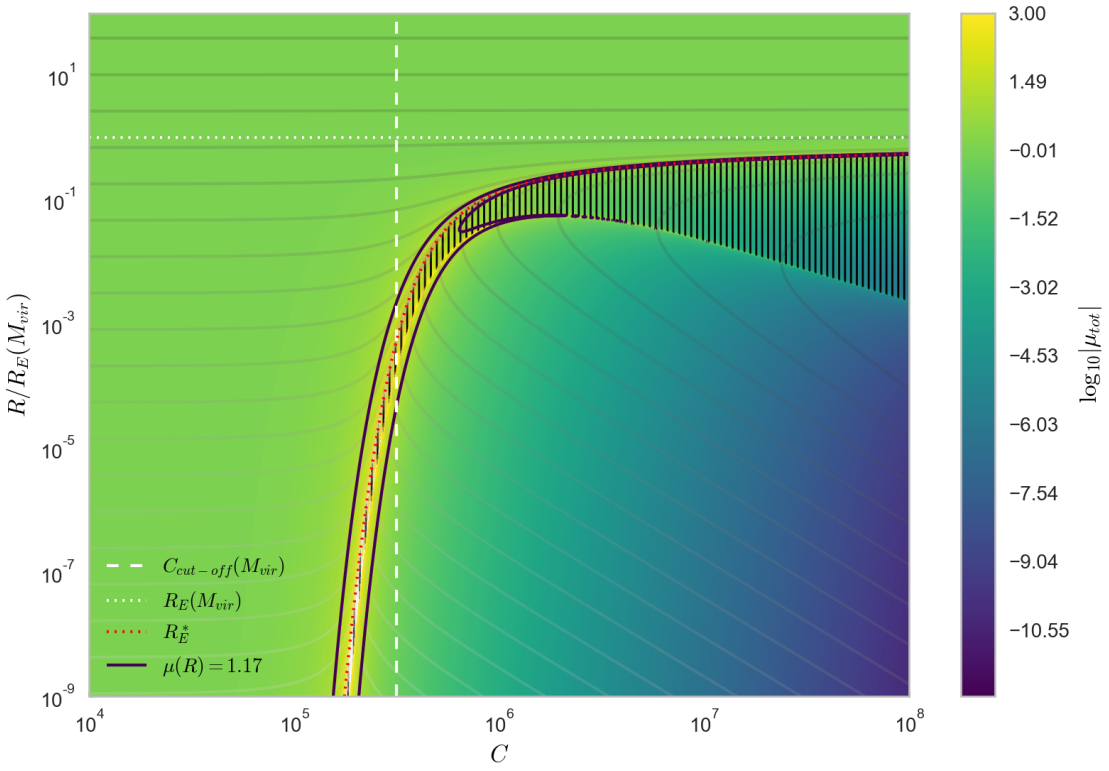

Figure 3.6: The magnification $|\mu(R)|$ for an NFW lens with $M_{vir} = M_\odot$ plotted as a function of the image position R and the concentration C. The region with vertical hatches shows where the image appears inverted ($\mu(R) < 0$), the solid dark purple contour line displays the solutions to $\mu(R) = 1.17$, and the white dashed line indicates the estimated cut-off concentration $C_{cut-off}$. The white dotted line shows the asymptotic value $R_E(M_{vir})$ for the Einstein radius. The weak, gray contour lines show curves of equal source position β.

The vertically hatched area corresponds to negative magnifications, meaning that the image will appear inverted. Therefore, the boundary of this area must correspond to scenarios of divergent total magnification. Here, the outer divergence is exactly the Einstein radius fixed point R_E^* (red dotted line). The disappearance of an Einstein ring can thus be seen as the exponential drop of R_E^* (red dotted line) for concentrations smaller than the cut-off $C_{cut-off}$ (white dashed line). Note how the position at magnification threshold $\mu(R) = 1.17$ drops together with R_E^*. As the $\mu(R) = 1.17$ line exponentially decreases with decreasing concentrations, then so does the source position corresponding to that image. That is, with the vanishing of the Einstein ring, the tube radius $\ell_T = D_s\beta(\mu = \mu_T)$ also vanishes. This is a nice time to recall the box-like x-dependence of $\mathcal{R}$ in figure 3.3. Since the Einstein radius scales as $R_E(R) \sim \sqrt{x(1-x)M_p(R)}$, it will attain smaller values closer to the boundaries of x. This effect, however, will be mathematically indistinguishable from lowering the virial mass M_{vir}. Since the cut-off of halos with lower mass occurs at higher concentrations, the tube radius will first vanish at the boundaries of x, i.e. close to either the source or the observer. Therefore, as one considers less concentrated halos, the cut-off will appear at increasingly large values of $x(1-x)$.

When the tube radius ℓ_T vanishes, then so does the chance for observing a microlensing event. What happens is that as $C \lesssim C_{cut-off}$ we are effectively probing a $\rho(R) \propto 1/R$ profile. In this case the projected mass scales roughly as the square of the image position $M_p(R) \sim R^2$, which results in a deflection angle that scales with the angular image position $\alpha \propto \theta$. In other words, the lens mapping becomes simply $\beta \propto \theta$ which results in a constant magnification $\mu(R)$ for images sufficiently far inside the halo. Therefore, the maximal magnification is set by the geometry and the lens profile and, crucially, scenarios closer to perfect alignment ($\beta \to 0$) do not make the lensing effects stronger!

Actually, since we are studying the *projected* mass M_p, the above argument is not perfectly valid as one would have an additional factor of $\ln(R_s/R)$ in the scaling of M_p, i.e $M_p(R) \sim R^2 \ln(R_s/R)$. This means that approaching perfect alignment will enhance the lensing effects, but only logarithmically at that.

We have now found that the hope for observing the microlensing of stars in M31 by WIMPy halos is feeble. The reason is that WIMPy halos have a relatively low concentration ($C \lesssim 10^2$) which leads to Einstein radii much less than the scale radius. Due to the weak lensing effects of a $1/r$ profile, the magnification never reaches the magnification threshold making events, if they do occur, pass unnoticed.

Chapter 4

Remedies and the Future

Up to this point, we have discussed the fundamental limits to the microlensing of WIMPy halos. In this chapter, we discuss the general prospects for constraining the abundance of WIMPy halos with microlensing when adopting more technically realistic assumptions. We will attempt to determine what is needed for the microlensing of WIMPs to produce observable effects, and recite some alternative techniques for probing the dark matter sub-structure.

4.1 Unspoken Complications

Before discussing whether WIMPy halos can ever be constrained using the technique developed in the previous chapters, we should spend some words on the complications that arise when adopting more realistic assumptions.

Let us start by recalling that not all halo parameters appearing in the prospect plane 3.4 are realistic. As previously pointed out, the most massive halos correspond to the unreasonable limiting case where halos of the same mass as the host galaxy pass the line of sight with a velocity normalized to $v_c \simeq 200\mathrm{km/s}$. In fact, these halos are also so large that many lens positions would violate the thin lens assumption.

Moreover, the halos with both very high concentration and very high mass are automatically ruled out by general relativity as the Schwarzschild radius $2GM_{enc}/c^2$ for the enclosed mass M_{enc} within the scale radius R_s become smaller than the scale radius. After all, that would mean the object is not well described as having an NFW density profile. Additionally, this might end up violating our initial assumption that spacetime can be treated as a perturbed Minkowskian spacetime, see equation (2.1). For NFW-profiled halos $2GM_{enc}/c^2 \simeq R_s$ occurs at $C_{sw} \simeq 2 \times 10^8$ for $M_{vir} = 10^{12}M_\odot$ and scales roughly as $C_{sw} \sim M_{vir}^{-2/3}$. It therefore only concerns masses in the range $10^9M_\odot - 10^{12}M_\odot$ with concentrations larger than 2×10^8.

Up to this point, we have silently ignored the possibility for the finite size of sources to affect microlensing by halo objects. In fact, it has been argued that for stars in the Large Magellanic Clouds, the effect of finite source size on microlensing

by point-like objects may be significant and non-trivial (see e.g. [98]). Roughly speaking, the effect of finite source size can be understood as follows. The finite size of a star will subtend some, often vanishingly small, angle θ_* on the sky. If this angle is comparable to the radius of the Einstein ring θ_E^*, then the star, even at perfect alignment, will just appear slightly deformed and magnified. For $\theta_* \gtrsim \theta_E^*$ all the strong lensing effects will simply deform the position of the star isophotes and therefore lead to negligible magnification effects. Therefore, one must have $\theta_E^* \gtrsim \theta_*$ to avoid finite source effects from suppressing the magnification. Now, a star with radius R_* at a distance D_s will subtend an angle

$$\theta_* \simeq \frac{R_*}{D_s} \simeq 6''.0 \times 10^{-9} \left(\frac{R_*}{R_\odot}\right) \left(\frac{770\text{kpc}}{D_s}\right) . \tag{4.1}$$

Comparing this to the Einstein radius

$$\theta_E^* \simeq 1''.0 \times 10^{-8} \left(\frac{1-x}{x}\right)^{1/2} \left(\frac{M_p(R_E^*)}{10^{-8}M_\odot}\right)^{1/2} \left(\frac{D_s}{770\text{kpc}}\right)^{-1/2} \tag{4.2}$$

suggests that even for point-like lenses with mass of the order $M_p \sim 10^{-8}M_\odot$ finite source size becomes important. In fact, the importance of finite source size increases when considering lenses closer to M31. This means that point-like lenses with $M \lesssim 10^{-8}M_\odot$ that are bound to M31 are likely not to be seen. Since MW and M31 hosts roughly the same amount of candidate microlenses, the expected number of events in figure 3.4 should be reduced by a factor of roughly 2 for the halos of lowest mass. Actually, since HSC monitored only the very brightest stars in M31 [90], many of the stars considered are expected to have much larger radius and thus further increasing the scale at which finite source size becomes important. Note also that for less concentrated halos, the projected enclosed mass $M_p(R_E^*)$ decreases. This means that finite source size will become increasingly important when lowering the concentration.

We saw in the last chapter that halos with a concentration below the concentration cut-off $C_{\text{cut-off}}$ will have an exponentially decreasing Einstein radius θ_E^*. A consequence of this is that for concentrations $C \lesssim C_{\text{cut-off}}$, the suppression of the magnification due to finite source size will rapidly increase with decreasing C. In other words, if there would have been a finite number of expected microlensing events for WIMPy halos in figure 3.4, they would most likely have to be disregarded when taking into account the finite source effects. Note, however, that it makes little sense to imagine a scenario in which there is both a finite number of WIMPy microlensing events and an exponentially decreasing Einstein radius below $C_{\text{cut-off}}$. The only possible way for this to happen is to consider a telescope with unrealistically low magnification threshold. As we shall see shortly, this is not a viable option.

When computing the number of expected microlensing events in the previous chapter, we set $\varepsilon(\hat{t}) = 1$ for all $\hat{t}$, without discussing the physical implication of such a choice. Realistic telescopes will have a non-zero exposure time δt. Roughly speaking,

this means that microlensing events with duration smaller than the exposure time $t_e \lesssim \delta t$ can occur without being detected by the telescope. Similarly, any survey monitors for a finite amount of time Δt, which lead events with durations $t_e \gtrsim \Delta t$ to not be fully captured and thus effectively pass unnoticed. These limits are, of course, only estimates of the order of magnitude. As photons will be detected during the exposure time, an excess can be detected even for t_e lower than the exposure time. The dead time between exposures will, however, set an absolute minimal observable event duration t_e. Likewise, event durations longer than the monitoring time can, at least in principle, be detected as slow inclinations in the magnitude of a star.

Actually, the middle part of figure 2.5, where $N_{exp} \sim M^{-1/2}$, correspond to those event durations that fall safely between the exposure time (2 minutes) and the total monitoring time (7 hours). This means that the effect of introducing an efficiency like that of HSC would heavily suppress the number of expected events in the prospect plane for all masses except those that are in vicinity of the region from $10^{-10}M_\odot$ to $10^{-5}M_\odot$. As concentrations decrease, however, this band is expected to drift towards higher masses as t_e decreases with $\ell_T \sim \theta_E^*$. If we manage to remedy the lensing of WIMPy halos, we may, in other words, end up needing a telescope with technically unrealistic exposure time.

4.2 Increased Distance and the Sparsity of Photons

In the previous chapter we saw that even for a telescope with ideal efficiency $\varepsilon = 1$, WIMPy halos would have a concentration multiple orders of magnitude too small for their microlensing of stars in M31 to be observable with a magnification threshold of $\mu_T = 1.34$. Therefore, a natural attempt at fixing the problem would be to construct a telescope with a much smaller magnification threshold. To see if this is possible, one would have to study the statistics and image analysis in detail. The magnification threshold will generally depend on the statistics of photons from the background compared to that of the source, as well as instrumental noise and the technique of background subtraction. Due to the disappearance of the Einstein ring, however, a reduced magnification threshold is likely to have little effect. In the best of cases, a reduced magnification threshold could open the possibility for detecting halos only slightly below the concentration cut-off (see e.g. figure 3.6). As discussed in the previous section this would quickly lead to serious difficulties due to both finite source size and the need for unrealistically short exposure time.

Recall that the exponential decrease of fixed points $R_E(R_E^*) = R_E^*$ was found to be related to the Einstein radius becoming smaller than the scale radius R_s. Moreover, the halo parameters that resulted in a vanishing number of expected events was estimated to be those with concentration lower than $C_{cut-off}(M_{vir})$ (3.17). Since $C_{cut-off}$ is proportional to $\sqrt{D_s}$ when keeping the relative lens position x fixed, a natural remedy is therefore to consider more distant sources.

Looking at the prospect plane depicted in figure 3.4, one would at least need the

cut-off to occur for concentrations two orders of magnitude lower in order to detect dwarf-galaxy-sized ($\sim 10^8 M_\odot$) halos. Since $C_{cut-off} \propto \sqrt{D_s}$, this means that one would have to consider sources four orders of magnitude further away, i.e 7.7Gpc. That is half the radius of the observable Universe! This is clearly not an option, but let us entertain the absurdity while introducing an important concept. Since the gravitational lensing formalism introduced in chapter 2 only considered a static, perturbed, Minkowskian spacetime, the interpretation of distances at cosmological scales is not clear. Actually, when we introduced the Einstein radius, we treated the distances D_l, D_s and D_{ls} as the *angular diameter* distances of a flat FRW spacetime. The problem is that in the ΛCDM cosmology, angular diameter distances cannot get larger than roughly 1.8Gpc*. When we substituted for $x \equiv D_l/D_s$ and wrote $D_{ls} = (1-x)D_s$, however, we treated the distances as if they were *comoving*. It turns out that if we treat distances as comoving, then $x(1-x)D_s$ should be replaced by $(1+z_l)x(1-x)D_s$, where z_l is the redshift of the lens (see [60] for a full discussion). In keeping the relative lens position fixed, this means that we should instead have used the scaling relation $C_{cut-off} \propto \sqrt{(1+z_l)D_s}$, which in the ΛCDM cosmology results in a minimal comoving distance of about $D_s \simeq 3$Gpc or, equivalently, a redshift of about $z_s \simeq 0.8$. A serious problem with considering microlensing of sources at $z_s \simeq 0.8$ is, of course, that there are few of them (see e.g. [99]) and, more importantly, that they are far to faint. Let us try to be quantitative about the faintness. In a static and flat spacetime, an observer at a distance D_s from a black-body with temperature T and radius R_* will receive a total number of

$$N_\gamma = \frac{R_*^2}{D_s^2}\frac{2\pi}{c^2}\left(\frac{kT}{\hbar}\right)^3 \int \frac{x^2 dx}{e^x - 1} \simeq 0.25/s/m^2 \left(\frac{T}{T_\odot}\right)^3 \left(\frac{R_*}{R_\odot}\right)^2 \left(\frac{D_s}{770kpc}\right)^{-2} \tag{4.3}$$

photons. Here $x \equiv \hbar\nu/kT$, $T_\odot = 5800$K and $R_\odot = 696000$km. This means that a sun-like star would provide only ~ 1600 photons in total for the 8.2m wide aperture of the HSC telescope every second minute. To claim an excess of $\delta N = N(\mu_T - 1)$ photons, with more than 3σ certainty, from a Poisson distribution with an average of N photon counts requires that $(\mu_T - 1)N > 3\sqrt{N}$. That is, in the complete absence of background photons even a perfect telescope with no detector uncertainties that is able to detect every single photon no matter the frequency, one would need a baseline of at least

$$N = \left(\frac{3}{\mu_T - 1}\right)^2 \simeq 78 \tag{4.4}$$

photons from that star in order to claim an excess with 3σ certainty with a magnification threshold at $\mu_T = 1.34$. This means that if one were to consider sources only a factor 10 further away then, since the number count decreases as the square of the distance, the photon statistics would simply be too bad for the HSC telescope to be able to claim a μ_T magnification of a sun-like star. Since short exposure times are required for detection of low-mass halos, the only possibility that remains is to build

*This value, and others like it, is computed using the cosmological parameters given in chapter 1.2.1 and would generally change in other cosmologies.

a ridiculously much larger telescope (recall the required factor of $\sim 10^4$ increase in D_s).

In fact, the HSC was unable to see sun-like stars in M31 even with a magnification threshold of $\mu_T = 1.34$. The HSC survey could only monitor stars with absolute magnitudes roughly from -2.4mag down to 1.5mag [90]. Note that 1.5mag barely reaches the most luminous stars in the main sequence. The point is that even for an ideal telescope being able to detect light at all frequencies, increasing the source distance would completely ruin the photon statistics. For each decrease in the concentration cut-off $C_{cut-off}$ (3.17) by a factor 10 when considering more distant stars, the photon count would drop by a factor of 10^4. One could, of course, consider only the most luminous of stars, but recall that a large number of stars monitored is crucial for observing the unlikely microlensing events.

In any way, the possibility of microlensing by WIMPy halos when considering sources at cosmological distances works only when keeping the relative lens position $x \equiv D_l/D_s$ fixed. For this to work, one would have to give up hope for detecting halos hosted by MW and instead start searching for distant host galaxies that are well aligned with a large population of very distant sources.

If one wants to remedy the situation by considering more distant sources, stars seem to be out of the picture. Quasars (QSOs), on the other hand, being both very distant and very luminous, would be ideal sources in this case. See e.g. [100] for the QSO number distribution as a function of redshift estimated from the 10k catalog. In fact, there are claims that dark matter sub-structure has been gravitationally detected at cosmological scales, see e.g. [101]. Note, however, that in this analysis halos are given a different density profile than the NFW. Additionally, there have been claims that the flux ratio anomalies in multiply imaged QSOs can be explained by including the perturbing effects of dwarf-galaxy-sized Cold Dark Matter substructure [102–105]. The lens systems discussed here are B1422+231 and PG1115+080 for which the lens and source distances are $z_s \simeq 3.36$, $z_l \simeq 0.34$ and $z_s \simeq 1.7$, $z_l \simeq 0.3$ respectively. This is well above what is required for the concentration cut-off to be lower than the concentration of WIMP halos, and therefore in good agreement with our results. That is, microlensing by WIMPy halos at those scales should produce observable magnification effects.

As pointed out by [105], the flux anomalies of B1422+231 can, however, also be explained by effects such as stellar microlensing, absorption and scattering with the interstellar medium. To determine if such perturbing effects of strong-lensed systems can be used to produce satisfactory bounds on the abundance of WIMPy halos a detailed analysis is needed. One would, for instance, need to distinguish perturbations due to Dark Matter halos from those of stellar microlensing. Moreover, one would have to determine the number of perturbing halos needed to explain the observation. At cosmological scales, microlensing event durations may increase significantly, which further complicates the determination of the number of lenses.

We conclude that the detection of individual microlensing events due to small-scale WIMPy halos only is possible at cosmological scales. The reason for this is related to the disappearance of an Einstein ring, the limited photon statistics,

the effects of finite source size and the need for an exponential decrease in the magnification threshold. In other words, the prospects for constraining the number of WIMPy halos by detection of individual microlensing events are feeble. Note, however, that gravitational lensing remains an important toolbox in general, and that individual microlensing events by halos more concentrated than those predicted by the WIMP may certainly be detected.

4.3 The Future of Halo Constraints from Lensing

We have now seen that there is little chance for constraining the number of small-scale WIMPy halos by detection of individual microlensing events. This does, however, only hold for WIMPy halos assumed to have low concentrations with an inner density slope of $\rho \propto 1/r$ *. Recall that the motivation for this thesis was the strong constraints on the abundance of NFW-profiled Axion miniclusters from the HSC survey [1].

As the prospect plane 3.4 suggests, microlensing may pose strong constraints on models that predict halos with high concentration. For example, in addition to the Axion miniclusters, it is likely that one can obtain stringent bounds on the population of so-called *Ultracompact Minihalos* (UCMHs). These are objects formed from the collapse of overdensities too small to form PBHs, but still large enough ($\delta \gtrsim 10^{-3}$) for the collapse to occur very early ($z \gtrsim 1000$) [106]. As argued by Aslanyan et al. [107] constraining the abundance of UCMHs would both provide information about the nature of dark matter, and the preferred parameter region for models of inflation. Much of the machinery introduced in the previous chapters, however, is tailored for NFW-profiled objects, and not for the expected $\rho \propto r^{-9/4}$ profile of UCMHs (see e.g. [108]). While this prevents us from immediately estimating for the number of expected microlensing events from UCMHs in the HSC survey, we can say that UCMHs, unlike the WIMPy halos, will not suffer from the disappearance on an Einstein ring. It is, in other words, considered likely that one can put strong bounds on the population of UCMHs using existing microlensing data.

There are many techniques related to gravitational microlensing that may have even more promising prospects. For completeness, we will conclude this text by reciting some of the alternative approaches for constraining dark matter substructure that has been proposed during the last years.

First of all, using the perturbative effects dark matter substructure has on the flux ratios in strongly lensed systems as discussed by [102–105], can maybe be used to constrain the abundance of WIMPy halos. At present, however, these studies offer little more than a hint of the existence of dark matter substructure and it remains to be determined whether utilizing this effect can ever pose actual limits on the halo mass function.

*From the analysis in the previous chapter, we actually expect this to hold for halos with $\rho \propto 1/r^n$ where $n \geqslant 1$.

A somewhat related class of methods for constraining halos are those based on Pulsar Timing Arrays (PTAs). One possibility is to consider the expected Shapiro time delay associated with halos passing the line of sight (see e.g. [109]). This has already been used to constrain the abundance of Ultracompact Minihalos (UCMHs) [110]. With increased time sensitivity, this technique may possibly also be used to constrain the abundance of WIMPy halos. It has also been claimed that the expected impulsive acceleration from the passage of CDM halos close to the pulsars or the solar system may be used to constrain the halo abundance, see e.g. [111].

Chapter 5

Conclusion

The deflection of light in gravitational potentials make distant stars appear deformed in the presence of intermediate massive objects. Such deformations tend to magnify the apparent size of the star, and thus also its apparent brightness. The passage of a massive object in front of the star will, in sufficiently well aligned cases, temporarily increase the apparent brightness of the star. A large population of stars in both the Magellanic Clouds (MACHO) and the Andromeda Galaxy (HSC) has been monitored, and the observed scarcity of such microlensing events has been used to place strong constraints on the abundance of Massive Astrophysical Compact Halo Objects (MACHOs) and Primordial Black Holes (PBHs). Recently, it has been claimed that highly concentrated halos predicted by the Axion dark matter scenario can be constrained by existing microlensing data.

In this thesis, we have discussed prospects for constraining general NFW-profiled halos in a model independent way, while at the same time focusing on the possibility for microlensing WIMPy halos. Such constraints can, generally, shed light on the cut-off in the halo mass function, and thus provide unique insight into the particle nature of dark matter.

We have discovered that while it is possible to pose strong constraints on highly concentrated NFW-profiled halos, the low concentration of WIMPy halos make them evade the existing constraints. This results from the exponential decline of the radius of the Einstein ring as it becomes smaller than the scale radius of the NFW profile. The halo parameters subject to this suppression are shown to be those with $R_E(M_{vir}) \lesssim R_s$. That is, the cut-off is closely related to the lensing scenario only being sensitive to a $\rho \propto 1/r$ profile. To observe the microlensing of halos with concentration only slightly less than the concentration cut-off, a greatly decreased magnification threshold is needed.

We argue that one is likely never to obtain constraints on the abundance of intra-galactic WIMPy halos from microlensing. While it is certainly possible for lenses and sources at cosmological distances to produce observable microlensing effects, it is unclear whether one can find a sufficiently large amount of sources well aligned with a population of sub-halos. In addition, the expected event durations may end up not being accessible.

In conclusion, the future may have a lot to offer, but probably not the detection of a microlensing event due to a nearby WIMPy halo.

Appendix A

The Deflection Angle

One of the great triumphs of General relativity is the ability to derive the trajectory of light in the vicinity of massive objects. When small deviations from a linear path is expected, it suffices to consider a perturbation of the Minkowskian spacetime. Assuming static sources and matter to behave as a perfect fluid, the perturbed Minkowski spacetime (expressed in transverse gauge) takes the form

$$g_{\mu\nu}dx^{\mu}dx^{\nu} = -(1+2\Phi)dt^2 + (1-2\Phi)d\mathbf{x}^2 \tag{A.1}$$

where Φ is the Newtonian gravitational potential. This means that the coordinate speed of a null ray ($g_{\mu\nu}dx^{\mu}dx^{\nu} = 0$) is given by

$$\frac{d|\mathbf{x}|}{dt} = \sqrt{\frac{1+2\Phi}{1-2\Phi}}. \tag{A.2}$$

The index of refraction created by the presence of a Newtonian potential is therefore given by

$$n = \sqrt{\frac{1-2\Phi}{1+2\Phi}} \simeq 1 - 2\Phi + \mathcal{O}(\Phi^2). \tag{A.3}$$

By invoking Fermat's principle it follows that possible trajectories of the light is constrained by

$$\frac{\delta}{\delta\mathbf{x}}\int_A^B n[\mathbf{x}]d\mathbf{x} \stackrel{!}{=} 0. \tag{A.4}$$

When changing variables to an affine parameter λ, the corresponding Euler-Lagrange equations take the form

$$\frac{d}{d\lambda}\frac{\partial}{\partial d_i}n|\mathbf{d}| = \frac{\partial}{\partial x_i}n|\mathbf{d}| \text{ where } \mathbf{d} \equiv \frac{d\mathbf{x}}{d\lambda}. \tag{A.5}$$

Choosing λ to normalize $\mathbf{d}$ ($|\mathbf{d}| = 1$), the tangential change in the direction of the ray can be conveniently written as

$$\frac{d}{d\lambda}\mathbf{d} = \frac{1}{n}\left[\nabla n - \mathbf{d}(\mathbf{d}\cdot\nabla n)\right] \equiv \nabla_{\perp}\ln n. \tag{A.6}$$

Since $\Phi \ll 1$ it follows that $\ln n = \ln(1-2\Phi) \simeq -2\Phi$ to first order. In this case, the net deflection angle takes the form

$$\boldsymbol{\alpha} = -\int d\lambda \nabla_\perp \ln n \simeq 2\int_{\lambda_A}^{\lambda_B} d\lambda \nabla_\perp \Phi. \tag{A.7}$$

To first order, lets start by considering the Newtonian potential for a point-like lens $\Phi(r) = -GM/r$ of an undeflected path purely along the z-axis so that $r = \sqrt{b^2+z^2}$ where $b = \sqrt{x^2+y^2}$ is the impact parameter of the ray. This means that

$$\nabla_\perp \Phi = \frac{GM}{r^3}\mathbf{r}_\perp \tag{A.8}$$

which yields the deflection angle

$$\boldsymbol{\alpha} = 2GM\mathbf{r}_\perp \int_\infty^\infty \frac{dz}{(z^2+b^2)^{3/2}} = \frac{4GM}{b}\frac{\mathbf{r}_\perp}{b}. \tag{A.9}$$

By definition, $|\mathbf{r}_\perp| = b$ so $|\boldsymbol{\alpha}| = 4GM/b$ with direction pointing towards the lens. A nice feature of this result is that it is linear in the mass. Assuming the deflection to happen instantaneously at the closest point to the lens, The deflection angle for an extended lens with projected density profile

$$\Sigma(\boldsymbol{\xi}) \equiv \int \rho\,(\boldsymbol{\xi}, z)\, dz \tag{A.10}$$

is therefore given by

$$\boldsymbol{\alpha}(\boldsymbol{\xi}) = 4G\int d^2x \Sigma(\mathbf{x}) \frac{\boldsymbol{\xi}-\mathbf{x}}{|\boldsymbol{\xi}-\mathbf{x}|^2}. \tag{A.11}$$

For an axially symmetric lens ($\Sigma(\mathbf{x}) = \Sigma(x)$), we may choose polar coordinates $\boldsymbol{\xi}-\mathbf{x} = (\xi - x\cos\theta, -x\sin\theta)$ so that

$$\alpha_1 = 4G\int_0^{2\pi} d\theta \int_0^\infty dx \Sigma(x) \frac{\xi x - x^2\cos\theta}{\xi^2+x^2-2\xi x\cos\theta}, \tag{A.12}$$

$$\alpha_2 = -4G\int_0^{2\pi} d\theta \int_0^\infty dx \Sigma(x) \frac{x^2\sin\theta}{\xi^2+x^2-2\xi x\cos\theta}. \tag{A.13}$$

While $\alpha_2 = 0$ due to antisymmetry of the integrand, we find

$$\int_0^{2\pi} d\theta \frac{\xi x - x^2\cos\theta}{\xi^2+x^2-2\xi x\cos\theta} = \begin{cases} 2\pi x/\xi & \text{for } x \leqslant \xi \\ 0 & \text{for } x > \xi \end{cases} \tag{A.14}$$

resulting in the expression

$$|\boldsymbol{\alpha}(\xi)| = \frac{4GM_p(\xi)}{\xi} \text{ where } M_p(\xi) = 2\pi\int_0^\xi \Sigma(x) x dx \tag{A.15}$$

is the enclosed projected mass. That is, an axially symmetric lens deflects the ray as if it was point-like of mass $M_p(\xi)$.

Bibliography

[1] M. Fairbairn, D. J. E. Marsh, J. Quevillon, and S. Rozier, "Structure Formation and Microlensing with Axion Miniclusters," 2017. arXiv: 1707.03310 [astro-ph.CO].

[2] W. T. B. Kelvin, *Baltimore lectures on molecular dynamics and the wave theory of light*. CJ Clay and Sons, 1904.

[3] G. Bertone and D. Hooper, "A History of Dark Matter," *Submitted to: Rev. Mod. Phys.*, 2016. arXiv: 1605.04909 [astro-ph.CO].

[4] J. Einasto, "Dark Matter," *Braz. J. Phys.*, vol. 43, pp. 369–374, 2013. DOI: 10.1007/s13538-013-0147-9. arXiv: 1308.2534 [astro-ph.CO].

[5] J. H. Oort, "The force exerted by the stellar system in the direction perpendicular to the galactic plane and some related problems," *Bull. Astron. Inst. Netherlands*, vol. 6, p. 249, Aug. 1932.

[6] J. Bovy and S. Tremaine, "On the local dark matter density," *Astrophys. J.*, vol. 756, p. 89, 2012. DOI: 10.1088/0004-637X/756/1/89. arXiv: 1205.4033 [astro-ph.GA].

[7] E. Hubble and M. L. Humason, "The Velocity-Distance Relation among Extra-Galactic Nebulae," *ApJ*, vol. 74, p. 43, Jul. 1931. DOI: 10.1086/143323.

[8] F. Zwicky, "Die rotverschiebung von extragalaktischen nebeln," *Helvetica Physica Acta*, vol. 6, pp. 110–127, 1933.

[9] F. Zwicky, "Republication of: The redshift of extragalactic nebulae," *General Relativity and Gravitation*, vol. 41, pp. 207–224, Jan. 2009. DOI: 10.1007/s10714-008-0707-4.

[10] Planck Collaboration, P. A. R. Ade, N. Aghanim, M. Arnaud, M. Ashdown, J. Aumont, C. Baccigalupi, A. J. Banday, R. B. Barreiro, J. G. Bartlett, and et al., "Planck 2015 results. XIII. Cosmological parameters," *A&A*, vol. 594, A13, A13, Sep. 2016. DOI: 10.1051/0004-6361/201525830. arXiv: 1502.01589.

[11] F. D. Kahn and L. Woltjer, "Intergalactic Matter and the Galaxy.," *ApJ*, vol. 130, p. 705, Nov. 1959. DOI: 10.1086/146762.

[12] V. C. Rubin, "One hundred years of rotating galaxies 1," *Publications of the Astronomical Society of the Pacific*, vol. 112, no. 772, pp. 747–750, 2000.

[13] H. W. Babcock, "The rotation of the Andromeda Nebula," *Lick Observatory Bulletin*, vol. 19, pp. 41–51, 1939. DOI: 10.5479/ADS/bib/1939LicOB.19.41B.

[14] N. U. Mayall, "Comparison of Rotational Motions Observed in the Spirals M31 and M33 and in The Galaxy," *Publications of Michigan Observatory*, vol. 10, 1951.

[15] M. S. Roberts, "A High-Resolution 21-CM Hydrogen-Line Survey of the Andromeda Nebula," *ApJ*, vol. 144, p. 639, May 1966. DOI: 10.1086/148645.

[16] V. C. Rubin and W. K. Ford Jr., "Rotation of the Andromeda Nebula from a Spectroscopic Survey of Emission Regions," *ApJ*, vol. 159, p. 379, Feb. 1970. DOI: 10.1086/150317.

[17] M. Roberts and A. Rots, "Comparison of Rotation Curves of Different Galaxy Types," *A&A*, vol. 26, pp. 483–485, Aug. 1973.

[18] M. S. Roberts and A. H. Rots, "Comparison of Rotation Curves of Different Galaxy Types," *A&A*, vol. 26, pp. 483–485, Aug. 1973.

[19] M. S. Roberts and R. N. Whitehurst, "The rotation curve and geometry of M31 at large galactocentric distances.," *ApJ*, vol. 201, pp. 327–346, Oct. 1975. DOI: 10.1086/153889.

[20] V. C. Rubin, W. K. Ford Jr., and N. Thonnard, "Extended rotation curves of high-luminosity spiral galaxies. IV - Systematic dynamical properties, SA through SC," *ApJ*, vol. 225, pp. L107–L111, Nov. 1978. DOI: 10.1086/182804.

[21] V. Rubin, W. Ford Jr., and N. Thonnard, "Rotational properties of 21 SC galaxies with a large range of luminosities and radii, from NGC 4605 /R = 4kpc/ to UGC 2885 /R = 122 kpc/," *ApJ*, vol. 238, pp. 471–487, Jun. 1980. DOI: 10.1086/158003.

[22] H. Gursky, A. Solinger, E. M. Kellogg, S. Murray, H. Tananbaum, R. Giacconi, and A. Cavaliere, "X-Ray Emission from Rich Clusters of Galaxies," *ApJ*, vol. 173, p. L99, May 1972. DOI: 10.1086/180926.

[23] D. J. Fixsen, "The Temperature of the Cosmic Microwave Background," *ApJ*, vol. 707, pp. 916–920, Dec. 2009. DOI: 10.1088/0004-637X/707/2/916. arXiv: 0911.1955.

[24] Planck Collaboration, P. A. R. Ade, N. Aghanim, C. Armitage-Caplan, M. Arnaud, M. Ashdown, F. Atrio-Barandela, J. Aumont, C. Baccigalupi, A. J. Banday, and et al., "Planck 2013 results. XV. CMB power spectra and likelihood," *A&A*, vol. 571, A15, A15, Nov. 2014. DOI: 10.1051/0004-6361/201321573. arXiv: 1303.5075.

[25] A. G. Riess, L. M. Macri, S. L. Hoffmann, D. Scolnic, S. Casertano, A. V. Filippenko, B. E. Tucker, M. J. Reid, D. O. Jones, J. M. Silverman, R. Chornock, P. Challis, W. Yuan, P. J. Brown, and R. J. Foley, "A 2.4% Determination of the Local Value of the Hubble Constant," *ApJ*, vol. 826, 56, p. 56, Jul. 2016. DOI: 10.3847/0004-637X/826/1/56. arXiv: 1604.01424.

[26] E. Kolb and M. Turner, *The early universe*. Westview press, 1994, vol. 69.

[27] S. Weinberg, *Cosmology*. Oxford University Press, 2008.

[28] L. Bergström and A. Goobar, *Cosmology and particle astrophysics*. Springer Science & Business Media, 2006.

[29] A. Linde, "Inflationary cosmology," in *Inflationary Cosmology*, Springer, 2008, pp. 1–54.

[30] J. M. Bardeen, P. J. Steinhardt, and M. S. Turner, "Spontaneous Creation of Almost Scale - Free Density Perturbations in an Inflationary Universe," *Phys. Rev.*, vol. D28, p. 679, 1983. DOI: 10.1103/PhysRevD.28.679.

[31] E. R. Harrison, "Fluctuations at the threshold of classical cosmology," *Phys. Rev.*, vol. D1, pp. 2726–2730, 1970. DOI: 10.1103/PhysRevD.1.2726.

[32] Y. B. Zeldovich, "A hypothesis, unifying the structure and the entropy of the Universe," *MNRAS*, vol. 160, 1P, 1972. DOI: 10.1093/mnras/160.1.1P.

[33] P. J. E. Peebles and J. T. Yu, "Primeval Adiabatic Perturbation in an Expanding Universe," *ApJ*, vol. 162, p. 815, Dec. 1970. DOI: 10.1086/150713.

[34] A. M. Green and A. R. Liddle, "Critical collapse and the primordial black hole initial mass function," *Phys. Rev.*, vol. D60, p. 063 509, 1999. DOI: 10.1103/PhysRevD.60.063509. arXiv: astro-ph/9901268 [astro-ph].

[35] T. Harada, C.-M. Yoo, and K. Kohri, "Threshold of primordial black hole formation," *Phys. Rev.*, vol. D88, no. 8, p. 084 051, 2013, [Erratum: Phys. Rev.D89,no.2,029903(2014)]. DOI: 10.1103/PhysRevD.88.084051,10.1103/PhysRevD.89.029903. arXiv: 1309.4201 [astro-ph.CO].

[36] P. J. E. Peebles, "The Gravitational Instability of the Universe," *ApJ*, vol. 147, p. 859, Mar. 1967. DOI: 10.1086/149077.

[37] D. Suto, T. Kitayama, K. Osato, S. Sasaki, and Y. Suto, "Confrontation of Top-Hat Spherical Collapse against Dark Halos from Cosmological N-Body Simulations," *Publ. Astron. Soc. Jap.*, vol. 68, no. 1, p. 14, 2016. DOI: 10.1093/pasj/psv122. arXiv: 1511.06935 [astro-ph.CO].

[38] M. Viel, J. Lesgourgues, M. G. Haehnelt, S. Matarrese, and A. Riotto, "Constraining warm dark matter candidates including sterile neutrinos and light gravitinos with WMAP and the Lyman-alpha forest," *Phys. Rev.*, vol. D71, p. 063 534, 2005. DOI: 10.1103/PhysRevD.71.063534. arXiv: astro-ph/0501562 [astro-ph].

[39] T. Bringmann and S. Hofmann, "Thermal decoupling of WIMPs from first principles," *JCAP*, vol. 0704, p. 016, 2007, [Erratum: JCAP1603,no.03,E02(2016)]. DOI: 10.1088/1475-7516/2007/04/016,10.1088/1475-7516/2016/03/E02. arXiv: hep-ph/0612238 [hep-ph].

[40] T. Bringmann, "Particle Models and the Small-Scale Structure of Dark Matter," *New J. Phys.*, vol. 11, p. 105 027, 2009. DOI: 10.1088/1367-2630/11/10/105027. arXiv: 0903.0189 [astro-ph.CO].

[41] T. Bringmann, H. T. Ihle, J. Kersten, and P. Walia, "Suppressing structure formation at dwarf galaxy scales and below: Late kinetic decoupling as a compelling alternative to warm dark matter," *Phys. Rev. D*, vol. 94, no. 10, 103529, p. 103 529, Nov. 2016. DOI: 10.1103/PhysRevD.94.103529. arXiv: 1603.04884 [hep-ph].

[42] T. Binder, T. Bringmann, M. Gustafsson, and A. Hryczuk, "Early kinetic decoupling of dark matter: when the standard way of calculating the thermal relic density fails," *Phys. Rev.*, vol. D96, no. 11, p. 115 010, 2017. DOI: 10.1103/PhysRevD.96.115010. arXiv: 1706.07433 [astro-ph.CO].

[43] T. Bringmann, J. Edsjö, P. Gondolo, P. Ullio, and L. Bergström, "DarkSUSY 6 : An Advanced Tool to Compute Dark Matter Properties Numerically," 2018. arXiv: 1802.03399 [hep-ph].

[44] B. Penning, "The Pursuit of Dark Matter at Colliders - An Overview," *J. Phys.*, vol. G45, no. 6, p. 063 001, 2018. DOI: 10.1088/1361-6471/aabea7. arXiv: 1712.01391 [hep-ex].

[45] T. Marrodán Undagoitia and L. Rauch, "Dark matter direct-detection experiments," *J. Phys.*, vol. G43, no. 1, p. 013 001, 2016. DOI: 10.1088/0954-3899/43/1/013001. arXiv: 1509.08767 [physics.ins-det].

[46] J. M. Gaskins, "A review of indirect searches for particle dark matter," *Contemp. Phys.*, vol. 57, no. 4, pp. 496–525, 2016. DOI: 10.1080/00107514.2016.1175160. arXiv: 1604.00014 [astro-ph.HE].

[47] S. Clesse and J. García-Bellido, "Seven Hints for Primordial Black Hole Dark Matter," 2017. arXiv: 1711.10458 [astro-ph.CO].

[48] J. F. Navarro, C. S. Frenk, and S. D. M. White, "The Structure of Cold Dark Matter Halos," *ApJ*, vol. 462, p. 563, May 1996. DOI: 10.1086/177173. eprint: astro-ph/9508025.

[49] M. A. Sánchez-Conde and F. Prada, "The flattening of the concentration–mass relation towards low halo masses and its implications for the annihilation signal boost," *Mon. Not. Roy. Astron. Soc.*, vol. 442, no. 3, pp. 2271–2277, 2014. DOI: 10.1093/mnras/stu1014. arXiv: 1312.1729 [astro-ph.CO].

[50] W. J. G. de Blok and A. Bosma, "High-resolution rotation curves of low surface brightness galaxies," *A&A*, vol. 385, pp. 816–846, Apr. 2002. DOI: 10.1051/0004-6361:20020080. eprint: astro-ph/0201276.

[51] J. I. Read and G. Gilmore, "Mass loss from dwarf spheroidal galaxies: the origins of shallow dark matter cores and exponential surface brightness profiles," *MNRAS*, vol. 356, pp. 107–124, Jan. 2005. DOI: 10.1111/j.1365-2966.2004.08424.x. eprint: astro-ph/0409565.

[52] A. Pontzen and F. Governato, "How supernova feedback turns dark matter cusps into cores," *MNRAS*, vol. 421, pp. 3464–3471, Apr. 2012. DOI: 10.1111/j.1365-2966.2012.20571.x. arXiv: 1106.0499.

[53] M. Vogelsberger, J. Zavala, F.-Y. Cyr-Racine, C. Pfrommer, T. Bringmann, and K. Sigurdson, "ETHOS – an effective theory of structure formation: dark matter physics as a possible explanation of the small-scale CDM problems," *Mon. Not. Roy. Astron. Soc.*, vol. 460, no. 2, pp. 1399–1416, 2016. DOI: 10.1093/mnras/stw1076. arXiv: 1512.05349 [astro-ph.CO].

[54] K. A. Oman *et al.*, "The unexpected diversity of dwarf galaxy rotation curves," *Mon. Not. Roy. Astron. Soc.*, vol. 452, no. 4, pp. 3650–3665, 2015. DOI: 10.1093/mnras/stv1504. arXiv: 1504.01437 [astro-ph.GA].

[55] A. Genina, A. Benítez-Llambay, C. S. Frenk, S. Cole, A. Fattahi, J. F. Navarro, K. A. Oman, T. Sawala, and T. Theuns, "The core-cusp problem: a matter of perspective," *MNRAS*, vol. 474, pp. 1398–1411, Feb. 2018. DOI: 10.1093/mnras/stx2855. arXiv: 1707.06303.

[56] S. Y. Kim, A. H. G. Peter, and J. R. Hargis, "There is No Missing Satellites Problem," 2017. arXiv: 1711.06267 [astro-ph.CO].

[57] M. Boylan-Kolchin, J. S. Bullock, and M. Kaplinghat, "Too big to fail? The puzzling darkness of massive Milky Way subhaloes," *MNRAS*, vol. 415, pp. L40–L44, Jul. 2011. DOI: 10.1111/j.1745-3933.2011.01074.x. arXiv: 1103.0007 [astro-ph.CO].

[58] W. H. Press and P. Schechter, "Formation of Galaxies and Clusters of Galaxies by Self-Similar Gravitational Condensation," *ApJ*, vol. 187, pp. 425–438, Feb. 1974. DOI: 10.1086/152650.

[59] A. Schneider, R. E. Smith, and D. Reed, "Halo Mass Function and the Free Streaming Scale," *Mon. Not. Roy. Astron. Soc.*, vol. 433, p. 1573, 2013. DOI: 10.1093/mnras/stt829. arXiv: 1303.0839 [astro-ph.CO].

[60] P. Schneider, C. Kochanek, and J. Wambsganss, *Gravitational lensing: strong, weak and micro: Saas-Fee advanced course 33*. Springer Science & Business Media, 2006, vol. 33.

[61] W. L. Burke, "Multiple gravitational imaging by distributed masses," *The Astrophysical Journal*, vol. 244, p. L1, 1981.

[62] D. Clowe, M. Bradač, A. H. Gonzalez, M. Markevitch, S. W. Randall, C. Jones, and D. Zaritsky, "A direct empirical proof of the existence of dark matter," *The Astrophysical Journal Letters*, vol. 648, no. 2, p. L109, 2006. [Online]. Available: http://stacks.iop.org/1538-4357/648/i=2/a=L109.

[63] I. Newton, "Opticks: Or a treatise of the reflexions, refractions, inflexions and colours of light," 1704.

[64] J. Giné, "On the origin of the deflection of light," *Chaos Solitons and Fractals*, vol. 35, pp. 1–6, Jan. 2008. DOI: 10.1016/j.chaos.2007.06.097. eprint: physics/0512121.

[65] A. S. Eddington, "The total eclipse of 1919 May 29 and the influence of gravitation on light," *The Observatory*, vol. 42, pp. 119–122, Mar. 1919.

[66] M. C. Davidson, "Ix. a determination of the deflection of light by the sun's gravitational field, from observations made at the total eclipse of may 29, 1919," *Phil. Trans. R. Soc. Lond. A*, vol. 220, no. 571-581, pp. 291–333, 1920.

[67] O. Chwolson, "Über eine mögliche Form fiktiver Doppelsterne," *Astronomische Nachrichten*, vol. 221, p. 329, Jun. 1924.

[68] A. Einstein, "Lens-like action of a star by the deviation of light in the gravitational field," *Science*, vol. 84, no. 2188, pp. 506–507, 1936.

[69] F. Zwicky, "Nebulae as gravitational lenses," *Phys. Rev.*, vol. 51, pp. 290–290, 4 1937. DOI: 10.1103/PhysRev.51.290. [Online]. Available: https://link.aps.org/doi/10.1103/PhysRev.51.290.

[70] M. Schmidt, "3C 273 : A Star-Like Object with Large Red-Shift," *Nature*, vol. 197, p. 1040, Mar. 1963. DOI: 10.1038/1971040a0.

[71] D. Walsh, R. F. Carswell, and R. J. Weymann, "0957 + 561 A, B - Twin quasistellar objects or gravitational lens," *Nature*, vol. 279, pp. 381–384, May 1979. DOI: 10.1038/279381a0.

[72] R. Weymann, F. Chaffee Jr, N. Carleton, D Walsh, R. Carswell, and M Davis, "Multiple-mirror telescope observations of the twin qsos 0957+ 561 a, b," *The Astrophysical Journal*, vol. 233, pp. L43–L46, 1979.

[73] R. J. Weymann, D. Latham, J. Roger, P. Angel, R. F. Green, J. W. Liebert, D. A. Turnshek, D. E. Turnshek, and J. A. Tyson, "The triple QSO PG1115+08 - Another probable gravitational lens," *Nature*, vol. 285, pp. 641–643, Jun. 1980. DOI: 10.1038/285641a0.

[74] G. Soucail, Y. Mellier, B. Fort, G. Mathez, and M. Cailloux, "The giant arc in A 370 - Spectroscopic evidence for gravitational lensing from a source at Z = 0.724," *A&A*, vol. 191, pp. L19–L21, Feb. 1988.

[75] R. Lynds and V. Petrosian, "Luminous arcs in clusters of galaxies," *ApJ*, vol. 336, pp. 1–8, Jan. 1989. DOI: 10.1086/166989.

[76] J. Hewitt, E. Turner, D. Schneider, B. Burke, G. Langston, and C. Lawrence, "Unusual radio source mg1131+ 0456: A possible einstein ring," *Nature*, vol. 333, no. 6173, p. 537, 1988.

[77] K. Chang and S. Refsdal, "Flux variations of QSO 0957+561 A, B and image splitting by stars near the light path," *Nature*, vol. 282, pp. 561–564, 1979. DOI: 10.1038/282561a0.

[78] P. Young, "Q0957+561 - Effects of random stars on the gravitational lens," *ApJ*, vol. 244, pp. 756–767, Mar. 1981. DOI: 10.1086/158752.

[79] R. E. Schild and R. C. Smith, "Microlensing in the Q0957 + 561 gravitational mirage," *AJ*, vol. 101, pp. 813–817, Mar. 1991. DOI: 10.1086/115724.

[80] M. J. Irwin, R. L. Webster, P. C. Hewett, R. T. Corrigan, and R. I. Jedrzejewski, "Photometric variations in the Q2237 + 0305 system - First detection of a microlensing event," *AJ*, vol. 98, pp. 1989–1994, Dec. 1989. DOI: 10.1086/115272.

[81] J. Wambsganss, B. Paczynski, and N. Katz, "A microlensing model for QSO 2237 + 0305," *ApJ*, vol. 352, pp. 407–412, Apr. 1990. DOI: 10.1086/168546.

[82] B. Paczynski, "Gravitational microlensing by the galactic halo," *Astrophys. J.*, vol. 304, pp. 1–5, 1986. DOI: 10.1086/164140.

[83] E Aubourg, P Bareyre, S Brehin, M Gros, M Lachieze-Rey, B Laurent, E Lesquoy, C. Magneville, A Milsztajn, L Moscoso, *et al.*, "Evidence for gravitational microlensing by dark objects in the galactic halo," *Nature*, vol. 365, no. 6447, p. 623, 1993.

[84] C. Alcock *et al.*, "Probable Gravitational Microlensing towards the Galatic Bulge," *Astrophys. J.*, vol. 445, p. 133, 1995. DOI: 10.1086/175678. arXiv: astro-ph/9407009 [astro-ph].

[85] C. Alcock *et al.*, "The MACHO project: Microlensing results from 5.7 years of LMC observations," *Astrophys. J.*, vol. 542, pp. 281–307, 2000. DOI: 10.1086/309512. arXiv: astro-ph/0001272 [astro-ph].

[86] T. Lasserre, "Not enough stellar mass machos in the galactic halo," *Astron. Astrophys.*, vol. 355, pp. L39–L42, 2000. arXiv: astro-ph/0002253 [astro-ph].

[87] B. Paczynski, K. Z. Stanek, A. Udalski, M. Szymanski, J. Kaluzny, M. Kubiak, M. Mateo, W. Krzeminski, and G. W. Preston, "Results from the optical gravitational lensing experiment (ogle)," 1994. arXiv: astro-ph/9411004 [astro-ph].

[88] C. Afonso *et al.*, "Bulge microlensing optical depth from EROS 2 observations," *Astron. Astrophys.*, vol. 404, pp. 145–156, 2003. DOI: 10.1051/0004-6361:20030307. arXiv: astro-ph/0303100 [astro-ph].

[89] A. P. S. Crotts, "M31 - A unique laboratory for gravitational microlensing," *ApJ*, vol. 399, pp. L43–L46, Nov. 1992. DOI: 10.1086/186602.

[90] H. Niikura, M. Takada, N. Yasuda, R. H. Lupton, T. Sumi, S. More, A. More, M. Oguri, and M. Chiba, "Microlensing constraints on $10^{-10}M_{\odot}$-scale primordial black holes from high-cadence observation of M31 with Hyper Suprime-Cam," 2017. arXiv: 1701.02151 [astro-ph.CO].

[91] R. J. Nemiroff, "On the probability of detection of a single gravitational lens," *ApJ*, vol. 341, pp. 579–587, Jun. 1989. DOI: 10.1086/167518.

[92] K. Griest, "Detecting dark matter via microlensing," *AIP Conf. Proc.*, vol. 243, pp. 1080–1085, 1992. DOI: 10.1063/1.41530.

[93] J. Bovy, C. Allende Prieto, T. C. Beers, D. Bizyaev, L. N. da Costa, K. Cunha, G. L. Ebelke, D. J. Eisenstein, P. M. Frinchaboy, A. E. García Pérez, L. Girardi, F. R. Hearty, D. W. Hogg, J. Holtzman, M. A. G. Maia, S. R. Majewski, E. Malanushenko, V. Malanushenko, S. Mészáros, D. L. Nidever, R. W. O'Connell, C. O'Donnell, A. Oravetz, K. Pan, H. J. Rocha-Pinto, R. P. Schiavon, D. P. Schneider, M. Schultheis, M. Skrutskie, V. V. Smith, D. H. Weinberg, J. C. Wilson, and G. Zasowski, "The Milky Way's Circular-velocity Curve between 4 and 14 kpc from APOGEE data," *ApJ*, vol. 759, 131, p. 131, Nov. 2012. DOI: 10.1088/0004-637X/759/2/131. arXiv: 1209.0759 [astro-ph.GA].

[94] C. Carignan, L. Chemin, W. K. Huchtmeier, and F. J. Lockman, "Extended hi rotation curve and mass distribution of m31," *Astrophys. J.*, vol. 641, pp. L109–L112, 2006. DOI: 10.1086/503869. arXiv: astro-ph/0603143 [astro-ph].

[95] C. Alcock *et al.*, "The MACHO project first year LMC results: The Microlensing rate and the nature of the galactic dark halo," *Astrophys. J.*, vol. 461, p. 84, 1996. DOI: 10.1086/177039. arXiv: astro-ph/9506113 [astro-ph].

[96] A. Klypin, H. Zhao, and R. S. Somerville, "Lambda CDM-based models for the Milky Way and M31 I: Dynamical models," *Astrophys. J.*, vol. 573, pp. 597–613, 2002. DOI: 10.1086/340656. arXiv: astro-ph/0110390 [astro-ph].

[97] T. Brainerd and C. Wright, "Gravitational lensing by nfw halos," Tech. Rep., 1999. arXiv: astro-ph/9908213 [astro-ph].

[98] H. J. Witt and S. Mao, "Can lensed stars be regarded as pointlike for microlensing by MACHOs?" *ApJ*, vol. 430, pp. 505–510, Aug. 1994. DOI: 10.1086/174426.

[99] J. A. Peacock *et al.*, "A Measurement of the cosmological mass density from clustering in the 2dF Galaxy Redshift Survey," *Nature*, vol. 410, pp. 169–173, 2001. DOI: 10.1038/35065528. arXiv: astro-ph/0103143 [astro-ph].

[100] S. M. Croom, R. J. Smith, B. J. Boyle, T. Shanks, N. S. Loaring, L. Miller, and I. J. Lewis, "The 2df qso redshift survey - v. the 10k catalogue," *Mon. Not. Roy. Astron. Soc.*, vol. 322, p. L29, 2001. DOI: 10.1046/j.1365-8711.2001.04474.x. arXiv: astro-ph/0104095 [astro-ph].

[101] S Vegetti, D. Lagattuta, J. McKean, M. Auger, C. Fassnacht, and L. Koopmans, "Gravitational detection of a low-mass dark satellite galaxy at cosmological distance," *Nature*, vol. 481, no. 7381, p. 341, 2012.

[102] S. Mao and P. Schneider, "Evidence for substructure in lens galaxies?" *MNRAS*, vol. 295, p. 587, Apr. 1998. DOI: 10.1046/j.1365-8711.1998.01319.x. eprint: astro-ph/9707187.

[103] M. Chiba, "Probing dark matter substructure in lens galaxies," *Astrophys. J.*, vol. 565, p. 17, 2002. DOI: 10.1086/324493. arXiv: astro-ph/0109499 [astro-ph].

[104] N. Dalal and C. S. Kochanek, "Direct detection of CDM substructure," *Astrophys. J.*, vol. 572, pp. 25–33, 2002. DOI: 10.1086/340303. arXiv: astro-ph/0111456 [astro-ph].

[105] C. Kochanek and N Dalal, "Tests for substructure in gravitational lenses," *The Astrophysical Journal*, vol. 610, no. 1, p. 69, 2004.

[106] M. Ricotti and A. Gould, "A New Probe of Dark Matter and High-Energy Universe Using Microlensing," *Astrophys. J.*, vol. 707, pp. 979–987, 2009. DOI: 10.1088/0004-637X/707/2/979. arXiv: 0908.0735 [astro-ph.CO].

[107] G. Aslanyan, L. C. Price, J. Adams, T. Bringmann, H. A. Clark, R. Easther, G. F. Lewis, and P. Scott, "Ultracompact minihalos as probes of inflationary cosmology," *Phys. Rev. Lett.*, vol. 117, no. 14, p. 141 102, 2016. DOI: 10.1103/PhysRevLett.117.141102. arXiv: 1512.04597 [astro-ph.CO].

[108] E. Bertschinger, "Self-similar secondary infall and accretion in an Einstein-de Sitter universe," *ApJ*, vol. 58, pp. 39–65, 1985. DOI: 10.1086/191028.

[109] E. R. Siegel, M. P. Hertzberg, and J. N. Fry, "Probing Dark Matter Substructure with Pulsar Timing," *Mon. Not. Roy. Astron. Soc.*, vol. 382, p. 879, 2007. DOI: 10.1111/j.1365-2966.2007.12435.x. arXiv: astro-ph/0702546 [astro-ph].

[110] H. A. Clark, G. F. Lewis, and P. Scott, "Investigating dark matter substructure with pulsar timing – I. Constraints on ultracompact minihaloes," *Mon. Not. Roy. Astron. Soc.*, vol. 456, no. 2, pp. 1394–1401, 2016, [Erratum: Mon. Not. Roy. Astron. Soc.464,no.2,2468(2017)]. DOI: 10.1093/mnras/stw2582, 10.1093/mnras/stv2743. arXiv: 1509.02938 [astro-ph.CO].

[111] K. Kashiyama and M. Oguri, "Detectability of Small-Scale Dark Matter Clumps with Pulsar Timing Arrays," *ArXiv e-prints*, Jan. 2018. arXiv: 1801.07847.